THE UNIVERSITY OF CHICAGO

HYBRID CAVITY QED WITH RYDBERG ATOMS

A DISSERTATION SUBMITTED TO
THE FACULTY OF THE DIVISION OF THE PHYSICAL SCIENCES
IN CANDIDACY FOR THE DEGREE OF
DOCTOR OF PHILOSOPHY

DEPARTMENT OF PHYSICS

BY
MARK STONE

CHICAGO, ILLINOIS
DECEMBER 2021

Dedicated to my parents Keith and Lisa, and my brother Russell

TABLE OF CONTENTS

LIST OF FIGURES vii

LIST OF TABLES ix

ACKNOWLEDGMENTS x

ABSTRACT xii

1 INTRODUCTION 1
1.1 Optical mm-wave Transduction 2
1.2 Hybrid Cavity QED 3
1.3 Thesis Layout 5

2 CAVITY QED 7
2.1 Quantized Light-Matter Interaction 8
2.1.1 Rotating Wave Approximation 10
2.1.2 The Jaynes-Cummings Hamiltonian 11
2.1.3 Photon Blockade 12
2.2 Input, Output, and Dissipation 13
2.2.1 Input-Output Theory 13
2.3 Non-Hermitian Hamiltonians 17
2.3.1 Non-Hermitian Perturbation Theory 18
2.4 Multiple Atoms 21
2.4.1 Behavior of Collective States 23
2.5 Rydberg Electromagnetically-Induced Transparency 24
2.5.1 Rydberg Collective States 24
2.5.2 Rydberg Polaritons 26
2.6 Interfacing Atoms and mm-Waves: Strong Nonlinearity 28
2.7 Impedance Matching in Atomic Systems 30
2.7.1 Dipole Emitter Impedance Matching 31
2.7.2 Cooperativity and Impedance Matching 32
2.7.3 EIT Impedance Matching 34

3 A HYBRID QUANTUM APPARATUS 37
3.1 Pulse Tube Cryocooler 39
3.1.1 Thermal Management 40
3.2 Cryogenic Grating Magneto-Optical Trap 43
3.2.1 Optical Lattice Transport 46
3.3 mm-Wave Resonators 47
3.3.1 Hybrid Cavity 51
3.3.2 Tuning Mode 52
3.4 Magnetic Field Control 55

3.5 Laser System . . . 57
3.5.1 Frequency Following . . . 58
3.5.2 Cryogenic Optics . . . 60
3.6 Hybrid Cavity QED . . . 61
3.6.1 Electromagnetically-induced transparency . . . 61
3.6.2 Autler-Townes Splitting . . . 62
3.6.3 mm-wave Tuning and Hybrid Coupling Signature . . . 64

4 VIBRATIONS AND MECHANICAL DESIGN . . . 66
4.1 Overview of Cryogenic Vibration Suppression . . . 67
4.1.1 Mechanical Decoupling . . . 68
4.1.2 Low-Pass Mechanical Filtering . . . 69
4.1.3 Damping . . . 70
4.1.4 High-Pass Mechanical Filtering . . . 72
4.1.5 Requirements for Hybrid Atomic System . . . 73
4.2 Custom Low-Vibration Cryostat . . . 74
4.2.1 Accelerometer Measurement . . . 77
4.2.2 Interferometer Measurement . . . 78
4.3 First Generation Optical Cavities . . . 80
4.3.1 Optical Cavity Components . . . 81
4.3.2 Epoxy Cavity Construction . . . 82
4.3.3 Epoxy Cavity Performance . . . 84
4.4 Mechanical Network Analysis . . . 87
4.4.1 Mobility Analogy . . . 88
4.4.2 Piezoelectric Transducers . . . 90
4.4.3 Circuit Model of Mechanical Resonances . . . 91
4.5 Spring Preload Cavities . . . 94
4.5.1 Preloading Piezoelectric Actuators . . . 96
4.5.2 Spring Preload Design . . . 97
4.5.3 Material Considerations . . . 100
4.5.4 Performance of Spring Mirror Mounts . . . 101
4.5.5 Temperature Dependence . . . 105
4.6 Conclusion . . . 105

5 OPTICAL TO MM-WAVE TRANSDUCTION . . . 108
5.1 Basics of Atomic Transduction . . . 109
5.1.1 Transducer Hamiltonian . . . 111
5.1.2 Phase Matching . . . 112
5.2 Resonant Transduction . . . 113
5.2.1 Elimination of Dressed State . . . 116
5.2.2 Decay of the Dressed States . . . 119
5.3 Transducer Performance . . . 120
5.3.1 Optimal Transducer Parameters . . . 121
5.3.2 Off-Resonant Operation . . . 122

5.4 Transducer Collective States 124
5.5 Transducer with Non-Uniform Couplings 125
5.5.1 Elimination of Atomic Degrees of Freedom 128
5.6 Conclusion 129

6 TUNABLE FINESSE AND MODE CONVERSION 130
6.1 Tunable Finesse Cavity 132
6.2 Impedance Matching Physical Picture 135
6.3 Mode Converter 136
6.4 Outlook 140

REFERENCES 141

A SI: MODE CONVERSION 155
A.1 Single-Mode S-Matrix Approach for Coupled Fabry Pérot Cavities 155
A.2 Suppression of Loss Through Higher-Order Modes 157
A.3 Multimode Scattering Matrix Approach for Coupled Fabry-Pérot Cavities . . 158
A.4 Mode Purity 161
A.5 Overlap of Hermite-Gauss Modes 162
A.6 Two-Mode Coupled Mode Analysis 163
A.7 Multimode Coupled Mode Analysis 165

LIST OF FIGURES

1.1 Mean thermal photon occupation of microwaves and mm-waves 3

2.1 Transmission spectra of a driven cavity with atoms. 12

3.1 Science chamber interior 38
3.2 Interior of custom two-chamber cryostat 39
3.3 Details of pulse tube cryocooler 40
3.4 Stainless steel standoffs 42
3.5 Cryogenic atom source 44
3.6 Grating magneto-optical trap 45
3.7 Optical lattice transport 47
3.8 Optical lattice lifetime versus position 48
3.9 Seamless evanescent-coupled mm-wave resonators 48
3.10 Quality factor measurements of mm-wave resonators 49
3.11 Cavity mm-wave filters of various frequencies. 51
3.12 Hybrid optical mm-wave cavity. 51
3.13 Cavity Stark tuning of Rydberg atoms. 53
3.14 Modified precision rectifier for mm-wave power lock 54
3.15 Magnetic field control in a superconducting cavity. 56
3.16 Laser system for rubidium D_2 line. 57
3.17 Locking scheme for science cavity with frequency following. 59
3.18 Cryogenic optics mounts. 60
3.19 Vacuum Rabi splitting and EIT transmission spectra in hybrid cavity 62
3.20 EIT transmission spectrum with improved magnetic field control in superconductor 63
3.21 Autler-Townes splitting in Rydberg manifold from mm-wave drive 63
3.22 Tuning of Rydberg transition into resonance with mm-wave cavity 64

4.1 Custom two-chamber cryostat with vibration-decoupling design. 75
4.2 Flexible thermal connection 76
4.3 Accelerometer measurement of vibration isolation. 77
4.4 Interferometer measurement on science chamber 35K vibrations. 79
4.5 Construction of epoxied cavities. 83
4.6 Length shaking of epoxy cavity. 85
4.7 Block diagram for transfer function measurement. 86
4.8 Piezo transfer function for epoxy cavity. 87
4.9 Two springs in parallel. 88
4.10 Two-port network model of a 1D piezoelectric transducer. 91
4.11 Model of driven piezo interacting with mount and epoxy resonances 92
4.12 Comparison of mechanical transfer functions for different cryogenic epoxies. . . . 93
4.13 CAD model of spring preload mirror mounts on optical cavity. 94
4.14 Circuit model of spring preload mirror mount. 95
4.15 Components of spring mirror mounts laid out 98

4.16 Completed cavity with spring mirror mounts. 99
4.17 Length shaking of spring cavity. 102
4.18 Comparison of piezo transfer function and vibrational noise. 103
4.19 Mechanical transfer function for a shorter mirror in a spring-piezo mount 104
4.20 Temperature variation of vibrational properties of a spring cavity 106
4.21 Potential design for an extensional flexure spring mirror mount. 107

5.1 Relevant energy levels for optical-mmwave transduction. 109
5.2 Dressed state elimination in a three-level system 114
5.3 Transducer bandwidth versus mm-wave cavity linewidth 123
5.4 Off-resonant transducer efficiency. 123

6.1 Tunable finesse optical cavity 133
6.2 Principle of cavity optical mode conversion 137
6.3 Demonstration of high-efficiency mode conversion 138

A.1 Simulated spectrum of coupled multimode optical resonators 159

LIST OF TABLES

4.1 Properties of the two piezos used for optical cavities. 82
4.2 Analogous quantities in the mobility analogy. 89

ACKNOWLEDGMENTS

First, I want to thank my advisors, Jon Simon and Dave Schuster. Jon's boundless creativity and genuine excitement for science and teaching cannot help but inspire the same in his students. He has spent countless hours working with me, not just to help the experiment get built, but to elucidate the physics, develop my skills as a scientist, and ensure that I have gotten the most out of my PhD. Dave is deeply committed to his students' growth, and the combination of his scientific clarity of thought and technical expertise have made even the most daunting challenges surmountable. My PhD has been influenced at every step by their brilliance and enthusiasm.

The hybrid quantum experiment is very much a team effort, and has benefitted from a group of talented and dedicated scientists. Since Lavanya Taneja joined the group, she has transformed the experiment into a much more elegant machine, and I am glad it is now in such capable hands. Ash Kumar, our first postdoc, is a constant source of ideas, energy, and banter, and the progress of the last few years would not have been possible without him. Aziza Suleymanzade and I have worked together since the beginning. I have learned a great deal from her optimism and nonstop work ethic in the face of challenges, and I couldn't have asked for a better lab partner to build this experiment together.

I found many mentors and friends in the members of the Simon and Schuster labs. Alex Georgakopoulos and Clai Owens welcomed me from day one, taught me much, and helped build the incomparable social culture of the lab. Albert Ryou was always willing to spend time to pass down his knowledge from building up the polariton experiment. Nathan Schine, Matt Jaffe, Ningyuan Jia, and Logan Clark all brought immense knowledge and cheer to the lab, and provided me many insights in enthusiastic whiteboard talks over the years. Claire Baum, Chuan Yin, Henry Ando, and Lukas Palm are doing fantastic work and have taken up the mantle of making a collaborative and friendly lab. I have many people to thank in the Schuster group – Brendan Saxberg, Gabrielle Roberts, Alex Ma, Meg Panetta, and

especially Sasha Anferov and Andrew Oriani, whose incredible technical knowledge and love for talking shop were a great help.

The JFI staff not only provided the support to make this work possible, but made the community a welcoming one. Maria Jimenez has kept the lab running seamlessly through generations of unorganized grad students. I spent a great deal of time in the machine shop with Luigi Mazzenga, and never found a problem he didn't have an answer for, even if it involved tracking down obscure machine parts. Our building manager John Phillips worked tirelessly to fix problems as they arose, and is truly one of the friendliest people I've met. Bentley Wall has done a fantastic job since taking over.

I have had the privilege to work with some fantastic undergraduates in the Simon lab. Scott Eustice helped get the lab started as we all learned about cryogenics together. Jasmine Kalia did an awesome job making the getter shield and exploring mm-waves. Lin Su was an incredibly hard worker and tackled several large projects on the experiment.

Finally, I want to acknowledge the support of my friends and family, who have filled these past years with joy. Thank you Todd, Gautam, Linsin, Lipi, Ryan, and Karthik. My parents Keith and Lisa, and my brother Russell, have given me steadfast encouragement, support, and love. Thank you Mia, for inspiring and supporting me through this all.

ABSTRACT

Cold atoms in cavity quantum electrodynamics experiments, and their counterparts using superconducting or solid-state qubits, have enabled impressive and complementary results in quantum-enhanced technology. Combining the advantages of these platforms has clear benefits for quantum networking and metrology, but is complicated by their operation at different ranges of the electromagnetic spectrum. Atomic gases provide a possible solution due to their ground state optical transitions and dense energy level structure with GHz transitions between highly excited Rydberg states.

This thesis will describe how a gas of ultracold Rydberg atoms can be simultaneously coupled to single optical and millimeter wave photons using cavity electromagnetically-induced transparency. I will describe the development of a new hybrid quantum apparatus, including high finesse optical and mm-wave resonators at 5 Kelvin, a cryogenic laser-cooled atom source, and techniques for manipulating atoms in a superconducting cavity. This system has immediate applications for upconverting mm-wave photons to optical frequencies for long-distance quantum communication, with predicted efficiency of greater than 90% and bandwidth of $\sim$ 3 MHz. Furthermore, the very high cooperativity coupling achievable at mm-wave frequencies could enable cavity-mediated interactions between Rydberg atoms and creation of metrologically useful entangled atomic states. I will report recent results from the experiment, including evidence of coupling between Rydberg polaritons and a mm-wave resonator with photon occupation $n \approx 1$, with a clear path forward to enter the strong coupling regime.

CHAPTER 1

INTRODUCTION

Quantum mechanics provides an extraordinarily well-tested and precise description of the microscopic world. Although the fundamental equations are well-known, groups of more than a few interacting particles exhibit rich and useful phenomena enabled by entanglement, which may be difficult or impossible to calculate directly [1]. This richness has motivated the creation of quantum systems from the ground up, intentionally engineering a system whose behavior depends critically on quantum mechanics. Designer quantum systems have led to direct observation of entanglement [2], quantum phases of matter [3] and quantum phase transitions [4, 5].

Another effort focuses on creating precisely controlled entangled states of many particles for computation or simulation purposes [6], inspired by the discovery of algorithms which outpace all known classical methods for certain problems [7]. Recent progress has resulted in entangled states of more than a dozen qubits [8, 9, 10]. Such quantum state engineering requires a large number of qubits which can be precisely controlled, yet are isolated from undesired signals in the environment.

This desire to create a clean, controllable quantum system has generated a diverse variety of platforms, including (but far from limited to) trapped ions [11], neutral atoms [12], and superconducting circuits [13]. Although each of these continue to show rapidly improving control, as a rule they have unique benefits and drawbacks, and no one platform is capable of all desired tasks. This raises the possibility that a combination of traditionally separate platforms, or a hybrid quantum system, may outperform any individual solution [14].

1.1 Optical mm-wave Transduction

A prototypical example of a useful hybrid quantum systems is a single-photon link between GHz and optical frequencies. Optical photons are ideal carriers of quantum information whose state can survive transit over many kilometers of fiber optic, enabling communication between distant quantum systems, or modular connections of quantum information processors [15, 16]. Meanwhile superconducting circuits operate at ~ 10 GHz microwave frequencies, and so must be kept inside a dilution refrigerator to avoid thermal photons, making long-distance state transfer impossible. Furthermore, Josephson junction based qubits have no accessible optical transitions. An external system which couples to both frequency regimes is needed. Such frequency transducers have been demonstrated using the direct electro-optic effect [17, 18] and radiation pressure in opto-mechanics [19, 20, 21, 22].

Another approach is to use atoms, which interact strongly with the electromagnetic field at their transition frequencies, including ground-state optical transitions and Rydberg-Rydberg transitions which occur over a large range, including GHz frequencies [23]. The combination of huge Rydberg dipole moments and large ensembles are predicted to enable transduction bandwidths of hundreds of kHz or even several MHz [24, 25]. However, to date atomic transducers have only been experimentally implemented in a classical regime [26, 27], due to the difficulty of integrating Rydberg atoms into a hybrid system.

The system described in this thesis takes this approach, using Rydberg atoms to couple to both optical and GHz frequency fields. However, instead of operating at microwave frequencies in the 10 GHz range, we elect to use mm-wave Rydberg-Rydberg transitions at 100 GHz. The $10\times$ higher energy scale means thermal mm-wave photons are frozen out at a temperature of $\sim$ 5 K, 10 times higher than microwave photons, as shown in Figure 1.1, enabling single-photon experiments without the cost and inconvenience of a dilution refrigerator. In addition, 100 GHz transitions are accessible at lower Rydberg states $n = 36$, rather than $n = 100$ for 10 GHz transitions. As the Rydberg d.c. polarizability scales

as n^7, these lower states are dramatically less sensitive to technical noise from stray electric fields. Although there are a number of proposals for Rydberg-based interconverters at 10 GHz and methods to reduce sensitivity to d.c. fields [28], these schemes remain experimentally challenging.

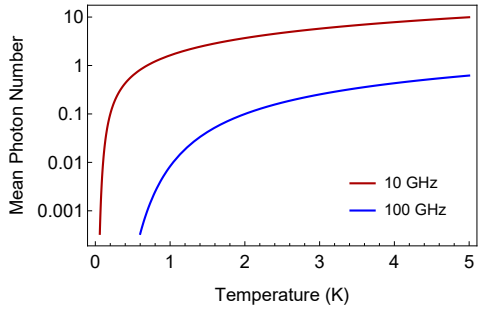

Figure 1.1: **Mean thermal photon occupation of microwaves and mm-waves.**

Transduction at mm-wave frequencies also has fundamental benefits for interfacing with quantum computers from a heat load perspective. Any transduction scheme requires pump photons to bridge the energy gap between input and output frequencies, which are lost with some probability. This imposes a heat load per converted photon proportional to the output frequency, so that direct conversion from microwave to optical frequencies may overwhelm a dilution refrigerator's cooling power at large conversion bandwidth. By upconverting first to 100 GHz on the dilution refrigerator stage, then to optical frequencies on a higher cooling power stage, this limitation on conversion bandwidth is drastically reduced [29].

1.2 Hybrid Cavity QED

In cavity QED experiments, the usefulness of mm-wave atomic transitions was early recognized for the large Rydberg dipole moments and lifetimes, and the availablility of superconducting resonators. The first demonstration of cavity Rabi oscillations in occured with a thermal beam of sodium Rydberg atoms traversing an 82 GHz resonator [30], and later the coupling of single atoms traversing a cavity was demonstrated by a single-atom maser operating at 21 GHz [31]. Later experiments showed direct evidence of field quantization [32] and Schrödinger cat states of the cavity field [33].

By 2004, cooling and trapping of ground state atoms allowed direct observation of vacuum Rabi splitting in *optical* resonators with a single trapped atom, rather than an average over many single atoms traversing a cavity [34, 35]. Single atom strong coupling led to photon blockade antibunching of the transmitted cavity field [36]. Since then, the toolbox for controlling optical light with cavity QED has progressed rapidly, leading to single and paired photon sources [37, 38], quantum memories [39], and quantum gates [40].

If atoms in a cavity can engineer interesting dynamics for light, the reverse is also true. Many atoms coupled to a shared cavity mode see an effective atom-atom interaction. This has been used to generate a variety of Hamiltonians for simulations of quantum phase transitions [41, 42]. Cavity-mediated interactions can also be used to produce specific useful quantum states. An off-resonantly driven cavity creates an effective one-axis twisting Hamiltonian [43], leading to squeezed states where entanglement-induced correlations between particles enable useful metrological gain [44, 45, 46]. Interactions between particles have also been used for enhanced readout protocols [47], leading to metrological sensitivity two orders of magnitude beyond the standard quantum limit [48]. At long times, one-axis twisting dynamics even produce "oversqueezed," non-Gaussian states, including maximally entangled GHZ states [49, 8].

It is in this context that we are once again interested in the exceptional properties of mm-wave transitions between Rydberg states. Light-induced squeezing schemes are fundamentally limited by loss of the cavity photons, or loss of the atomic states they excite. The figure of merit for these systems is the single-atom cooperativity $\eta = \frac{4g^2}{\kappa\gamma}$ [50], relating the atom-cavity coupling rate g to the cavity and atom loss rates κ, γ. Useful entanglement amongst N atoms can be generated so long as $N\eta \gtrsim 1$ [44, 45, 49]. However, reaching Heisenberg-limited metrology requires $\eta \sim N$. Our system has the potential to place thousands of cold Rydberg atoms in a resonator with a cooperativity $\eta \sim 10^4$, compared to a state of the art of $\eta = 145$ in optical cavities [51]. In addition to enabling entanglement of

many atoms, this strong nonlinearity from the mm-wave cavity can be transferred to the optical domain through EIT. Although we have not achieved these cooperativities in the current experiment, the quality factor of our mm-wave resonators will increase by a factor of 1000 when the system is upgraded from a 5 K to a 1 K cryocooler, providing a clear path forward.

An important part of this thesis is the construction of a hybrid quantum experiment. Any given qubit implementation is sensitive to certain sorts of environmental perturbations, and must be isolated from these effects. A hybrid quantum experiment has more sorts of components and is sensitive to more sorts of perturbations. Millimeter waves require low temperatures, Rydberg atoms are decohered by electric fields, and optical cavities require sub-angstrom vibrational stability. Integrating these often conflicting requirements into a single experiment is challenging, and two chapters of the thesis will cover the tools I have built to do so.

1.3 Thesis Layout

The experiment presented here centers on a sample of rubidium atoms coupled to two resonators simultaneously, so Chapter 2 will introduce the formalism of cavity QED. I will begin with the paradigmatic Jaynes-Cummings model, in which a single atom in a cavity produces a large photonic nonlinearity. Introducing multiple atoms in the cavity enhances the light-matter interaction strength, but removes the nonlinearity that comes from atomic saturation. Using cavity Rydberg EIT, a collective atomic excitation can be transformed into a collective Rydberg excitation, which may then interact with a mm-wave resonator. I will explain how the mm-wave resonator can be used to induce an all-to-all interaction among the atoms, restoring a strong nonlinearity, or alternatively to facilitate transduction between optical and mm-wave frequencies. Along the way the all-important cavity QED parameter called cooperativity will be introduced.

Chapters 3 and 4 will describe the hybrid experimental apparatus. Chapter 3 focuses on novel techniques for trapping atoms in a cryogenic environment, construction of hybrid optical mm-wave resonators, the laser system, and magnetic field control in a superconductor. The chapter will conclude with early results from the experiment, with a signature of coupling between a single Rydberg polariton and the mm-wave resonator.

Chapter 4 is devoted to a deeper discussion of the effort to stabilize optical cavities to sub-angstrom precision despite strong vibrational noise from a cryocooler. I will describe the design of our custom low-vibration cryostat, early generations of unstable cavities, and the mechanical theory which allowed us to pinpoint the flaws in those cavities. Finally, I will describe the new generation of optical resonators which are rigidly stabilized by compliant springs to the necessary precision.

Chapter 5 introduces a mathematical description of all-resonant transduction using an atomic ensemble in a cavity. The system is currently being upgraded with the necessary ultraviolet optics for mm-wave to optical transduction, but internal efficiencies $> 90\%$ and bandwidths of ~ 3 MHz are predicted.

Finally, Chapter 6 extends the concepts of impedance matching from frequency transduction to the spatial domain, enabling near-unity conversion between spatial modes of light in optical cavities.

CHAPTER 2

CAVITY QED

Interacting photons are a promising tool for distributed quantum networking, quantum information processing, and simulation of many-body systems. However, because light in a vacuum is non-interacting, as can be seen from the linearity of Maxwell's equations, interactions between photons must be engineered using a matter-based mediator which itself interacts with the electromagnetic field.

Optical crystals with nonlinear properties allow effective optical interactions, with important applications including sum and difference frequency generation, optical parametric amplification, and four-wave mixing. However, these phenomena require strong optical drives involving many photons to achieve a nonlinear effect.

Atomic systems can mediate extraordinarily strong light-matter interactions. Indeed, one important application of the system described here is to enable efficient four-wave mixing, which is a classical nonlinear process. However, atomic systems are even able to achieve strong nonlinearity at the single-photon level, where the behavior is strongly altered by the presence of a single photon. This opens the possibility of true single-photon interactions.

This chapter offers an introduction to the interaction of an atom or atomic ensemble with quantized light in an optical cavity, known as cavity quantum electrodynamics (cQED). We will begin with a single atom coupled to the modes of a closed cavity, described by the Jaynes-Cummings Hamiltonian. We will then treat coupling to the environment in the Heisenberg picture using input-output formalism, and adapt this approach to an approximate treatment using non-Hermitian Hamiltonians. The latter approach provides a natural method for restricting to a privileged subset of the Hilbert space, which is extremely useful for analyzing nonlinear and many-atom systems.

We will then place a large ensemble of atoms into the cavity, which enhances the light-matter interaction, but removes nonlinearity from the system. A Jaynes-Cummings type

nonlinearity can be recovered by simultaneously coupling the atoms to an additional resonator, this time at mm-wave frequencies. This nonlinearity can be transfered to the optical domain, and can be extremely strong compared to traditional optical nonlinearities. Finally, we will introduce the problem of impedance-matched transduction in atomic systems, whose efficiency is set by a single parameter called the cooperativity which quantifies the light-matter interaction. Later on in Chapter 5, we will see how *both* optical and mm-wave transitions can be collectively enhanced for efficient transduction between the two frequencies.

2.1 Quantized Light-Matter Interaction

We begin with a brief derivation the Jaynes-Cummings model, which is the prototypical example of quantized light coupled to matter. A quantized electromagnetic field in a closed cavity is coupled to a single atom.

The uncoupled electromagnetic field is quantized in the usual way[1]. Then, the coupling between the field and an atom is written in the dipole form, whose derivation can be found in standard textbooks [52, 53]. The total Hamiltonian is:

$$H = \sum_i \hbar\omega_i \left|i\right\rangle \left\langle i\right| + \sum_k \hbar\omega_k \left(a^\dagger a + \frac{1}{2}\right) - \boldsymbol{d}\cdot\boldsymbol{E} \tag{2.1}$$

1. Quantization of the field, in broad strokes, proceeds by decomposing the classical electromagnetic fields into uncoupled normal modes, yielding a vector potential of the form $\boldsymbol{A}(\boldsymbol{r},t) = \sum_{\boldsymbol{k}} \alpha_{\boldsymbol{k}}(t)\boldsymbol{f}_{\boldsymbol{k}}(\boldsymbol{r}) + c.c.$, where each mode oscillates at a single frequency $\alpha_{\boldsymbol{k}}(t) = \alpha_{\boldsymbol{k}}(0)e^{-i\omega_{\boldsymbol{k}}t}$ and $\omega_{\boldsymbol{k}} = c|\boldsymbol{k}|$. The spatial mode functions $\boldsymbol{f}_{\boldsymbol{k}}(\boldsymbol{r})$ satisfy the specified boundary conditions and are normalized over the integration volume as $\int_V |\boldsymbol{f}(\boldsymbol{r})|^2 d^3r = 1$. Dropping the $\boldsymbol{k}$ index for now, each mode is then written in terms of a unitless function $a(t)$ by defining $\alpha(t) = i\sqrt{\frac{\hbar}{2\omega\epsilon_0}}a(t)$ (this choice of constants will ensure the energy of a single photon is $\hbar\omega$). The functions $a, a^\dagger$ are then quantized by imposing the commutation relation $[a, a^\dagger] = 1$. The EM Hamiltonian becomes $H = \sum_{\boldsymbol{k}} \hbar\omega_{\boldsymbol{k}} \left(a^\dagger_{\boldsymbol{k}} a_{\boldsymbol{k}} + \frac{1}{2}\right)$. Finally, the electric and magnetic field operators are easily obtained by their usual definition in terms of the vector potential: $\boldsymbol{E}(\boldsymbol{r},t) = -\partial_t \boldsymbol{A}(\boldsymbol{r},t) = -\sqrt{\frac{\hbar\omega}{2\epsilon_0}} f(\boldsymbol{r})a(t) + h.c.$, $\boldsymbol{B}(\boldsymbol{r},t) = \boldsymbol{\nabla}\times\boldsymbol{A}(\boldsymbol{r},t) = i\sqrt{\frac{\hbar}{2\omega\epsilon_0}}\boldsymbol{\nabla}\times f(\boldsymbol{r})a(t) + h.c.$

where $\hbar\omega_i$ is the energy of the atom in state i, a_k is the annihilation operator for a photon in mode k with energy $\hbar\omega_k$, $\boldsymbol{E}$ is the electric field operator, and $\boldsymbol{d} = e\boldsymbol{r}$ is the atomic dipole operator.

For alkali atoms, only the single valence electron has a significant interaction with light, and the atomic dipole operator can be written as

$$\boldsymbol{d} = \sum_{ij} |i\rangle \langle i| \boldsymbol{d} |j\rangle \langle j| = \sum_{i<j} \boldsymbol{d}_{ij} \left(\sigma_{ij} + \sigma_{ji}\right) \tag{2.2}$$

where $\boldsymbol{d}_{ij} = \langle i| \boldsymbol{d} |j\rangle$, and $\sigma_{ij} = |i\rangle \langle j|$ is the atomic transition operator from state $|j\rangle$ to state $|i\rangle$. Note we have used $\boldsymbol{d}_{ij} = \boldsymbol{d}_{ji}$, and we also have $\boldsymbol{d}_{ii} = 0$ due to parity.

In the long-wavelength (or dipole) approximation, the electric field is evaluated at a single position $\boldsymbol{r}_0$ representing the atomic center of mass, which is accurate as the electron wavefunction of size $\sim a_{Bohr}$ is much smaller than the optical wavelength. Then the interaction Hamiltonian takes the form

$$H_{int} = -\boldsymbol{d} \cdot \boldsymbol{E}(\boldsymbol{r}_0) \tag{2.3}$$

The electric field at position $\boldsymbol{r}_0$ is given by $\boldsymbol{E}(\boldsymbol{r}_0) = -\sum_k \sqrt{\frac{\hbar\omega_k}{2\epsilon_0}} \left(\boldsymbol{f}_k(\boldsymbol{r}_0) a_k + \boldsymbol{f}_k^*(\boldsymbol{r}_0) a_k^\dagger\right)$, where $\boldsymbol{f}_k(\boldsymbol{r})$ is normalized over the mode volume.

For simplicity we will now restrict to two atomic levels g and e, so the dipole operator becomes $\boldsymbol{d}_{eg} \equiv \boldsymbol{d}$, and one cavity mode c with frequency ω_c which is nearly resonant with this transition. Later on additional atomic levels will be reintroduced. Then, defining the coupling strength $\hbar g = -\sqrt{\frac{\hbar\omega_c}{2\epsilon_0}} \boldsymbol{d} \cdot \boldsymbol{f}(\boldsymbol{r}_0)$, the interaction Hamiltonian is

$$H_{int} = \hbar \left(\sigma_{eg} + \sigma_{ge}\right) \left(gc + g^* c^\dagger\right) \tag{2.4}$$

Often an effective mode volume V is defined as if the field strength at the atom were uniform over the whole cavity, i.e. $V|\boldsymbol{f}(\boldsymbol{r}_0)|^2 \equiv \int |\boldsymbol{f}(\boldsymbol{r})|^2 d^3r = 1$, so $|\boldsymbol{f}(\boldsymbol{r}_0)| = \frac{1}{\sqrt{V}}$. Then the

coupling constant is written as

$$g = -\hat{\epsilon} \cdot \boldsymbol{d} \sqrt{\frac{\omega_c}{2\epsilon_0 \hbar V}} \tag{2.5}$$

where $\hat{\epsilon}$ is the polarization vector of the field at $\boldsymbol{r}_0$.

Dropping the vacuum field energy, the dipole approximation Hamiltonian becomes

$$H = \hbar\omega_e \sigma_{ee} + \hbar\omega_c c^\dagger c + \hbar\left(\sigma_{eg} + \sigma_{ge}\right)\left(gc + g^* c^\dagger\right) \tag{2.6}$$

2.1.1 Rotating Wave Approximation

The interaction term in the Hamiltonian is expanded as

$$H_{int}/\hbar = g\sigma_{eg}c + g^*\sigma_{ge}c^\dagger + g\sigma_{ge}c^\dagger + g^*\sigma_{ge}c \tag{2.7}$$

In the absence of interaction, the Heisenberg equation of motion for c is $\dot{c} + i\omega_0 c = 0$, a first-order differential equation with solution $c(t) = c(0)e^{-i\omega_c t}$. Similarly, $\sigma_{ge}(t) = \sigma_{ge}(0)e^{-i\omega_e t}$. Therefore in the interaction picture, we can see the first two terms in H_{int} will oscillate slowly as $e^{\pm i(\omega_e - \omega_c)t}$, while the latter two oscillate rapidly as $e^{\pm i(\omega_e + \omega_c)t}$.

As long as the coupling $g \ll \omega$, the rapidly oscillating terms will only weakly affect the dynamics and can be dropped[2]. Put another way, dropping these terms is valid so long as the coupling does not cause the interaction picture amplitudes $\tilde{c}(t)$ and $\tilde{\sigma}_{ge}(t)$ to vary at time scales comparable to ω. If they did, then many cavity longitudinal modes would have

2. This is analogous to the classical harmonic oscillator, where a second-order differential equation $\ddot{x} + \omega_0^2 x = 0$ can be reduced to a single first-order equation by defining the variable $a \equiv \dot{x} - i\omega_0 x$, so that $\dot{a} + i\omega_0 a = 0$. There is also an a^* equation, $\dot{a}^* - i\omega_0 a^* = 0$, but the two equations are uncoupled, so the second-order system is fully described by just one first-order equation. However, if damping terms are added, or if multiple oscillators are coupled (e.g. with a spring, producing terms like kx_1x_2), the differential equations for a and a^* are coupled together. In that case, the RWA approximation can be made if $g \ll \omega$. The exact solution is easy to obtain, but the RWA reduces the complexity from 2 first-order ODEs per oscillator to 1 per oscillator.
For the quantum problem, the regime where g approaches ω is known as the ultrastrong coupling regime. It can also be solved without the RWA [54, 55], but it is considerably more difficult.

to be occupied, and the single-mode approximation would not be valid anyway.

2.1.2 The Jaynes-Cummings Hamiltonian

Finally, this yields the Jaynes-Cummings Hamiltonian [56]

$$H = \hbar\omega_e\sigma_{ee} + \hbar\omega_c c^\dagger c + \hbar\left(g\sigma_{eg}c + g^*\sigma_{ge}c^\dagger\right) \tag{2.8}$$

The Hamiltonian is block diagonal, in that it only couples pairs of near-degenerate states $|n+1, g\rangle$ and $|n, e\rangle$, where the first index is the photon number and the second is the atomic state. Then defining the detuning $\delta_{ec} = \omega_e - \omega_c$, the eigenstates are found by diagonalizing each block. The energies are

$$E_{n,\pm}/\hbar = \omega_c\left(n+1\right) + \frac{1}{2}\left(\delta_{ec} \pm \sqrt{\delta_{ec}^2 + 4|g|^2\left(n+1\right)}\right) \tag{2.9}$$

For $\omega_e < \omega_c$ (negative δ_{ec}), the states are written

$$|n, +\rangle = -\cos\frac{\theta}{2}|n+1, g\rangle + \sin\frac{\theta}{2}|n, e\rangle \tag{2.10}$$

$$|n, -\rangle = \sin\frac{\theta}{2}|n+1, g,\rangle + \cos\frac{\theta}{2}|n, e\rangle \tag{2.11}$$

with

$$\tan\theta_i = \frac{2g\sqrt{n+1}}{\delta_{ec}} \tag{2.12}$$

For $\omega_e > \omega_c$ (positive δ_{ec}), the states are written

$$|n, +\rangle = \sin\frac{\theta}{2}|n+1, g\rangle + \cos\frac{\theta}{2}|n, e\rangle \tag{2.13}$$

$$|n, -\rangle = \cos\frac{\theta}{2}|n+1, g\rangle - \sin\frac{\theta}{2}|n, e\rangle \tag{2.14}$$

Meanwhile the ground state $|0, g\rangle$ is uncoupled and experiences no shift. It is useful to

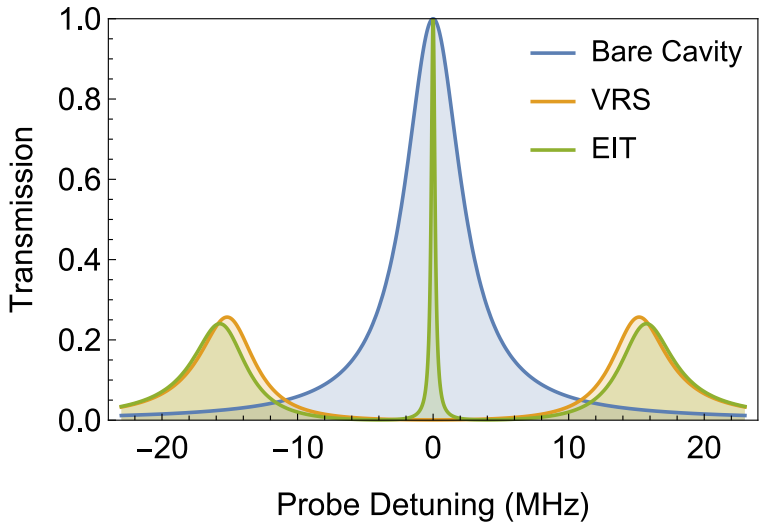

Figure 2.1: **Transmission spectra of a driven cavity with atoms.** Blue, the transmission of a bare cavity. Orange, vacuum Rabi splitting induced by atoms resonant with the cavity. Green, cavity electromagnetically induced transparency.

examine two limits for the other states:

For $g \gg |\delta|$, the eigenstates are symmetric and antisymmetric superpositions $|n,+\rangle \approx \frac{1}{\sqrt{2}}(|n+1,g\rangle + |n,e\rangle)$, and $|n,-\rangle \approx \frac{1}{\sqrt{2}}(|n+1,g\rangle - |n,e\rangle)$,. The energies are $E_{n,\pm}/\hbar \approx \omega_c(n+1) \pm |g|\sqrt{n+1}$. Even with zero photons in the system, there is a splitting between the two states, which is known as the vaccum Rabi splitting. Thus, probing the cavity in transmission, even weakly, will reveal a two-peak structure, as shown in Figure 2.1 and described more thoroughly in Section 2.3.1. The splitting is strongly dependent on the photon number, which causes a nonlinearity examined in the next section.

For $g \ll |\delta|$, the eigenstates are close to the uncoupled states, with a population admixture of magnitude $\frac{4g^2(n+1)}{\delta_e c}$. The energies are equal to the original bare energies, but Stark shifted apart by $\hbar\frac{g^2(n+1)}{\delta_e c}$.

2.1.3 Photon Blockade

The photon-number dependent splitting of the Jaynes-Cummings eigenstates can lead to a strong optical nonlinearity, which is very useful for quantum information processing appli-

cations. Under certain conditions, only one photon can be present in the system at a time, known as the photon blockade effect [57]. If a probe with frequency ω_o resonantly drives one of the $n = 0$ polaritons, say $\omega_o = \omega + g$, then the $|0, +\rangle$ state will be populated. However, the energy required to transition from $|0, +\rangle$ to $|1, +\rangle$ is $\omega + \left(\sqrt{2} - 1\right) g$. Therefore, the probe is off-resonant by $\left(\sqrt{2} - 2\right) g$. If g is much larger than the width of the eigenstates (set by loss processes examined in the next section), then a second excitation cannot enter the system.

2.2 Input, Output, and Dissipation

In our experiments, all measurements occur by probing a resonator with a probe tone, and detecting the light leaking out. Therefore, it is essential to understand how the system receives and loses energy to the outside world. This coupling of the quantum system under study to the continuum of outside modes inevitably leads to dissipative loss. In fact, coupling to a reservoir is the most natural way to treat dissipation in quantum mechanics: an ad hoc approach of adding damping terms to the Heisenberg equations of motion would lead to unphysical decay of the commutators of system operators [58].

We will begin by treating input and output in the Heisenberg picture, which allows the entire spectrum of cavity operators to be calculated. This is particularly convenient for systems with linear dynamics, including frequency transducers. Afterward, we will introduce an approximate treatment in the Schrödinger picture using non-Hermitian perturbation theory, where we can specialize to considering a few privileged states.

2.2.1 Input-Output Theory

Consider an optical cavity with one partially transmissive mirror which couples it to the environment. This derivation will borrow from Walls and Milburn [59] and Steck [53]. Then the cavity mode with annihilation operator c is supplemented by a continuum of outside modes with annihilation operators $b(\omega)$. All field operators c, $b(\omega)$ have units $\mathrm{s}^{-1/2}$. The

outside modes have commutation relations $\left[b(\omega), b^\dagger(\omega)\right] = 1$ and are coupled to the cavity mode with strength $g(\omega)$. Then dropping zero-point energy terms, the model Hamiltonian for the system is[3]:

$$H = \hbar\omega_c c^\dagger c + \hbar \int_0^\infty d\omega \omega b^\dagger(\omega) b(\omega) + \hbar \sum_\omega g(\omega) \left[b^\dagger(\omega) c + c^\dagger b(\omega)\right] \tag{2.15}$$

The Heisenberg equations of motion for the operators are then (note that while the outside modes are indexed by their center frequency ω, they still have explicit time dependence in the Heisenberg picture)

$$\dot{c} = -i\omega_c c - i \sum_\omega g(\omega) b(\omega) \tag{2.16}$$

$$\dot{b}(\omega) = -i\omega b(\omega) - i g(\omega) c \tag{2.17}$$

or, in a rotating frame $\tilde{c} = e^{i\omega_c t} c$, $\tilde{b}(\omega) = e^{i\omega_c t} b(\omega)$,

$$\dot{\tilde{c}} = -i \sum_\omega g(\omega) \tilde{b}(\omega) \tag{2.18}$$

$$\dot{\tilde{b}}(\omega) = -i\left(\omega - \omega_c\right) \tilde{b}(\omega) - i g(\omega) \tilde{c} \tag{2.19}$$

Now the latter equation is formally integrated. The initial conditions for integration can be chosen at a time $t_0 < t$, which will be seen to correspond to the "input" field, or a time $t_1 > t$, which will correspond to the "output" field. The integration can be done with an

3. This model certainly seems reasonable, but a rigorous justification is more involved. For example, when the resonator is opened to the environment, it is no longer strictly possible to define normal modes confined to the interior of the cavity, so it may be asked what exactly the operator $\hat{c}$ represents, and whether the coupling constants $g(\omega)$ can be derived from first principles. The general question of how to model open/coupled cavities with discrete modes, is relevant in both quantum and classical physics, where it is known as coupled-mode theory. One method to derive Equation 2.15 is to add an auxiliary perfectly reflecting mirror at infinite distance, and solve the exact normal modes of this system [60]. For now, we will simply begin with the present model and find that it results in a Lorentzian cavity line, which matches the classical analysis of a high-finesse cavity.

integrating factor, yielding

$$\tilde{b}(\omega) = e^{-i(\omega-\omega_c)(t-t_0)}\tilde{b}_0(\omega) - ig(\omega)\int_{t_0}^{t} dt' e^{-i(\omega-\omega_c)(t-t')}\tilde{c}(t') \tag{2.20}$$

where $t_0 < t$ and $b_0(\omega) = b(\omega, t = t_0)$, or

$$\tilde{b}(\omega) = e^{-i(\omega-\omega_c)(t-t_1)}\tilde{b}_1(\omega) + ig(\omega)\int_{t}^{t_1} dt' e^{-i(\omega-\omega_c)(t-t')}\tilde{c}(t') \tag{2.21}$$

where $t < t_1$ and $b_1(\omega) = b(\omega, t = t_1)$.

Inserting the former into Equation 2.18 and passing to a continuum limit yields

$$\dot{\tilde{c}} = -i\int_0^\infty d\omega\rho(\omega)g(\omega)e^{-i(\omega-\omega_c)(t-t_0)}\tilde{b}_0(\omega) - \int_0^\infty d\omega\rho(\omega)g(\omega)^2\int_{t_0}^{t} dt' e^{-i(\omega-\omega_c)(t-t')}\tilde{a}(t') \tag{2.22}$$

The exponential factors oscillate rapidly far from $\omega \approx \omega_c$, so we can extend the lower integration limit to $-\infty$, and assume $g(\omega) \approx g(\omega_c)$, $\rho(\omega) \approx \rho(\omega_c)$ are roughly constant in a sufficient range around ω_c, which is a Markov approximation. Then performing the integration with some delta-function tricks and finally leaving the rotating frame yields

$$\dot{c} = -i\omega_c c - \frac{\kappa}{2}c + \sqrt{\kappa}c_{in}(t) \tag{2.23}$$

$$c_{in}(t) \equiv -\frac{i}{\sqrt{2\pi}}\sqrt{\rho(\omega_c)}\int_{-\infty}^{\infty} d\omega e^{-i\omega(t-t_0)}b_0(\omega) \tag{2.24}$$

$$\kappa \equiv 2\pi\rho(\omega_c)g(\omega_c)^2 \tag{2.25}$$

where we have defined the input field operator $c_{in}(t)$ (units s^{-1}) and the constant κ. A

similar calculation substituting Equation 2.21 into 2.18 yields

$$\dot{c} = -i\omega_c c + \frac{\kappa}{2}c - \sqrt{\kappa}c_{out}(t) \tag{2.26}$$

$$c_{out}(t) \equiv \frac{i}{\sqrt{2\pi}}\sqrt{\rho(\omega_c)}\int_{-\infty}^{\infty} d\omega e^{-i\omega(t-t_1)}b_1(\omega) \tag{2.27}$$

where we have defined the output field operator $c_{out}(t)$. Finally, subtraction of Equations 2.23 and 2.26 yields

$$\sqrt{\kappa}c(t) = c_{in}(t) + c_{out}(t) \tag{2.28}$$

which says that the output field is equal to a prompt reflection of the input field with $R \approx -1$, plus a leakage field from the cavity weighted by $\sqrt{\kappa}$.

A few remarks:

1. Determination of the coupling constants: Examination of Equation 2.23 shows that κ is a Lorentzian linewidth. Comparison to the classical case yields $\kappa = 2\pi \times \frac{c}{2L\mathcal{F}}$ with finesse $\mathcal{F}$. This fixes the initially undetermined coupling constant g as $g = \sqrt{\frac{\kappa}{2\pi}}$.

2. Extension to multiple ports and arbitrary cavity Hamiltonian: suppose there are multiple ports to the environment. Also suppose the intracavity Hamiltonian is H_{sys}, which before was just $\hbar\omega_c c^\dagger c$. Then a similar derivation yields

$$\dot{c} = -\frac{i}{\hbar}\left[H_{sys}, c\right] - \frac{1}{2}\left(\kappa_1 + \kappa_2\right)c + \sqrt{\kappa_1}c_{in,1}(t) + \sqrt{\kappa_2}c_{in,2}(t) \tag{2.29}$$

and

$$\sqrt{\kappa_1}c(t) = c_{in,1}(t) + c_{out,1}(t) \tag{2.30}$$

$$\sqrt{\kappa_2}c(t) = c_{in,2}(t) + c_{out,2}(t) \tag{2.31}$$

The total cavity decay rate is now $\kappa = \sum_i \kappa_i$. Again, comparison to the classical case

tells us that κ_i is the loss rate through mirror i, with value $\kappa_i = 2\pi\frac{T_i}{T_{rt}}$, round trip time T_{rt} and mirror power transmission T_i.

3. Input field: in the absence of any input light, $c_{in}(t)$ represents a Langevin noise operator, which does not contribute to the expectation value of normally ordered operators. In this thesis we will only measure intensity and g_2, which are given by such normally ordered operators. However, if the cavity is driven by a coherent drive field of amplitude $\xi e^{-i\omega t}$ at mirror 1, then

$$\dot{c} = -i\omega_c c - \frac{\kappa}{2}c + \sqrt{\kappa_1}\xi e^{-i\omega t} \tag{2.32}$$

where we have still neglected a noise term.

This equation can be easily solved, and then the output field at mirror 2 is

$$c_{out,2} = \sqrt{\kappa_2}c, \tag{2.33}$$

giving the cavity transmission.

2.3 Non-Hermitian Hamiltonians

If Langevin noise terms are neglected in the results of the last section, then the loss term in the cavity input equation 2.32 is equivalent to modifying the cavity energy directly in the Hamiltonian as $\omega_c \to \omega_c - i\frac{\kappa}{2}$.

Atomic loss can be included in a similar way, where the decay rate $\gamma_e = \frac{\omega^3 d^2}{3\pi\epsilon_0\hbar c^3}$ is obtained by a similar calculation [61] as for the cavity known as the Wigner-Weisskopf approximation, or by Fermi's golden rule.

Meanwhile the coherent input drive in Equation 2.32 is equivalent to adding to the Hamiltonian a term $\xi\sqrt{\kappa_1}\left(ae^{-i\omega t} + a^\dagger e^{-i\omega t}\right)$. Finally, the transmitted output field is calculated

from the cavity state using Equation 2.33.

All together, this gives a prescription to calculate the cavity transmission in terms of a non-Hermitian Hamiltonian[4]:

$$H = \hbar\left(\omega_e - i\frac{\gamma_e}{2}\right)\sigma_{ee} + \hbar\left(\omega_c - i\frac{\kappa}{2}\right)c^\dagger c + \hbar\left(g\sigma_{eg}c + g^*\sigma_{ge}c^\dagger\right) + \xi\sqrt{\kappa_1}\left(ae^{-i\omega t} + a^\dagger e^{-i\omega t}\right) \tag{2.34}$$

Going into a rotating frame at the drive frequency, which amounts to examining a transformed wavefunction $|\tilde{\psi}\rangle = e^{iAt}|\psi\rangle$, with $A = \omega c^\dagger c + \omega\sigma_{ee}$, the Hamiltonian becomes

$$H = \hbar\left(\delta_e - i\frac{\gamma_e}{2}\right)\sigma_{ee} + \hbar\left(\delta_c - i\frac{\kappa}{2}\right)c^\dagger c + \hbar\left(g\sigma_{eg}c + g^*\sigma_{ge}c^\dagger\right) + \xi\sqrt{\kappa_1}\left(c + c^\dagger\right) \tag{2.35}$$

where $\delta_e = \omega_e - \omega$ and $\delta_c = \omega_c - \omega$.

2.3.1 Non-Hermitian Perturbation Theory

As we are interested broadly in single-to-few photon phenomena, the cavity will be probed only weakly. This suggests that the probe be treated as a perturbation, $V = \xi\sqrt{\kappa_1}\left(c + c^\dagger\right)$. In the absence of a probe, the atom-cavity system begins in the vacuum state $|\psi_0\rangle \equiv |0, g\rangle$, and no term in the Hamiltonian couples it to a different state. To first order in the probe, the only accessible states are the single excitation states (this will be clear in the formal treatment): $|1, g\rangle$ and $|0, e\rangle$. Then no other states enter the dynamics, and the Hamiltonian $H = H_0 + V$ can be written in matrix form:

4. Treating loss in this way allows decay from the population of one state without growth in the population of another, losing probability conservation. This treatment is identical to ignoring the $a\rho a^\dagger$ operator terms in the master equation [62]. For the present case of a single atom strongly coupled to a cavity, those terms are important. However, when we treat the case of many atoms later, the return of any given atom to its ground state is not so important, and the non-Hermitian Hamiltonian approach is very accurate.

$$H_0 = \begin{pmatrix} 0 & 0 & 0 \\ 0 & \delta_c - i\frac{\kappa}{2} & g \\ 0 & g & \delta_e - i\frac{\gamma_e}{2} \end{pmatrix}, \qquad V = \xi\sqrt{\kappa_1} \begin{pmatrix} 0 & 1 & 0 \\ 1 & 0 & 0 \\ 0 & 0 & 0 \end{pmatrix} \tag{2.36}$$

with basis vectors $|0,g\rangle = (1\,,0\,,0)^T$, $|1,g\rangle = (0\,,1\,,0)^T$, $|0,e\rangle = (0\,,0\,,1)^T$.

Because this is a non-Hermitian matrix, modifications must be made to the usual derivation of perturbation theory, which relies on the orthogonality between the eigenkets and the eigenbras. For a non-Hermitian Hamiltonian, the eigenkets and eigenbras are not necessarily orthogonal, and thus are not related by Hermitian conjugation, but by matrix inversion.

Closely following References [63, 64, 65], we begin in an initial state $|\psi_0\rangle$ which is an eigenket $H_0\,|\psi_0\rangle = \epsilon_0\,|\psi_0\rangle$. We then require that we can identify a single eigenbra $\langle\psi_0^c|$ which satisfies

$$\langle\psi_0^c|\psi_0\rangle = 1 \tag{2.37}$$

$$\langle\psi_0^c|\psi_i\rangle = 0 \tag{2.38}$$

$$\langle\psi_0^c|\,H_0 = \epsilon_0\,\langle\psi_0^c| \tag{2.39}$$

where $|\psi_i\rangle$ are the (unknown) eigenkets of H_0 besides $|\psi_0\rangle$. In our case this is satisfied by $\langle\psi_0^c| = \langle 0,g|$.

Then, perturbation theory in V yields a steady-state wavefunction $|\psi_{ss}\rangle = |\psi_0\rangle + |\psi_0^{(1)}\rangle$, with first-order correction

$$\epsilon_0^{(1)} = \langle\psi_0^c|V|\psi_0\rangle = 0 \tag{2.40}$$

$$|\psi_0^{(1)}\rangle = (\epsilon_0\mathbb{1} - H_0)^{-1}\,QV\,|\psi_0\rangle \tag{2.41}$$

where $Q = \mathbb{1} - |\psi_0\rangle\,\langle\psi_0^c|$ projects onto the subspace orthogonal to $|\psi_0\rangle$.[5]

5. In the derivation, Q arises because $\epsilon_0^{(1)}\,|\psi_0\rangle = \langle\psi_0^c|V|\psi_0\rangle\,|\psi_0\rangle = (\mathbb{1} - Q)\,V\,|\psi_0\rangle$. Similarly at second

To employ second-order perturbation theory, states in the two-excitation manifold must also be included in the Hamiltonian matrix. Then the second-order correction can be calculated as

$$\epsilon_0^{(2)} = \langle \psi_0^c | V Q G_0 V | \psi_0 \rangle \tag{2.42}$$

$$|\psi_0^{(2)}\rangle = G_0 V G_0 V \, |\psi_0\rangle \tag{2.43}$$

with[6]

$$G_0 = (\epsilon_0 \mathbb{1} - H_0)^{-1} \, Q \tag{2.44}$$

Note that higher-order corrections do not follow the simple pattern of Equation 2.43, but they will not be used in this thesis in any case.

Finally, the cavity transmission with an atom can be directly calculated from the first-order steady-state wavefunction in Equation 2.41. The output field is given by Equation 2.33, then a photodetector measures [66] $\left\langle c_{out}^\dagger c_{out} \right\rangle$. Normalized to the drive rate $|\xi|^2$, the transmission is

$$\begin{aligned} T &= \frac{1}{|\xi|^2} \left\langle c_{out}^\dagger c_{out} \right\rangle = \kappa_2 \left\langle \psi_{ss} \left| \, c^\dagger c \, \right| \psi_{ss} \right\rangle = \kappa_2 \, \langle \psi_{ss} \,|\, 1, g\rangle \, \langle 1, g \,|\, \psi_{ss}\rangle \\ T &= \kappa_1 \kappa_2 \left| \left\langle 1, g \left| \, \left(\epsilon_0 \check{\mathbb{1}} - \check{H}_0\right)^{-1} \, \right| 1, g \right\rangle \right|^2 \end{aligned} \tag{2.45}$$

where we used that $c^\dagger c = |1, g\rangle \langle 1, g|$ in the one-excitation manifold, and the superscript on $\check{\mathbb{1}}$, $\check{H}_0$ shows that they act only on states orthogonal to $|\psi_0\rangle$ (so they can be written as 2×2 matrices). For a symmetric cavity, $\kappa_1 = \kappa_2 = \frac{\kappa}{2}$.

---

order, $\epsilon_0^{(2)} \, |\psi_0\rangle = (\mathbb{1} - Q) \, V \, |\psi_0^{(1)}\rangle$.

6. We have assumed that we are in a frame rotating with the drive frequency. Often instead we will write H_0 in a frame rotating with some other frequency ω_o, so the drive has time dependence $V = \xi\sqrt{\kappa_1}\left(a e^{-i\delta_l t} + a^\dagger e^{i\delta_l t}\right)$, with $\delta_l = \omega - \omega_o$. Then going into the correct rotating frame modifies the Hamiltonian, which amounts to writing $G_0 = (\epsilon_0 \mathbb{1} + \delta_l N_{exc} - H_0)^{-1} \, Q$, where $N_{exc} = a^\dagger a + \sigma_{ee}$ is the number of excitations in the system. Note that $\epsilon_0 \mathbb{1}$ arises from a constant energy offset (zero-point energy) and will always be set to zero, while $\delta_l N_{exc}$ arises from a rotating drive term.

This expression for (lossless) cavity transmission requires only a matrix inversion, and will be applicable even for complicated Hamiltonians involving many atoms with multiple internal states! Using the Hamiltonian in Equation 2.36 gives the vacuum Rabi splitting, as described in Section 2.1.2 and shown in Figure 2.1. For a symmetric cavity, this is

$$T = \left| \frac{-i}{1 + i\frac{\delta_c}{\kappa/2} + \frac{4g^2/\kappa\gamma}{1+i\frac{\delta_e}{\gamma_e/2}}} \right|^2 \tag{2.46}$$

Meanwhile, the second-order steady-state wavefunction in Equation 2.43 can be used to calculate correlation functions in the cavity transmission.

2.4 Multiple Atoms

Our experiments will usually involve thousands of atoms in the cavity. The Jaynes-Cummings Hamiltonian is easily extended to the case of N atoms, yielding the Tavis-Cummings Hamiltonian:

$$H = \hbar\delta_c c^\dagger c + \hbar\delta_e \sum_{i=1}^{N} \sigma_{ee}^i + \hbar \sum_{i=1}^{N} \left(g_i \sigma_{eg}^i c + g_i^* \sigma_{ge}^i c^\dagger \right) + \xi\sqrt{\kappa_1} \left(c + c^\dagger \right) \tag{2.47}$$

If all atoms are identically coupled to the cavity, there are elegant treatments of their collective behavior [67, 68], in which the atoms act as a single spin vector. However, even with non-uniform couplings, a great simplification occurs by defining the collective operators

$$\Sigma_{eg} = \frac{1}{g_{coll}} \sum_i \left(g_i \sigma_{eg}^i \right) \tag{2.48}$$

$$g_{coll} = \sqrt{\sum_i |g_i|^2} \tag{2.49}$$

$$N_E = \sum_i \sigma_{ee}^i \tag{2.50}$$

and a corresponding normalized, single-excitation collective state $|E\rangle = \Sigma_{eg}|0\rangle$. Then the Hamiltonian becomes

$$H = \hbar\delta_c c^\dagger c + \hbar\delta_e N_E + \hbar\left(g_{coll}\Sigma_{eg}c + g^*_{coll}\Sigma_{ge}c^\dagger\right) + \xi\sqrt{\kappa_1}\left(c + c^\dagger\right) \tag{2.51}$$

To understand the collective states, first consider the case where the atoms are coupled identically. Then $g_{coll} = g\sqrt{N}$, representing the $\sqrt{N}$ collective enhancement of the coupling strength compared to the one-atom case. In the one-excitation state $|E\rangle$, the single excitation is shared between all atoms. Furthermore, consider the commutator $\left[\Sigma_{ge}, \Sigma_{eg}\right] = \frac{N_g - N_e}{N}$, where N_e is the number of atoms in state e. Because this commutator has no terms which change the state of any atom, the collective excitation operator is a "ladder operator": applying Σ_{eg} twice creates two excitations, then Σ_{ge} brings the system back to the unique one-excitation state $|E\rangle$, and does not couple it into other states. Thus the system will only ever go up and down the excitation ladder. There is no need to keep track of the individual atoms, only the number of collective excitations![7] Furthermore, at low excitation numbers, the commutator is nearly 1, so collective excitations are essentially bosonic.

In the one-excitation manifold, then, the accessible states are $|0, G\rangle$, $|1, G\rangle$, and $|0, E\rangle$, and we can write a non-Hermitian Hamiltonian nearly identical to the previous one. Dropping the vacuum state from the matrix, we have

$$H_0 = \begin{pmatrix} \delta_c - i\frac{\kappa}{2} & g_{coll} \\ g_{coll} & \delta_e - i\frac{\gamma_e}{2} \end{pmatrix} \tag{2.52}$$

with the only difference being g replaced with g_{coll}.

For nonuniform couplings, calculating the same commutator as before gives $\left[\Sigma_{ge}, \Sigma_{eg}\right] =$

7. The Hamiltonian contains another term $N_E = \sum_{i=1}^{N} \sigma^i_{ee}$. This term also does not couple the system outside the ladder of collective excitations. In fact, the commutator $[N_{coll}, \Sigma_{eg}] = \Sigma_{eg}$ shows that this is the number operator for collective excitations.

$\frac{1}{g_{coll}^2}\sum_i |g_i|^2 \left(\hat{\sigma}_{gg}^i - \hat{\sigma}_{ee}^i\right)$. Applied to the vacuum, this equals 1, which means there is still a unique one-excitation state $|E\rangle$, as long as we never go beyond first order. At higher excitation numbers, the commutator contains terms which change the state of individual atoms, coupling out of the collective manifold. For example, Σ_{ge} applied to the state $\Sigma_{eg}\Sigma_{eg}|0\rangle$ yields mostly $|E\rangle$, plus a small coupling to a state outside the ladder. However, this coupling is suppressed by a factor of $\frac{N_{exc}}{N}$, so it is usually negligible at low excitation numbers.

The bottom line is, to a very good approximation the system can be fully characterized by the number of collective excitations, and Σ_{eg} is nearly a bosonic operator.

2.4.1 Behavior of Collective States

A single atom, strongly coupled to a cavity, results in a large photonic nonlinearity. However, strong coupling requires the coupling strength g to be large compared to the loss rates κ, γ_e (later, we will see the degree of coupling is quantified by a single parameter called the cooperativity η). It is also technically challenging to bring just one atom into a cavity, particularly if it is to be exactly at the mode maximum.

With N atoms in the cavity, the coupling strength is enhanced by $\sim \sqrt{N}$, and each excitation is "shared" amongst the atoms with weight g_i. We will often use the enhancement of g_{coll} to define an "effective atom number" by $g_{coll} = g_0\sqrt{N_{eff}}$, where g_0 is the coupling strength for an atom at the mode maximum. This enhancement makes it much easier to reach the strong coupling regime, and avoids the technical problems of working with single atoms.

The introduction of many atoms has changed the commutation relation of a single atom, $\left[\sigma_{eg}, \sigma_{ge}\right] = \sigma_{ee}$, to just a harmonic oscillator $\left[\Sigma_{eg}, \Sigma_{ge}\right] \approx 1$. Thus we have lost the nonlinearity associated with atomic saturation, which is so useful for cavity QED! In fact, for some experiments (transduction), we will want the system to be as linear as possible, so this isn't a problem. Moreover, we will regain a Jaynes-Cummings like nonlinearity by

coupling the atoms to a second cavity at mm-wave frequencies. This nonlinearity can be transferred to the optical field, and has the potential to be extremely strong compared to what is achievable with an optical cavity alone.

2.5 Rydberg Electromagnetically-Induced Transparency

For an atom to interact strongly with mm-waves, it must be excited to a Rydberg level with principle quantum number $n \approx 36$. Thus, we now wish to add additional atomic levels to the Hamiltonian.

The simplest solution would be to use a laser at the ground-to-Rydberg transition frequency for rubidium, around 297 nm. Indeed, in Chapter 5, we will do exactly this. However, ultimately we want to interface mm-waves with an optical wavelength that is suitable for telecom fibers. Ultraviolet light is hardly ideal for this purpose, not to mention that building a high-finesse optical cavity for UV would be a challenging task. Finally, the transition is not closed, substantially decreasing the achievable atom-cavity coupling strength, which will be quantified later by the cooperativity η.

Instead, we will excite Rydberg atoms using electromagnetically-induced transparency (EIT), a two-photon scheme in which the atom is first coupled from the $|5S_{1/2}\rangle$ state (g) to an intermediate $|5P_{3/2}\rangle$ state (e) by a cavity photon at 780 nm, then to a Rydberg s state (r) by a strong classical blue beam at 480 nm. The next subsection derives the Rydberg collective states, but the reader can safely skip to the first-order matrix Hamiltonian in the following subsection.

2.5.1 Rydberg Collective States

The blue laser has frequency ω_{blue} and Rabi frequency Ω_i for the ith atom. The Hamiltonian can then be written in a frame with the cavity field and $|e\rangle$ state rotating at the drive frequency ω, while the $|r\rangle$ state rotates at $\omega + \omega_{blue}$, which amounts to examining a

transformed wavefunction $|\tilde{\psi}\rangle = e^{iAt}|\psi\rangle$, with $A = \omega c^\dagger c + \omega \sum_i \sigma^i_{ee} + (\omega + \omega_{blue}) \sum_i \sigma^i_{rr}$. Then

$$\begin{aligned} H = &\hbar\left(\delta_c - i\frac{\kappa}{2}\right) c^\dagger c + \hbar\left(\delta_c - i\frac{\gamma_e}{2}\right) N_E + \hbar\left(\delta_r - i\frac{\gamma_r}{2}\right) \sum_i \sigma^i_{rr} \\ &+ \hbar\left(g_{coll}\Sigma_{eg} c + g^*_{coll}\Sigma_{ge} c^\dagger\right) + \hbar \sum_i \left(\Omega_i \sigma^i_{re} + \Omega^*_i \sigma^i_{er}\right) + \xi\sqrt{\kappa_1}\left(c + c^\dagger\right) \end{aligned} \tag{2.53}$$

with $\delta_r = \omega_r - \omega_{blue} - \omega$.

We wish to define a collective Rydberg operator similar to Σ_{eg}. It turns out that if Ω_i are nonuniform, there is no longer a nice ladder of collective states – a method to treat this case is presented in Section 5.5. Therefore assuming uniform Ω, we define

$$N_R = \sum_i \sigma^i_{rr} \tag{2.54}$$

$$\Sigma_{re} = \sum_i \sigma^i_{re} \tag{2.55}$$

$$\Sigma_{rg} = \Sigma_{re}\Sigma_{eg} = \frac{1}{g_{coll}} \sum_i \left(g_i \sigma^i_{rg}\right) \tag{2.56}$$

where Σ_{rg} is approximately a bosonic creation operator for R type excitations, N_R counts R type excitations, and Σ_{re} converts an excitations of E type to R type. The single R excitation state is

$$|R\rangle = \Sigma_{rg}|0\rangle = \frac{1}{g_{coll}} \sum_i g_i \sigma_{rg}|0\rangle \tag{2.57}$$

where the excitation is shared among the atoms with weights g_i.

With these definition, Σ_{re} obeys exact commutation relations

$$[\Sigma_{er}, \Sigma_{re}] = N_e - N_r \tag{2.58}$$

$$\left[\Sigma_{re}, \Sigma_{eg}\right] = \Sigma_{rg} \tag{2.59}$$

$$\left[\Sigma_{er}, \Sigma_{rg}\right] = \Sigma_{eg} \tag{2.60}$$

Finally, the operators Σ_{rg}, Σ_{eg} obey quasi-bosonic commutation relations. As before, they are exactly bosonic if we restrict to one excitation, with corrections and couplings to other states of order $\frac{N_{exc}}{N}$ for higher excitation number N_{exc}. These corrections will always be ignored, so we might as well write them as bosonic operators $R^\dagger = \Sigma_{rg}$, $E^\dagger = \Sigma_{eg}$, and approximate $\Sigma_{re} \approx R^\dagger E$:

$$\begin{aligned} H = &\hbar\left(\delta_c - i\frac{\kappa}{2}\right)c^\dagger c + \hbar\left(\delta_e - i\frac{\gamma_e}{2}\right)E^\dagger E + \hbar\left(\delta_r - i\frac{\gamma_r}{2}\right)R^\dagger R \\ &+ \hbar\left(g_{coll}E^\dagger c + g_{coll}^* c^\dagger E\right) + \hbar\Omega\left(R^\dagger E + E^\dagger R\right) + \xi\sqrt{\kappa_1}\left(c + c^\dagger\right) \end{aligned} \tag{2.61}$$

Note that while g_{coll} is enhanced by the number of ground state atoms, Ω is only enhanced by the number of E and R excitations.

2.5.2 Rydberg Polaritons

Now, we can calculate the transmission spectrum with an additional atomic level. One may worry that coupling to the lossy intermediate E state would cause loss, removing the benefit of long Rydberg lifetimes. However, it is well known that a three-level atom driven on two-photon resonance experiences zero population in the middle state [69], a phenomenon called electromagnetically-induced transparency (EIT).

In this case the atoms are also in a cavity, but it turns out that the first-order Hamiltonian is the same as that for a free three-level atom. With an additional atomic sublevel, the one-excitation states are now $|C\rangle \equiv |1, G\rangle$, $|E\rangle \equiv |0, E\rangle$, and $|R\rangle \equiv |0, R\rangle$. In this basis the Hamiltonian is

$$H_0 = \begin{pmatrix} -i\frac{\kappa}{2} & g_{coll} & 0 \\ g_{coll} & \delta_{ec} - i\frac{\gamma_e}{2} & \Omega \\ 0 & \Omega & \delta_{rc} - i\frac{\gamma_r}{2} \end{pmatrix} \tag{2.62}$$

where we have gone into a frame rotating at the cavity frequency ω_c because we are initially considering no drive, and $\delta_{ec} = \omega_e - \omega_c$, $\delta_{rc} = \omega_r - \omega_{blue} - \omega_c$.

We search for an eigenstate with exactly zero population in the E state, so long as two-photon resonance is maintained. Neglecting loss rates and setting $\delta_{rc} = 0$, we look for an eigenstate $H_0 |\psi\rangle = \lambda |\psi\rangle$, where the state vector $|\psi\rangle = (A_C, A_E, A_R)^T$, and $A_E = 0$. This gives equations

$$\begin{aligned} \lambda A_C &= 0 \\ 0 &= g_{coll} A_C + \Omega A_R \\ \lambda A_R &= 0 \end{aligned}$$

The solution is the so-called "dark polariton":

$$\lambda = 0 \tag{2.63}$$

$$|\psi_D\rangle = \frac{1}{\sqrt{g_{coll}^2 + \Omega^2}} \left(\Omega |C\rangle - g_{coll} |R\rangle\right) \tag{2.64}$$

$$= \left(\cos\theta_D |C\rangle - \sin\theta |R\rangle\right) \tag{2.65}$$

where $\tan\theta_D = \frac{g_{coll}}{\Omega}$ is the dark-state rotation angle. The dark polariton is a superposition of a cavity photon and a collective Rydberg excitation, with the relative weight set by θ_D.

The two other eigenstates can be solved for:

$$\lambda_\pm = \pm\sqrt{g_{coll}^2 + \Omega^2} \tag{2.66}$$

$$|\psi_{B\pm}\rangle = \frac{1}{\sqrt{2}} \left(\sin\theta_D |G\rangle \pm |E\rangle + \cos\theta_D |R\rangle\right) \tag{2.67}$$

These are called "bright polaritons" because they have finite population in E and thus strongly scatter light.

Reintroducing loss, allowing nonzero δ_{rc}, and solving for the eigenstates, the dark polari-

ton linewidth becomes [70, 71]

$$\gamma_D \approx \kappa \cos^2\theta_D + \gamma_r \sin^2\theta_D + a\delta_{rc}^2 \tag{2.68}$$

where $a = 4\gamma_e \frac{\Omega^2 g_{coll}^2}{\left(\Omega^2+g_{coll}^2\right)^3}$. The first two terms are just loss through the cavity and Rydberg state scattering, weighted by the dark-state rotation angle. The third term introduces additional loss when two-photon resonance is broken.

Note that, so long as $\delta_{rc} = 0$, the dark polariton is unaffected by loss from the $|E\rangle$ state! Thus, when the cavity is driven on two-photon resonance, it is populated by a superposition of only a cavity photon and a long-lived collective Rydberg excitation, leading to a narrow transmission peak as shown in Figure 2.1. Controlling the blue power Ω tunes θ_D, i.e. how "cavity-like" vs "Rydberg-like" the dark polariton is, with low blue powers corresponding to Rydberg-like. The two bright polaritons also appear when probing the cavity, and are separated energetically from the dark polariton by $\sqrt{g_{coll}^2 + \Omega^2}$. We will generally be less interested in these, as they are lossy.

Using electromagnetically-induced transparency, we are able to excite Rydberg-like excitation via a convenient wavelength of 780 nm, while bypassing the loss of the intermediate state. The dark polariton inherits the properties of the Rydberg atom, and will thus strongly couple to mm-waves, with strength tunable by changing Ω.

2.6 Interfacing Atoms and mm-Waves: Strong Nonlinearity

Rydberg polaritons can interact with a mm-wave field by transitioning to a nearby Rydberg state. If this coupling is enhanced by a mm-wave cavity, then a nonlinearity very similar to that of the Jaynes-Cummings model is expected.

We introduce a mm-wave resonator with field operators b, $b^\dagger$, which is nearly resonant with the $r \leftrightarrow f$ atomic transition. Even for a λ scale resonator, the wavelength is 3 mm for

100 GHz light, so the mode is much larger than the atomic cloud, and the atom-resonator coupling is nearly a constant h. Then we can define a nearly bosonic collective operator F just as for cavity Rydberg EIT, giving

$$\begin{aligned} H = &\left(\delta_c - i\frac{\kappa}{2}\right) c^\dagger c + \left(\delta_b - i\frac{\kappa_m}{2}\right) b^\dagger b + \left(\delta_e - i\frac{\gamma_e}{2}\right) E^\dagger E \\ &+ \left(\delta_r - i\frac{\gamma_r}{2}\right) R^\dagger R + \left(\delta_f - i\frac{\gamma_f}{2}\right) F^\dagger F + \left(g_{coll} E^\dagger c + g_{coll}^* c^\dagger E\right) \\ &+ \Omega\left(R^\dagger E + E^\dagger R\right) + h\left(b^\dagger F^\dagger R + R^\dagger b F\right) + \xi\sqrt{\kappa_1}\left(c + c^\dagger\right) + \zeta\sqrt{\kappa_m}\left(b + b^\dagger\right) \end{aligned} \tag{2.69}$$

This Hamiltonian is written in the rotating frame of *both* an optical and mm-wave drive at ω_o and ω_m, respectively. This amounts to examining a transformed wavefunction $|\tilde{\psi}\rangle = e^{iAt}|\psi\rangle$, with $A = \omega_o c^\dagger c + \omega_m b^\dagger b + \omega_o \sum_i \sigma_{ee}^i + (\omega_o + \omega_{blue}) \sum_i \sigma_{rr}^i + (\omega_o + \omega_{blue} - \omega_m) \sum_i \sigma_{ff}^i$. The detunings are $\delta_c = \omega_c - \omega_o$, $\delta_e = \omega_e - \omega_o$, $\delta_r = \omega_r - \omega_{blue} - \omega_o$, $\delta_b = \omega_b - \omega_m$, and $\delta_f = \omega_f - \omega_o - \omega_{blue} + \omega_m$. In experiments with no mm-wave drive, ω_m is an arbitrary frequency, which can be set to ω_b for convenience.

As before, all atomic excitation operators are bosonic. However, unlike the EIT Hamiltonian, this Hamiltonian is *not* linear, due to the presence of nonquadratic terms $b^\dagger F^\dagger R + h.c.$. Thus, its behavior is significantly more complicated. In fact, this situation resembles the single-atom Jaynes-Cummings Hamiltonian, where the nonlinearity comes not from the atomic transition operator, but from a cubic term of bosonic operators. Instead of a single atom strongly coupled to an optical cavity, we can create a single Rydberg polariton, which is strongly coupled to a mm-wave cavity. At this point, we can observe a nonlinearity by either injecting photons into the mm-wave cavity, or injecting optical photons to create more Rydberg polaritons, each of which is strongly coupled to the mm-wave cavity.

For very weak optical probes, the system can be treated to first order in perturbation theory to calculate a linear transmission. We can follow the usual prescription and identify the one-excitation states, now indexed by $|n_c, n_b, X\rangle$, where X is one of the possible collective

atomic excitations. The accessible states are $|1,0,G\rangle$, $|0,0,E\rangle$, $|0,0,R\rangle$, and $|0,1,F\rangle$[8].

When a strong coherent mm-wave tone of amplitude β pumps the system, the system becomes approximately linear. Then the b operator can be approximated $\hat{b} \to \beta$. The nonlinear coupling term becomes $h\beta R^\dagger F + h\beta^* F^\dagger R$, which looks like a simple coherent drive of the $R \leftrightarrow F$ transition. This produces an Autler-Townes splitting of the dark polariton peak.

Otherwise, the system behaves nonlinearly. The optical transition experiences antibunching or photon blockade, which can be seen in the g_2 correlation function. To date, we have not observed the strong coupling required for VRS on the mm-wave transition, or for g_2 suppression. The reason is simply that our cryostat is too warm: the quality factor of the mm-wave resonator decreases exponentially with temperature rise, increasing the cavity linewidth and obscuring nonlinear effects. Qualitatively, the mm-wave vacuum Rabi splitting $2h$ is much smaller than the linewidth κ_m, so the peaks are not resolved. At current temperatures of ~ 5 K, the mm-wave linewidth is 4 MHz. At temperatures of 1 K, the linewidth improves to 5 kHz, a 3 order of magnitude difference. This is a planned experiment upgrade which will yield exciting new physics! It should also be noted that at current temperatures, there is a non-negligible thermal population of the mm-wave cavity. To treat that case properly, a master equation formalism should be used. Additionally, active cooling techniques using Rydberg atoms can remove thermal photons from the mm-wave mode [72].

2.7 Impedance Matching in Atomic Systems

We have seen how interfacing a Rydberg excitation with a mm-wave cavity can result in a strong photonic nonlinearity. Another interesting application of this atomic coupling to

8. The state $|0,1,F\rangle$ contains both a mm-wave photon and an atomic F excitation. If there is only an optical drive and no mm-wave drive, the Hamiltonian in Equation 2.69 always creates these two excitations together, so we need only consider states with $N_b = N_F$. Be careful, though, because as more excitations are added, the bosonic enhancement of this transition is effectively squared. If there is an additional mm-wave drive, or if there are thermal mm-wave photons, then we can no longer restrict to states where $N_b = N_F$.

the mm-wave field is photonic transduction, in which an optical excitation is absorbed by the atom-cavity system, and a mm-wave excitation is emitted (or vice versa). This is, in fact, an ideally linear process. Regardless of the incoming state of the optical field, an ideal transducer should implement a linear map $c^\dagger \rightarrow b^\dagger$.

To get a sense for how transduction works in atomic systems, we will first investigate how a single atom in a cavity can be used to efficiently scatter incoming light from a Gaussian mode into an outgoing dipole radiation pattern. This is an elastic scattering process which changes the spatial mode of light without changing its frequency, and will be described by the same Hamiltonian as the cavity-based mode converters in Chapter 6. Along the way we will encounter the extremely important cooperativity parameter, which is a figure of merit governing many cavity QED processes.

Next, we will consider the case where we want to convert an incoming optical photon into some outgoing excitation accessible from the Rydberg state. For example, the Rydberg state might be able to decay and emit a photon into a mm-wave cavity. When the Rydberg state is accessed by a two-photon EIT transition, the efficiency of this process will again depend on the cooperativity, though in a different form.

2.7.1 Dipole Emitter Impedance Matching

Consider a single atom inside an optical cavity with one partially transmissive mirror. The atom has decay rate γ_e, the cavity linewidth is κ, and the coupling between them is g. This system is described exactly by the Hamiltonian of Equation 2.36. If the cavity is weakly probed, we can use the first-order non-Hermitian perturbation theory to calculate the steady-state population of the atomic excited state, $P_e = |\langle 0, e|\psi_{ss}\rangle|^2$, and the rate of free-space scattering $\Gamma_{out} = \gamma_e P_e$. On resonance ($\delta_c = \delta_e = 0$) and normalized to the input photon rate $\Gamma_{in} = |\xi|^2$,

$$\frac{\Gamma_{out}}{\Gamma_{in}} = \frac{4\eta}{(\eta+1)^2} \tag{2.70}$$

where we have defined the all-important cooperativity

$$\eta = \frac{4g^2}{\kappa\gamma_e} \tag{2.71}$$

In the case $\eta = 1$, the efficiency of scattering is unity. Since the atom emits as a dipole, this represents a perfect mode converter between an incoming Gaussian mode and outgoing dipole radiation. Furthermore, the time-reversed calculation is identical, so if we had a source of incoming dipole radiation, an atom-cavity system could perfectly convert it to a Gaussian beam[9].

2.7.2 Cooperativity and Impedance Matching

Remarkably, the efficiency of resonant scattering does not depend on g, κ, or γ_e individually, only on the unitless cooperativity parameter. This deserves further consideration.

One interpretation of cooperativity is the ratio of the rate at which cavity photons are scatterd by the atom, given by Fermi's golden rule as $4g^2/\gamma_e$, to the rate that photons leak through the mirror, κ. Thus, at $\eta = 1$, the rate for photons leaving the two ports is exactly matched.

However, in the present case where the cavity is driven directly, the prompt reflection destructively interferes with light leaking through the mirror. At $\eta = 1$, the reflected power is exactly canceled, and all input photons leave as photons scattered by the atom. This is called impedance matching, and will be explored in greater detail in Chapter 6, in particular Section 6.2. The key point is that when in- and out- coupling rates are equal, the reflection goes to zero, and therefore all power exits through the desired output port.

In most cases, we don't wish to scatter light into free space – in fact, this is the main loss

9. With N atoms in the cavity, g receives a $\sqrt{N}$ collective enhancement, so the condition for unity scattering out of the cavity becomes $\eta = \frac{4Ng^2}{\kappa\gamma_e} = 1$. However, the light scattered outside the cavity is no longer necessarily be in a dipole pattern – having many atoms scatter together strongly affects the spatial distribution of scattered light [50].

mechanism we want to avoid. Still, cooperativity governs the efficiency of most transduction processes, including photon storage in a spin wave [73], and scattering from a Rydberg atomic state, as we will see in the next section. Cooperativity also governs many nonlinear cavity QED processes, including the number of collisions between interacting Rydberg polaritons [70], and the strength of the Jaynes-Cummings nonlinearity [74]! Roughly speaking, it determines the degree to which a nonlinearity is resolved – the Jaynes-Cummings splitting scales as g, while the widths of the eigenstates scale as κ and γ_e.

Lastly, there is a powerful result that η can be interpreted in terms of geometric parameters of the optical cavity. First we calculate the mode volume for a Gaussian mode with mode function $f(\boldsymbol{r}) = \frac{1}{\sqrt{N}}u(\boldsymbol{r})$, N is some normalization constant. Then with the mode maximum at and $\boldsymbol{r}_0$, the mode volume is

$$V = \frac{\int |u(\boldsymbol{r})|^2 d^3r}{|u(\boldsymbol{r}_0)|^2} = L\int_0^\infty e^{-2r^2/w_0^2} 2\pi r dr \tag{2.72}$$

$$V = \frac{\pi w_0^2}{2} L \tag{2.73}$$

where the integral is simplified because the power is identical through any cross section. Thus, using the expression for g in Equation 2.5,

$$g = d\sqrt{\frac{2\omega_c}{\epsilon_0 h L w_0^2}} \tag{2.74}$$

For a two-mirror cavity we multiply g^2 by an additional factor of 2 by assuming it is at the maximum of a standing wave mode, and again normalizing the mode so that one photon gives an energy of $\hbar\omega$[10].

Then we express $\kappa = \frac{c}{2L\mathcal{F}}$, where $\mathcal{F}$ is the finesse, and the atomic decay rate $\gamma_e = \frac{\omega^3 d^2}{3\pi\epsilon_0\hbar c^3}$,

10. For a running wave cavity we do not make this modification, and also we have $\kappa = \frac{c}{L}$, as each round trip involves one pass through the cavity length, not two. The result is $\eta = \frac{\mathcal{F}}{\pi}\frac{\sigma}{w_0^2}$.

to obtain

$$\eta = \frac{24\mathcal{F}}{\pi}\frac{1}{k^2 w_0^2} = \frac{4\mathcal{F}}{\pi}\frac{\sigma}{w_0^2} \tag{2.75}$$

where $\sigma = \frac{6}{k^2}$ is the atomic cross section. The cooperativity can thus be interpreted as the number of round trips a photon in the cavity makes, times the ratio of the atomic cross section to the beam area $\frac{\pi w_0^2}{2}$. In Equation 2.75, all properties of the atom other than the transition wavelength have dropped out, as has the cavity length, leaving only finesse, wavelength, and mode waist. In fact, this result can be obtained from a purely classical calculation, regarding the atom as a dipole emitter [50].

This is an extremely important result for designing optical cavities: the system's behavior will only depend on the cavity waist and finesse. For example, increasing the length of the cavity decreases g due to the larger mode volume, but this is exactly canceled by the corresponding decrease in κ. That said, while figures of merit like transduction efficiency and nonlinearity only depend on the unitless cooperativity, the experimental time scale depends on the actual rates g, κ, γ_e. Thus, for high transduction bandwidth, or taking data in a reasonable amount of time, or having coupling rates exceed decoherence from technical noise sources, shorter cavities are ideal.

2.7.3 EIT Impedance Matching

Suppose that, instead of converting an input Gaussian beam into dipole radiation, we would like to convert it into some outgoing excitation accessible only from a Rydberg state. This could be the free decay products of the Rydberg, or more practically, the Rydberg state may scatter into a mm-wave cavity at a rate $4g_m^2/\kappa_m$. In any case, we will call the rate at which the Rydberg decays κ_r (instead of γ_r, so as to emphasize that this is a desirable process instead of a loss process). To access the Rydberg state, we will use a classical EIT beam and an ensemble of atoms as before. Then the Hamiltonian in the strongly-coupled basis with

all transitions resonant is similar to Equation 2.62:

$$H_0 = \begin{pmatrix} -i\frac{\kappa}{2} & g_{coll} & 0 \\ g_{coll} & -i\frac{\gamma_e}{2} & \Omega \\ 0 & \Omega & -i\frac{\kappa_r}{2} \end{pmatrix} \tag{2.76}$$

As in the last subsection, the steady-state wavefunction can be solved, and the rate of decay from the Rydberg state is $\Gamma_{out} = \kappa_r P_R$. This rate will depend on the strength of our EIT control beam. Therefore we will optimize Ω to maximize the decay from the Rydberg state.

Before calculating the exact solution, it is useful to try to understand the process physically in the high-cooperativity case, adapted from an argument in Reference [64]. By the impedance matching argument above, we want the in- and out- coupling rates to be equal. Thus, we would like to find a steady-state where $P_C\kappa = P_R\kappa_r$[11]. An approximate dark state is given by the lossless case in Equation 2.63, yielding $\frac{P_C}{P_R} = \frac{\Omega^2}{g_{coll}^2}$. These two equations set $\Omega^2 = \frac{\kappa_r}{\kappa} g_{coll}^2$.

However, by design there is loss, and the decay from R must be scattered from population in the E state, i.e. $\Gamma_{out} = P_E \frac{4\Omega^2}{\kappa_r}$. Then the free space scattering rate is $\Gamma_{loss} = P_E \gamma_e$, and we can calculate the efficiency χ

$$\chi = \frac{\Gamma_{out}}{\Gamma_{in}} = \frac{\Gamma_{out}}{\Gamma_{out} + \Gamma_{loss} + \Gamma_{refl}} = \frac{\Gamma_{out}}{\Gamma_{out} + \Gamma_{loss}} \tag{2.77}$$

$$= \frac{4\Omega^2/\kappa_r}{4\Omega^2/\kappa_r + \gamma_e} \tag{2.78}$$

$$= \frac{\eta}{\eta + 1} \tag{2.79}$$

where in the first line we used conservation of excitation number, $\Gamma_{in} = \Gamma_{out} + \Gamma_{loss} + \Gamma_{refl}$,

11. The actual condition for zero reflection requires input rate is the sum of *all* output rates, $P_C\kappa = P_R\kappa_r + P_E\gamma_e$. For high cooperativity, loss through E is small and this is a minor correction.

and zero reflection for impedance matching, $\Gamma_{refl} = 0$.

The efficiency is thus $\frac{\eta}{\eta+1}$. Exact computation gives identical efficiency, but ideal control beam Rabi frequency $\Omega^2 = \frac{\kappa_r}{\kappa}\left(g_{coll}^2 + \frac{\gamma_e \kappa}{4}\right)$.

As in the case of dipole scattering, the efficiency here depends only on η. However, instead of $\eta = 1$, the requirement for high efficiency is $\eta \gg 1$. Why the discrepancy? For dipole scattering, η represented the ratio of the output rate to the input rate: $4g^2/\gamma_e$ to κ, which is 1 when impedance matched.

In the present case, any scattering through γ_e is considered loss. Then the efficiency $\chi = \frac{\eta}{\eta+1}$ can be easily understood in the time reversed case: a Rydberg atom is created and brought down to the E state by the control beam. From here, the excitation can be lost at a rate γ_e, or it can leave through the cavity at a rate $4g^2/\kappa$. The branching ratio for scattering through the cavity is $\frac{4g^2/\kappa}{4g^2/\kappa+\gamma_e} = \frac{\eta}{\eta+1}$. Finally, optimizing Ω ensures good impedance matching, so that there is no additional reflection loss.

CHAPTER 3

A HYBRID QUANTUM APPARATUS

This chapter will describe the construction of a hybrid cryogenic quantum apparatus capable of interfacing cold Rydberg atoms with high-finesse optical and 100 GHz mm-wave resonators. Additionally, the end of the chapter will describe early experimental results from atoms simultaneously coupled to both cavities.

The elaborate interior of the experimental chamber, shown in Figure 3.1, reflects the many requirements imposed upon a hybrid quantum system. Compared to a conventional AMO experiment, the most obvious difference is the sheer number of components, and the prevalence of copper. Of course, because a low thermal occupation is required for 100 GHz photons, the entire system must be cryogenic. Thus we will begin by introducing the custom cryogenic system built for low temperatures and compatibility with an AMO experiment. A particularly sensitive design point is the decoupling of vibrations between the cryocooler and the rest of the experiment, including the optical cavity. This will be postponed until Chapter 4 for a more complete discussion.

Next, a novel source of cold atoms, which is itself thermalized to the cryogenic environment, will be described. Cooling and trapping of alkali atoms to μK temperatures is common to many AMO experiments. However, a number of modifications had to be made to adapt these techniques to a cryogenic environment. I will then discuss the superconducting mm-wave resonators we created, how they are interfaced with optics, the use of superconductivity to create an extremely stable magnetic environment for the atom, and the use of strong mm-waves to tune the properties of our atoms. Finally, I will discuss an agile laser system which can probe a cavity even in the presence of vibrations.

In the last section of the chapter, I will present initial results from the experiment, including the observation of cavity EIT, and first signatures of coupling between Rydberg polaritons and a mm-wave resonator with sub-photon occupation.

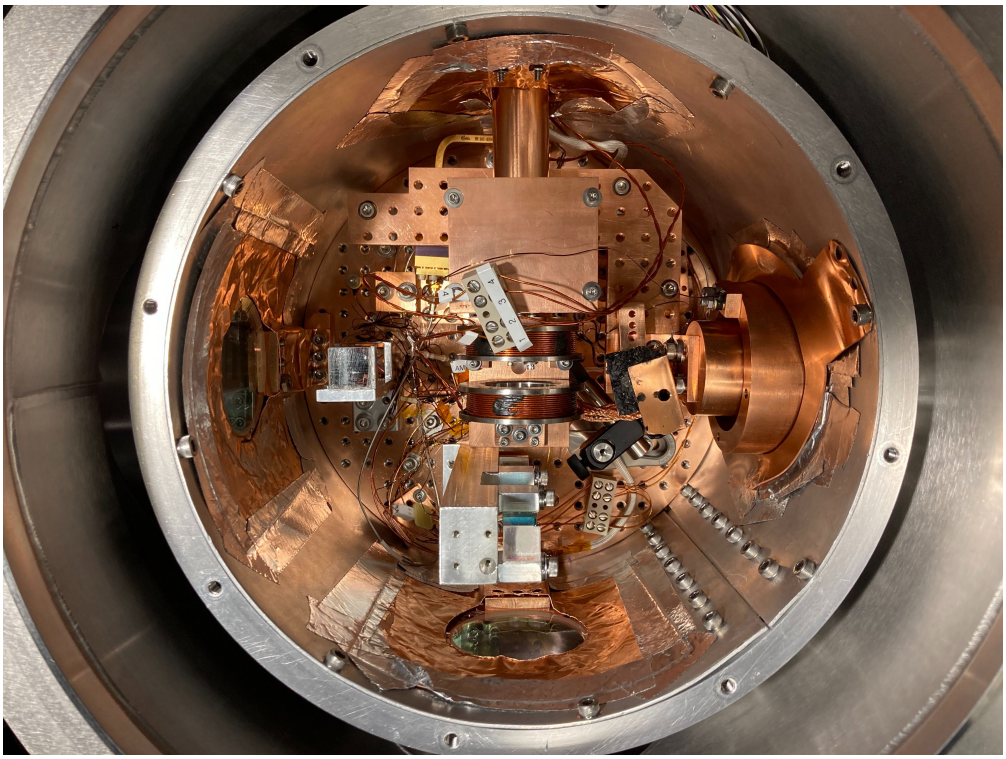

Figure 3.1: **Science chamber interior.** A top view of the science chamber showing MOT, lattice, and cavity optics, atom source shield, cryogenic plates, and mm-wave circuitry.

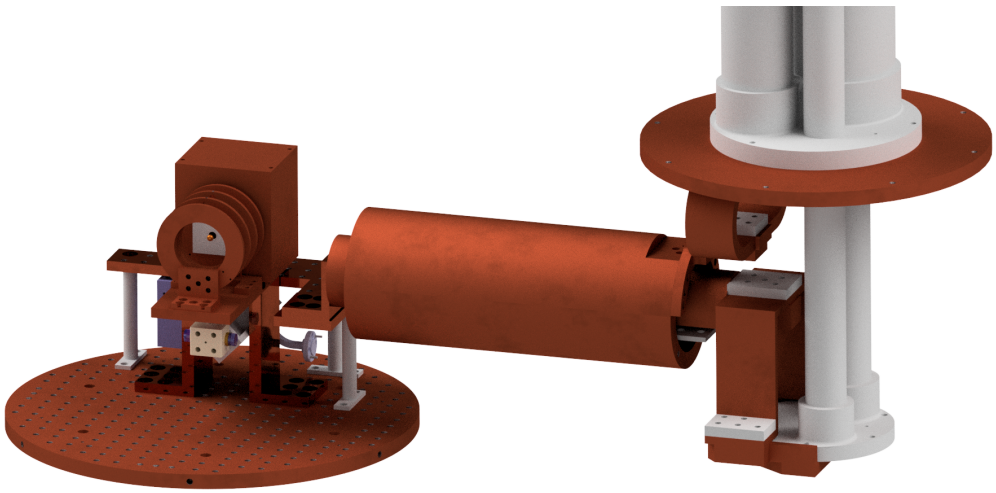

Figure 3.2: **Interior of custom two-chamber cryostat.** Thermal connection between the cryocooler and the experiment occurs via flexible braids and two long copper cold arm tubes for the 4 K and 35 K stages.

3.1 Pulse Tube Cryocooler

Cryogenic temperatures are required to freeze out thermal photons at 100 GHz, and also to be well below the superconducting transition temperature of niobium. A number of cryocooler technologies exist, from simple liquid helium bath cryostats to sophisticated dilution refrigerators capable of reaching millikelvin temperatures. We selecetd a closed cycle pulse tube cryocooler (Cryomech PT410), which is a closed system requiring no helium refilling.

Pulse tubes cryocoolers operate on a thermodynamic cycle where enthalpy flow through the cryocooler is controlled by periodic pulses of high-pressure helium [75]. Most pulse tubes have a two stage design, with a 35 K stage that has high cooling power, and a lower-temperature $\sim$ 4 K stage. Compared to other cryocooler designs, pulse tubes require no moving parts at cryogenic temperatures; however, the flow of helium still produces significant mechanical vibrations. As AMO experiments, and particularly optical cavities, are extremely sensitive to mechanical vibrations, we built a custom two-vacuum chamber design in which the cold head is mechanically isolated from the experiment. The two chambers are called the "fridge chamber" and "science chamber." Detailed analysis of the vibrational performance

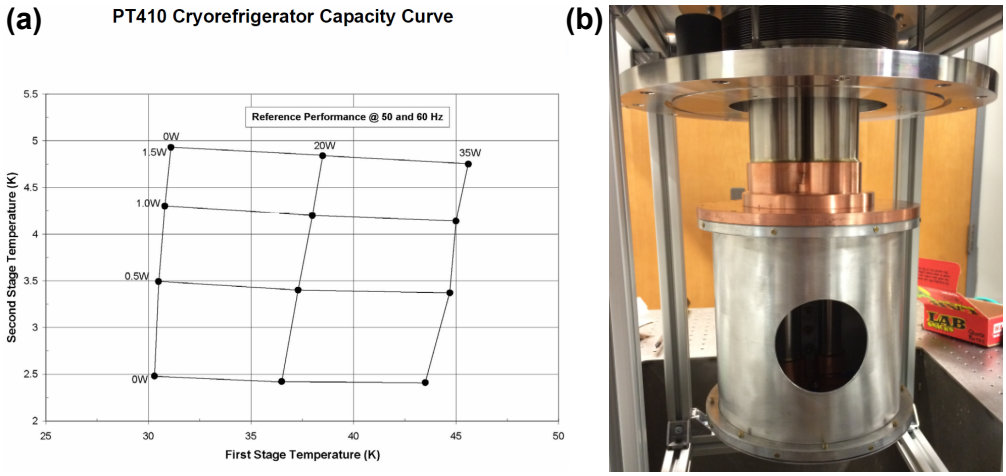

Figure 3.3: **Details of pulse tube cryocooler, (a)** Cooling capacity curve for Cryomech PT410 with base temperature ¡2.8 K, 1 W of cooling power at 4.2 K, and 40 W at 45 K, **(b),** Picture of pulse tube inserted through top flange of vacuum chamber into 35 K radiation shield.

is given in Chapter 4.

Thermal transfer between the chambers is accomplished by two cold arms made from OFHC copper, one for each stage, as pictured in Figure 3.2. The cold arms are connected to their respective stages at the pulse tube via flexible copper braids. In the science chamber a 35K plate and a 4K plate rigidly support the cold arms in a cantilevered configuration. These plates then supply the cooling power for all other components. Each has a breadboard pattern of threaded holes for convenient connections.

3.1.1 Thermal Management

The ultimate achievable temperature is a function of the cryocooler itself, the amount of environmental heat pumped into the system (heat load), and the quality of thermal connection between the cryostat and the payload. The Cryomech PT410 (with CPA298C compressor) is rated for a base temperature of 2.8 K at zero heat load. 1 W of heat load increases the temperature to 4.2 K (this is referred to as the cooling power at 4.2 K), while the other stage supports 40 W at 45 K. A full cooling power curve is in Figure 3.3(a).

Heat load increases the temperature of the cold head itself. Additionally, if the heat load is applied distantly from the cold head, a thermal gradient is esablished. This relation is usually specified by $\frac{d(T_1-T_2)}{dQ} = Z$, where Z is the thermal impedance between two points and is a function of temperature. The thermal impedance across an object can be calculated from the heat equation and known thermal conductivities. In fact, all thermal connections are made from OFHC copper to minimize Z, so the thermal gradients across these pieces are generally very small. However, bolted connections produce a large thermal impedance – the temperature mostly increases in steps between the cold head and the payload at each thermal connection.

The 4K components must be totally encapsulated by opaque 35K surfaces to absorb radiation from room temperature. Therefore, 35K radiation shields made from aluminum surround all 4K components (the shield around the pulse tube is in Figure 3.3b). The 35 K arm is a tube surrounding the 4 K arm, and a hole in each radiaton shield allows the cold arms to fit through snugly. Radiation from a black body room temperature, determined by the Stefan-Boltzmann law, is approximately 42 mW/cm^2. Up to a small geometric correction, the radiation absorbed by the 35K shields is determined by their surface area, approximately 0.27 m^2 for the science chamber and 0.18 m^2 for the fridge chamber, for a total heat load of 189 W. However, this value is diminished by a factor of the emissivity of both the emitter (stainless steel vacuum chamber) and the absorber. To reduce radiative heat load to a manageable level, the 35 K shields are covered with multilayer insulation, a layered blanket of low-emissivity mylar held apart by low-thermal conductivity polyester (sourced from OxfordICE and Talas, respectively).

Two windows in the 35 K shield provide optical access for laser beams and imaging. These are made from UV fused silica, which has high absorption of all thermal infrared wavelengths from room temperature. The windows are thermalized by clamping them against a copper ring using SEM mounting clips. As long as the windows are well thermalized and fully absorb

incoming infrared, they will appear to the 4K stage as a heat source at only 35 K.

In the science chamber, the 4K plate is mechanically supported by the 35K plate, which is in turn supported by the room temperature outer chamber. Additional heat load arises from thermal conduction through these supports, so they should be carefully designed.

Figure 3.4: Stainless steel standoffs to mechanically support and thermally insulate cryogenic plates.

Three stainless steel standoff tubes, each machined as a single piece and pictured in Figure 3.4, support the 4K plate. They are threaded on top and flare to a rectangular base at bottom to be screwed down at two points on bottom; this design prevents loosening when the 4K plate is torqued. The tubes of OD 8.9 mm are hollowed out from the bottom to a wall thickness of 0.5 mm. The length of the thin segment is 48 mm. With boundary conditions of 35 K on one side and 4 K on another, each conducts 18 mW of heat. In future the wall thickness should be decrased, but this is not the dominant heat load in our system. Similar standoffs made of G-10 fiberglass resin composite separate the 35K plate from room temperature, with negligible heat load.

The current temperature of the experimental cavity is 5 K, the cold head is 3.5 K, and the thermal impedance between the science chamber and cold head is 3.8 K/W. This suggests a heat load of about 400 mW on the 4K stage. The cooling power curve in Figure 3.3 suggests about 500 mW.

At this temperature, the mean thermal photon occupation is about 0.5, and resistive losses in the superconductor are still by far the limitation on quality factors. For future experiments, it will be imperative to reach $\sim$ 1 K temperatures through a combination of

additional cooling stages (probably a Joule-Thompson or helium sorption cooler), management of parasitic heat load, and optimization of the thermal conductivity.

Finally, we note that the cryogenic temperatures allow efficient cryopumping to reach ultrahigh vacuum levels, as contaminants are frozen, condensed, or cryo-adsorbed onto cold surfaces. A copper piece covered in activated charcoal and thermalized to 4 K aids the cryopumping due to the enormous surface area of the charcoal. Although many AMO and ion trap experiments are turning to cryogenic temperatures to reach XHV level vacuums [76], in our case it is used to have great leeway in experimental design (read: duct tape inside the chamber) while still reaching acceptable vacuum. Before cooldown, a cold cathode vacuum gauge (Pfeiffer PKR 251, mounted far from any cryogenic surfaces) measures 10^{-5} mbar, decreasing to 4×10^{-8} at cryogenic temperatures. The pressure near cryogenic surfaces is considerably better, as evidenced by atom lifetime data presented later in Figure 3.8. Because the entire experimental cycle occurs in ~ 0.1 s, extremely low pressures and long lifetimes are not required.

3.2 Cryogenic Grating Magneto-Optical Trap

As with most atomic physics experiments, ours begins by cooling and trapping atoms in a magneto-optical trap (MOT). The combination of a quadrupole magnetic field and red detuned lasers shined from all directions provides positional trapping and velocity damping in 3 dimensions. The MOT (or perhaps a collimated atom source [77, 78]) could have been constructed in a separate chamber at room temperature, with restricted optical access to prevent radiative load on the 4K stage. However, it is much more convenient to mount the MOT magnetic coils and optics directly at 35 K. This necessitated three main modifications to the conventional MOT protocol.

The atom source is one or more rubidium dispensers from SAES Getters, continuously run with 3 to 4 amps of current. The dispensers are mounted on an electrically insulating

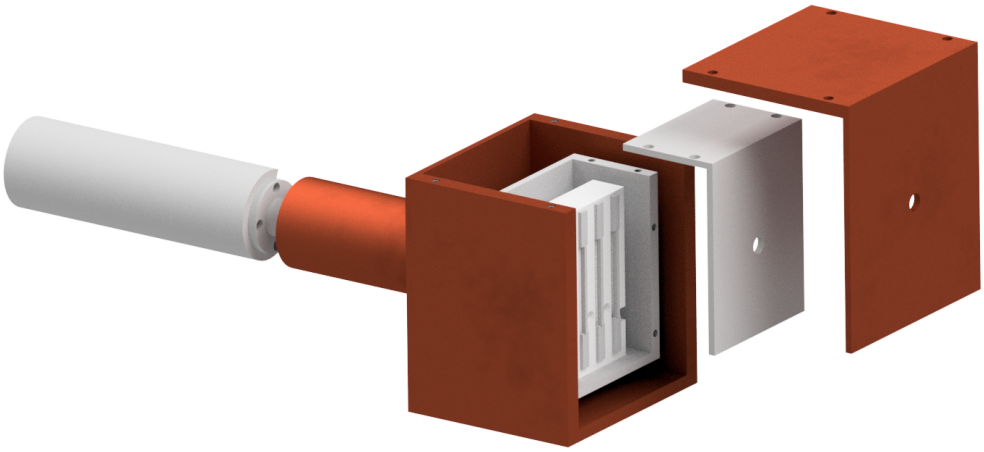

Figure 3.5: **Cryogenic atom source.** Rubidium atoms are sourced from alkali dispensers from SAES Getters. An aluminum box at room temperature surrounds the dispensers so that atoms are prethermalized to 293 K before trapping. An additional 35 K copper box surrounds this to shield the science chamber from radiation from the atom source.

block of machinable macor ceramic. In other experiments, the atoms from the dispensers fill the chamber with a background vapor of rubidium, from which a MOT can be loaded. However, our early attempts to create a MOT did not load any atoms.

To make a cryogenic atom source, the solution was to enclose the dispensers in a box that is well thermalized to room temperature, and to further enclose that in a 35 K box, as shown in Figure 3.5. The aluminum box is connected via aluminum tube to the room-temperature wall of the vacuum chamber. This arrangement performs two functions. First, it protects cryogenic surfaces from radiation from the getter, which can reach temperatures of several hundred degrees Celsius. This heat load could potentially release cryopumped contaminants from the surface, ruining the chamber pressure. Second, the room temperature box prethermalizes atoms from the very hot dispenser. In a room temperature experiment the walls of the chamber perform this prethermalization; however, in a cryogenic chamber, the atoms are likely to freeze onto surfaces [79], leaving only the direct output from the dispenser to be trapped. Unfortunately, the high temperature of atoms from the dispenser leaves very few within the MOT capture velocity [79]. Thus, the room temperature box allows atoms to prethermalize, before drifting into the MOT capture volume through consecutive holes in

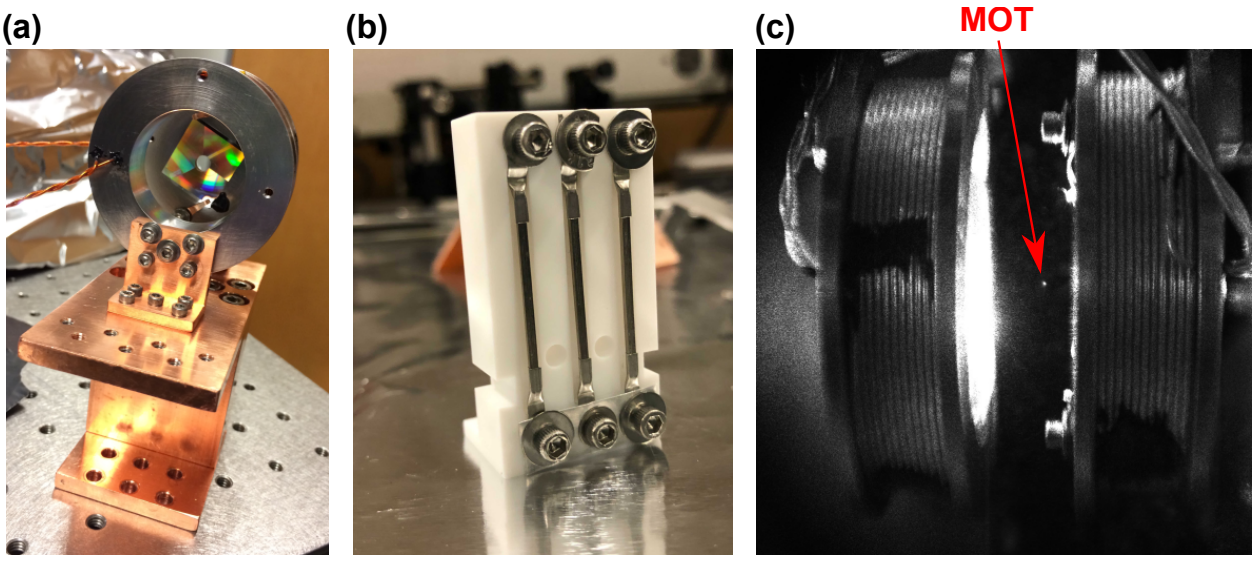

Figure 3.6: **Grating magneto-optical trap.** **(a)** Microfabricated blazed grating chip with three sections to reflect a single input beam into a tetrahedral pattern for magneto-optical trapping. **(b)** Three rubidium dispensers mounted on ceramic macor mount. **(c)** Side view of coils, with bright magneto-optical trap visible in center.

the room temp box, the 35 K box, and the back of the MOT coils.

With a functional cryogenic atom source, we create a magneto-optical trap using a single-chip MOT grating. A conventional 6-beam MOT requires significant optical access, but the science chamber has only two windows to minimize radiative heat load. The grating MOT chip, graciously provided by the Arnold group at Strathclyde [80, 81], is pictured in Figure 3.6(a). Three microfabricated blazed grating segments reflect a single 2 cm input beam into a tetrahedral pattern, providing radiation pressure along all 3 spatial axes. The chip is mounted directly onto one of the magnetic coils with SEM clips, and a hole in the grating and coil holder allows rubidium vapor to enter from the back.

Initial creation of the MOT follows the usual protocol. Two lasers described in Section 3.5, and denoted the MOT and repump lasers, are near resonant with the ^{85}Rb $|F = 3\rangle \rightarrow |F' = 4\rangle$ and $|F = 2\rangle \rightarrow |F' = 3\rangle$ transitions, respectively. The former can scatter many photons from the atomic cycling transition atoms to slow them, while the latter repumps atoms when they occasionally fall out of the cycling transition. A picture of the MOT between the

magnetic coils is in Figure 3.6(c).

Polarization gradient cooling must be slightly modified in the cryogenic environment. As usual, the quadrupole field is turned off, bias fields are adjusted to zero, laser powers are decreased, and laser detunings are increased. However, the field changes are resisted by eddy currents in surrounding high-electrical conductivity copper. The magnetic field ringdown outside the chamber was measured to have an exponential time constant of 26 ms, but using atoms as magnetic field sensors suggests a longer time constant inside the chamber, as described in Section 3.4. During this coil ringdown, we use an optical molasses stage to damp the atomic motion so that fluctuating magnetic fields do not destroy the MOT. The detunings are similar to the MOT stage, with slightly higher powers; the molasses lasts for about 20 ms. Finally, after PGC, the atomic cloud is cooled to 5 μK.

3.2.1 Optical Lattice Transport

The magneto-optical trap center is 63 mm above the mode of the optical cavity due to geometric constraints, so atoms must be transported after trapping. This is accomplished by trapping the atoms in a standing wave optical lattice formed by counterpropagating beams, and shifting the frequency of one beam [82]. The resulting intensity profile moves at a speed $v = \frac{\lambda \Delta f}{2}$, forming an optical conveyer belt.

A schematic of the lattice beam path, threaded through the MOT location and the hybrid cavity, is shown in Figure 3.7(a). Three turning mirrors each on the upper and lower paths guide the beams. The figure also shows fluorescence images of the lattice loading from the PGC (b) and after the PGC has fallen away (c). The lattice is derived from a narrow 785 ECDL amplified by a tapered amplifier. The TA output is split into two paths, each of which is frequency shifted by a double pass acousto-optic modulator, with RF tones provided by a direct digital synthesizer (DDS). The tone provided to one AOM is ramped in a triangle wave to accelerate the atoms in the lattice, then decelerate them to bring them to a stop in

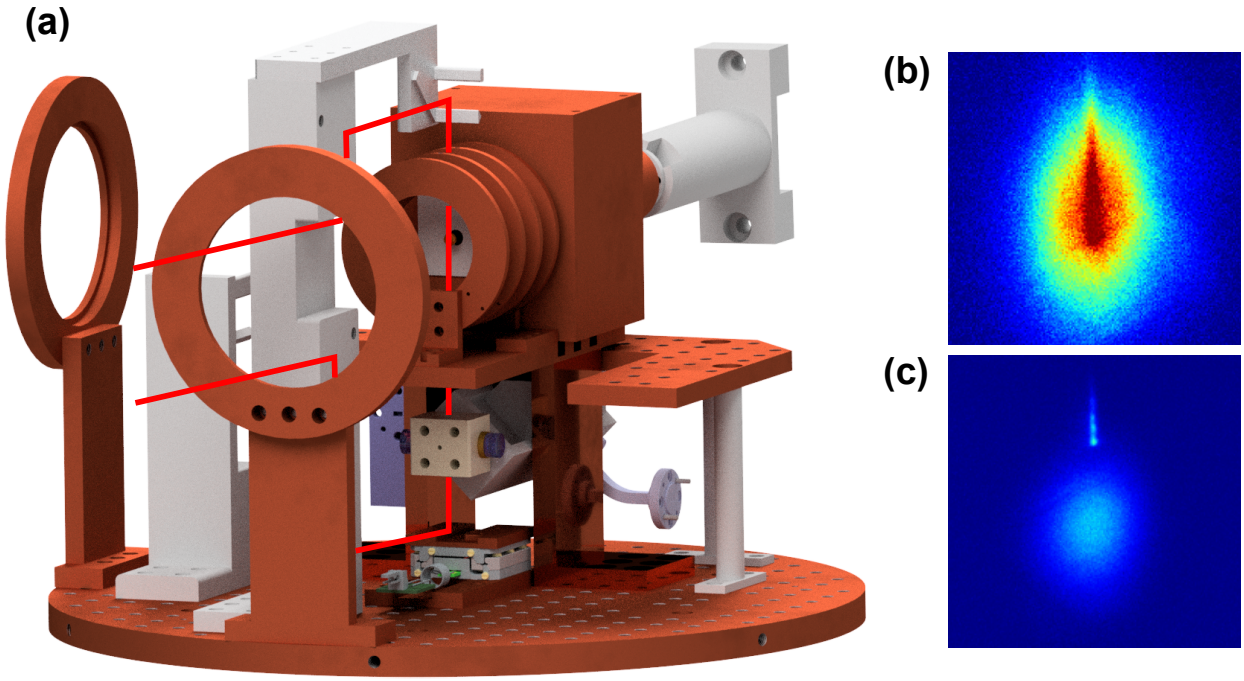

Figure 3.7: **Optical lattice transport, (a)** Diagram of transport lattice beam path threaded through MOT and hybrid cavity, **(b)** Loading of lattice from PGC-cooled atoms, **(c)** Atoms trapped in lattice as MOT cloud falls away.

the cavity. Initial lattice loading efficiency is around 30%, while transport efficiency can be in excess of 90% with accelerations up to $500g$.

The lifetime of atoms in the lattice varies strongly as a function of transport distance, as shown in Figure 3.8, from a minimum of 350 ms at the MOT position, up to 900 ms at the center of the cavity. We attribute this to the heightened cryopumping efficiency inside the cavity, which is strongly thermalized to 4K.

3.3 mm-Wave Resonators

A key feature of the experiment is a millimeter wave resonator to enhance the interaction between Rydberg atoms and the field at 100 GHz. The resonator must possess as high a quality factor and as small a mode volume as possible to achieve the highest cooperativity, while also having optical access for lasers and atoms to enter the mm-wave mode.

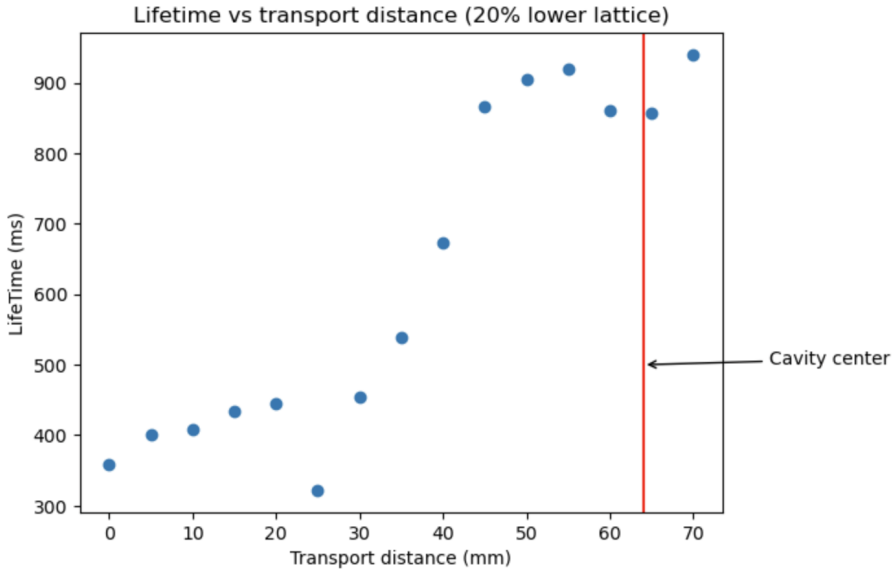

Figure 3.8: **Optical lattice lifetime versus position.** The lifetime of atoms in the lattice varies as a function of transport distance. This can be attributed to the variation in cryopumping efficiency at different positions. Near the end of the transport, the atoms enter the cavity, which is strongly thermalized to 4 K, exhibiting stronger cryopumping.

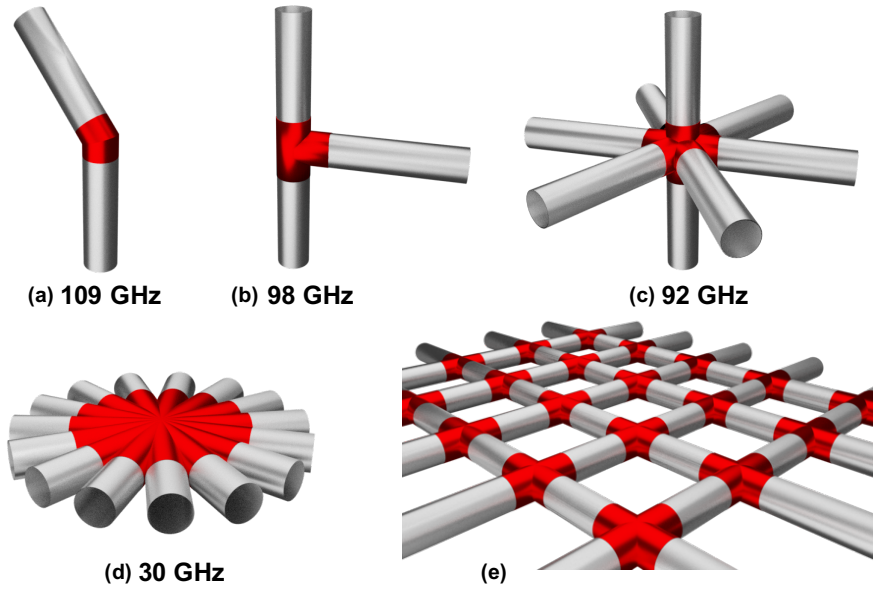

Figure 3.9: **Seamless evanescent-coupled mm-wave resonators.** A high-quality factor, low-mode volume mm-wave resonator is formed by the intersection of two or more holes in a superconductor. Altering the size or configuration of the tubes allows customization of the mode spatial and frequency structure. Figure from Reference [83].

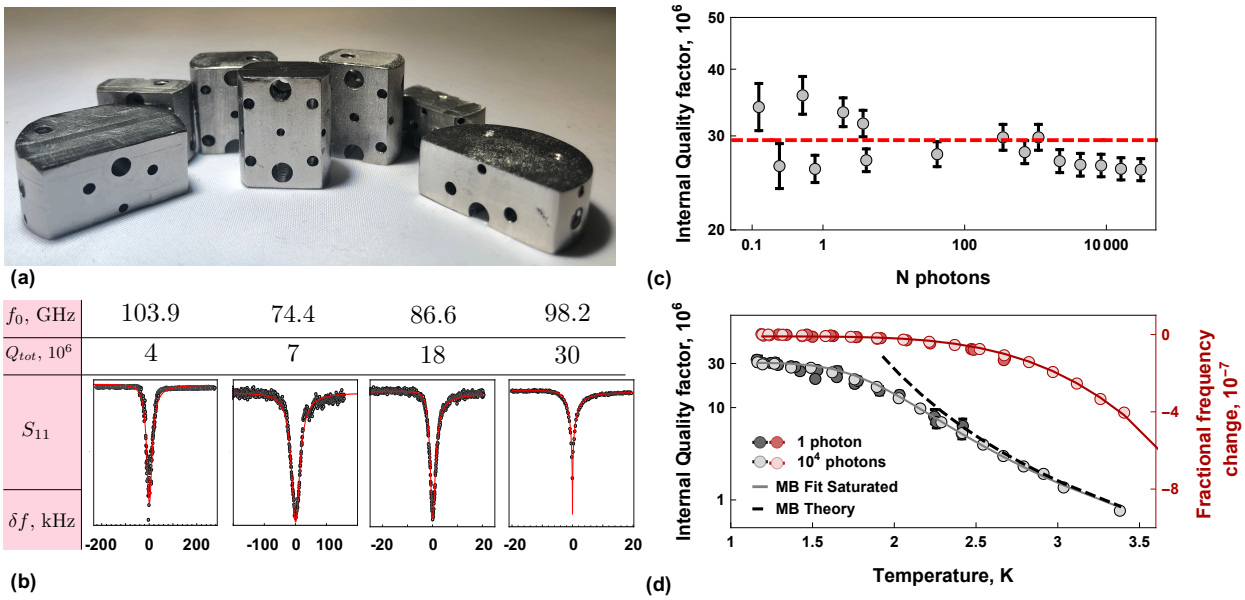

Figure 3.10: **Quality factor measurements of mm-wave resonators.** Figure from Reference [83].

To achieve this, we designed a new type of resonator based on the intersection of evanescent waveguides, as pictured schematically in Figure 3.9. Two or more intersecting holes are drilled through a piece of pure niobium. The characteristic size at the intersection is greater than that of the individual tubes, allowing a localized mode to form. The hole diameters are chosen so that they do not act as waveguides at the target mode frequency – that is, the frequency is below cutoff, and waveguide propagation is exponentially supressed with length.

This design has a number of benefits. It can be easily machined from a monolithic block of niobium and thus has no seams, leading to high quality factors. The holes provide built-in optical access for lasers and atoms. Long holes completely suppress radiative loss, while a single shorter hole can be used for coupling to the input waveguide. Finally, the geometry is very flexible, allowing for fine tuning of mode frequencies and shapes. The mode volume for our 100 GHz resonator is approximately $\lambda/10$.

An array of machined resonators is shown in Figure 3.10(a). After machining the cavities are chemically etched in a solution of H_3PO_4, HNO_3, and HF to remove surface irregu-

larities and increase quality factors. The quality factor of the resonator is determined by fitting the reflection signal according to Equation 2.28, shown in part (b). The Q increases exponentially as temperature drops below the superconducting transition, predicted by a Mattis-Bardeen fit. At 1K, Q saturates to 3×10^7, corresponding to a linewidth of only 3 kHz! Combined with a low mode volume, this will lead to very high cooperativity for Rydberg atoms. Many more details on mm-wave resonators can be found in Reference [83] and Aziza Suleymanzade's thesis.

The frequencies of the mm-wave resonators are set by the sizes and alignment of the coupling holes, which are about 1.3 mm in diameter for a 100 GHz cavity. A deviation of only 1 micron thus leads to a frequency error of order 75 MHz, much greater than the linewidth of 3 kHz. Achieving a target frequency through machining alone is unrealistic. One solution is to remove excess material through further acid etching. The etch rate can be calibrated fairly accurately, and we have can achieve precisions of 10-20 MHz in this fashion[1] Further tuning can be accomplished by squeezing the cavity in a hydraulic press, with which we have achieved several MHz precision. Finally, Section 3.3.2 will discuss methods for tuning the atoms instead with extremely high precision, and a range of several MHz.

The same cavity architecture can be used to create lower-Q bandpass filters at mm-wave frequencies, simply by shortening the tube along the coupling directions, as shown in Figure 3.11. Room-temperature aluminum filters, with no chemical etching, are sufficient to achieve Qs of 400 and 3 dB insertion loss. We have investigated using such filters to clean the output of our mm-wave sources, but they are not in use currently.

1. Tuning the cavity frequency requires repeated cycles of etching and measurement. For high Q cavities, the coupling Q is a function of the geometry and must roughly match the desired total Q, while the internal Q depends on temperature. Thus, the cavity is heavily undercoupled and impossible to measure unless at cryogenic temperatures, making the measurement process tedious. A possible solution (so far untested) is to machine the cavity for a coupling Q_l of around 1000 so it can be measured at room temperature. For final cryogenic operation, an additional length of niobium tube can be placed between the cavity and the input waveguide. The resulting seam will generate some loss, but it will be suppressed because it is already in the evanescent coupling tube.

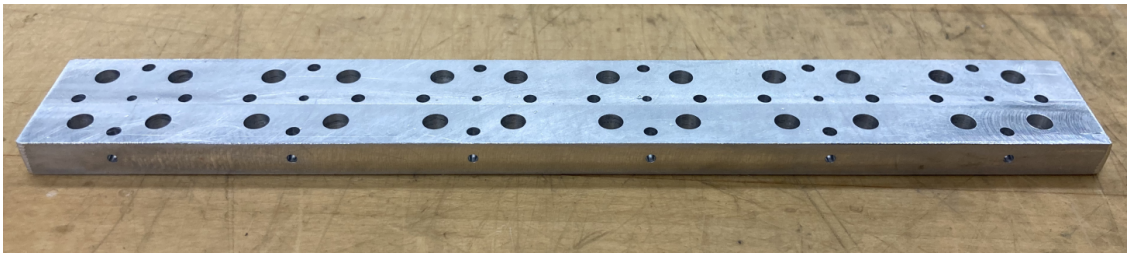

Figure 3.11: **Cavity mm-wave filters of various frequencies.** Machined mm-wave filters follow a similar design as cavities, but with shorter coupling tubes along one direction for moderate Q. These aluminum filters were machined in the CNC and have a Q of 400 with 3 dB insertion loss.

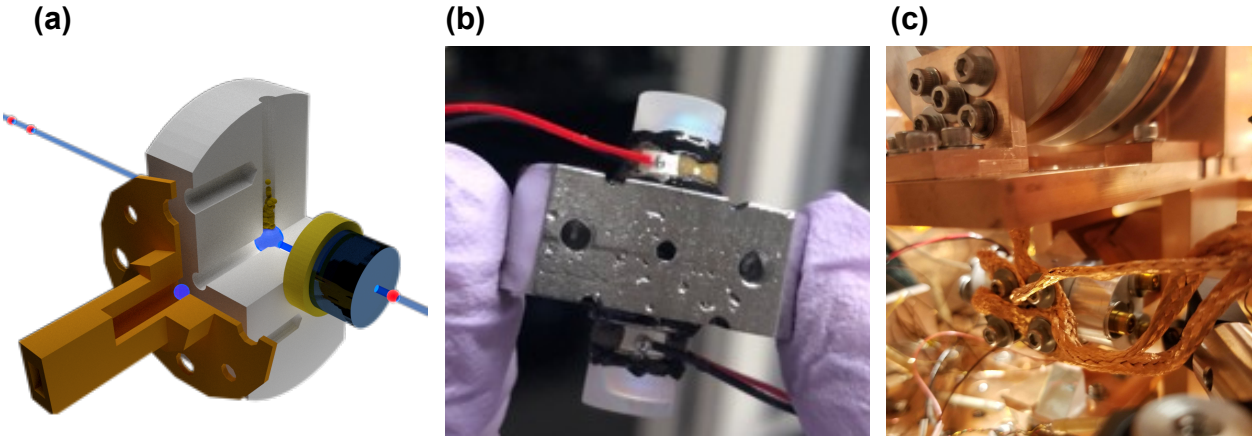

Figure 3.12: **Hybrid optical mm-wave cavity, (a)** 3D rendering with atoms and laser input, **(b)** Early hybrid cavity design with visible mirrors and piezos, **(c)** New spring-assembled cavity in place below MOT coils.

3.3.1 Hybrid Cavity

Due to the inherent optical access of this mm-wave resonator design, it is in principle simple to create a hybrid cavity: simply attach mirrors to either side of the niobium block, and their Fabry-Perot mode will intersect with the maximum of the mm-wave mode. The evanescent waveguide tubes are still much larger than the optical modes, so beam clipping is not an issue. In practice, additional problems had to be solved to create a stable, cryogenic Fabry-Perot cavity, in particular one made of dissimilar materials, which will be discussed further in Chapter 4.

Pictures of such a hybrid cavity are shown in Figure 3.12, where (a) is a CAD model, (b)

is an early cavity design, and (c) is a modern, spring-assembled cavity design fully integrated into the experiment. The cavity is attached directly to mm-wave circuitry, which places it below the magneto-optical trap. Additional flexible copper braids attach directly from the cavity to the 4K tube to increase cooling power. The result is a hybrid cavity ready to accept atoms and interface with mm-wave sources and laserse.

3.3.2 Tuning Mode

So far, we have achieved mm-wave resonant frequencies within 7 MHz of the desired atomic resonance. While this is an accuracy of 0.007%, it is still a large detuning compared to the relevant Rydberg and cavity linewidths. The resonance condition is fine-tuned by Stark-shifting the Rydberg levels with a coherent microwave tone.

The relevant section of the Rydberg manifold is shown in Figure 3.13(a), where the blue arrow represents the resonant cavity mode (science transition), and gray arrows represent the action of the tuning tone. Note that we have chosen a π polarized $|36S_{1/2}\rangle \leftrightarrow |35P_{1/2}\rangle$ transition for the science mode with respect to the cavity axis, even though a circularly polarized transition to $|35P_{3/2}\rangle$ would have a higher Clebsch-Gordan coefficient, because it is difficult to engineer circularly polarized mm-wave modes. To avoid admixture of multiple states, we have chosen the π polarization. The simulated E-field distribution of the science mode is shown in part (b) of the figure.

The tuning tone is resonantly enhanced by a second mm-wave cavity mode, shown in part (c)[2]. The orthogonal geometry of the cavity constrains the two resonant modes to have orthogonal polarizations, so the tuning mode has lin polarization.

Figure 3.13(d) shows simulated Stark shifts for an arbitrary tuning tone power (achievable with our sources) versus frequency, obtained by diagonalization of the Hamiltonian. Eigenstate overlap with three selected states are indicated by color. We choose a tuning

2. Indeed, the cavity efficiently rejects any tone which is *not* at a resonance frequency

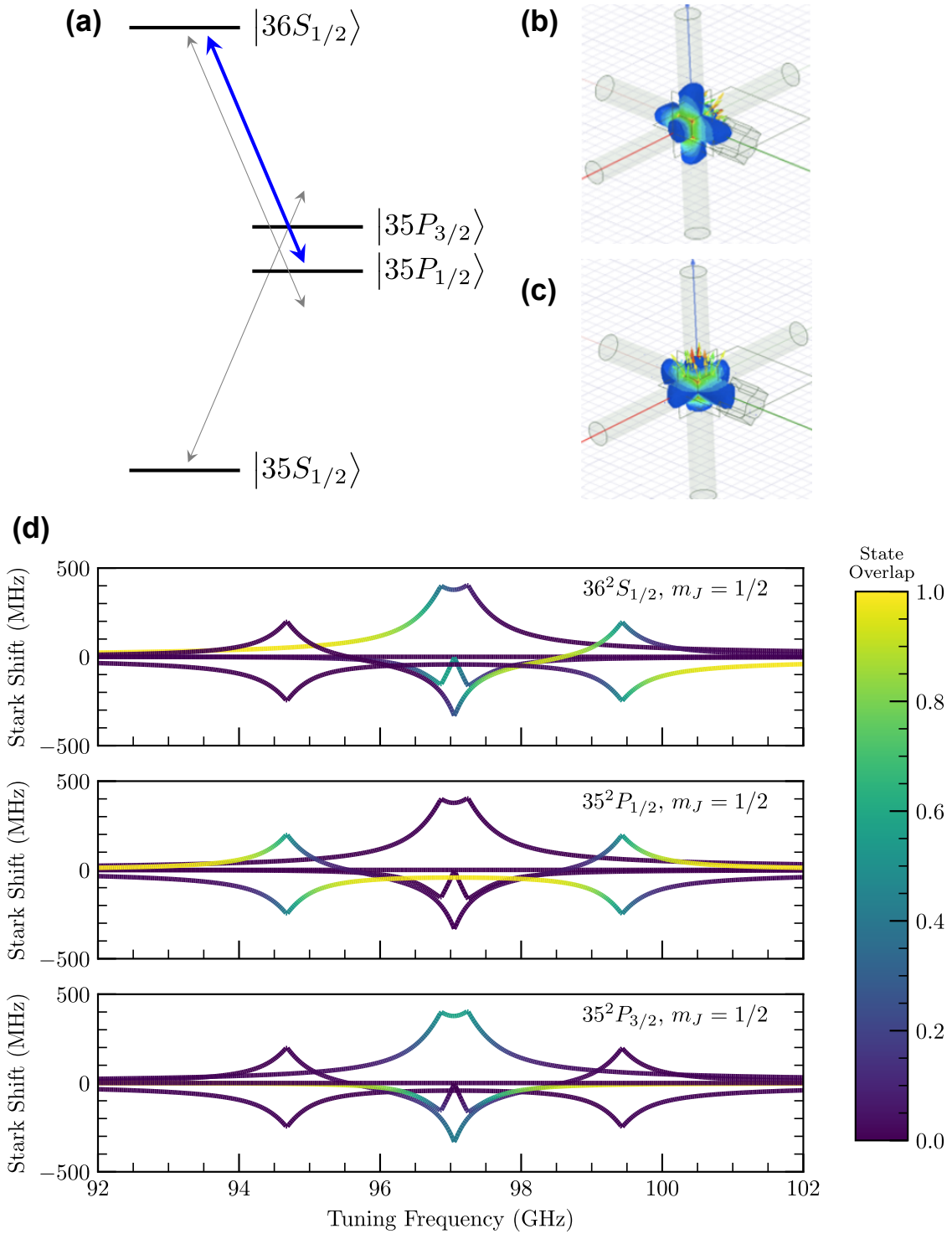

Figure 3.13: **Cavity Stark tuning of Rydberg atoms.** **(a)** In addition to a near-resonant mm-wave cavity mode, a second off-resonant mode can be for Stark shifting atomic levels. **(b), (c)** Simulated E-field distributions for the science and tuning modes, respectively. **(d)** Simulated Stark shifts for an arbitrary tuning power. Color on each plot indicates overlap with the specified state.

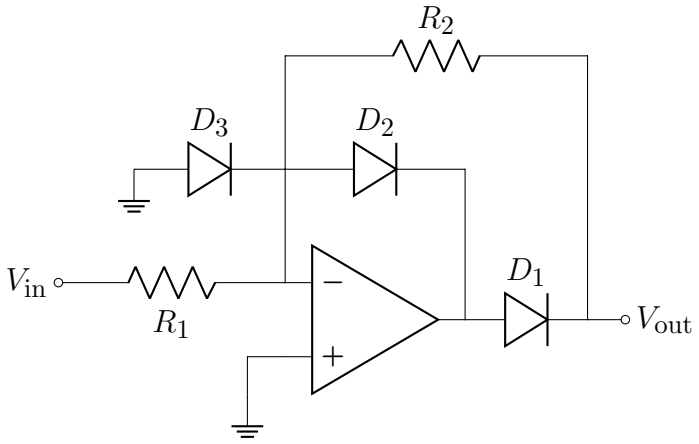

Figure 3.14: **Modified precision rectifier for mm-wave power lock.**

mode frequency near 101 GHz. At this frequency, the $|36S_{1/2}\rangle$ state energy can be easily shifted down by 100 MHz with achievable mm-wave powers, and with negligible admixture of other states. Meanwhile, the $|35P_{1/2}\rangle$ is shifted up by approximately 40% as much as the $36S$ state shifts down. State energies and matrix elements are obtained from the Alkali Rydberg Calculator package [84]. This Stark tuning scheme provides a precise method to tune atoms into resonance with the cavity.

Large Stark tuning means that a small fractional change in the mm-wave source power can move the atoms off resonance. For stable operation, the mm-wave power must be locked. The power is controlled with a voltage variable attenuator (Mi-Wave 900WF-30/387), and detected with a finline power detector (Mi-Wave 950W/387). The loop is closed through a homebuilt PI controller. Initially, the lock introduced noise into the mm-wave power which showed up as a decoherence mechanism in the Rydberg polariton linewidth. Adding an attenuator after the power detector, and severely limiting the lock bandwidth, fixed this problem, which was probably due to a lock oscillation or writing high-frequency noise into the lock. The current setup has resulted in Stark shifts of 5 MHz that are stable to at least 10 kHz, potentially better, and no broadening attributable to the lock. However, the tuning scheme itself does cause broadening, see Section 3.6.3

The mm-wave voltage variable attenuator used for power locking is intolerant of any negative voltage, but requires near-zero tuning voltage for low powers. A bipolar op-amp with a modified precision rectifier circuit, shown in Figure 3.14 allows operation down to exactly zero with no risk of negative voltage. For negative V_{in}, the circuit functions as an inverting amplifier. Since the sense resistor lies after protection diode D_1, the output voltage is not affected by the diode, and $V_{\text{out}} = -\frac{R_2}{R_1}V_{\text{in}}$. For positive input voltages, D_1 is off and conducts no current, while D_2 turns on, providing a feedback path so the op-amp does not run open loop. Since one end of R_2 is connected to virtual ground, and no current flows through it, $V_{\text{out}} = 0$. Finally, D_3 ideally has no effect, because it connects virtual ground to ground. However, if the op amp were to lose power, the negative input would pass directly through to the output; D_3 prevents such a situation.

3.4 Magnetic Field Control

The presence of superconductors and high-electrical conductivity copper at cryogenic temperatures presents interesting challenges and opportunities for magnetic field control. As already noted, atom cooling sequences must be modified to account for eddy current ring-downs.

In addition, a well-known property of superconductors is their ability to set up permanent magnetic fields. We directly observed this behavior using atoms inside the superconducting niobium resonator as probes. Figure 3.15(a) shows the EIT transmission spectrum as a function of bias magnetic field when the cavity is above the critical temperature T_c. The fields create Zeeman shifts, as expected. Below T_c, as shown in part (b), the applied bias field is completely screened by the superconductor, and has no effect on the atoms.

When the resonator is cooled below the superconducting transition temperature, the magnetic field in the holes is "frozen in." Future changes to the applied field are counteracted by currents according to Lenz's law, which persist indefinitely. Initially, this effect was

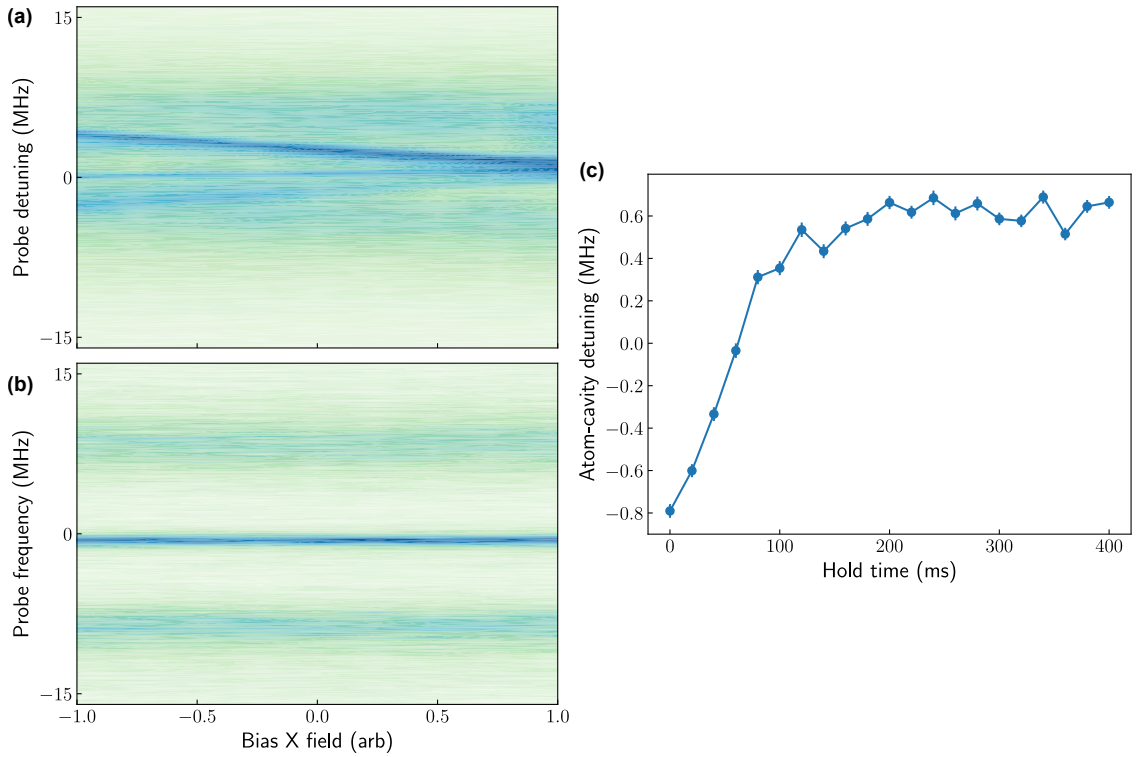

Figure 3.15: **Magnetic field control in a superconducting cavity.** **(a)** Above T_c, magnetic fields cause Zeeman shifts in the EIT spectrum. **(b)** Below T_c, external fields are screened by the superconductor, and are invisible to the atoms. **(c)** Ringdown of magnetic fields above T_c, measured by atoms.

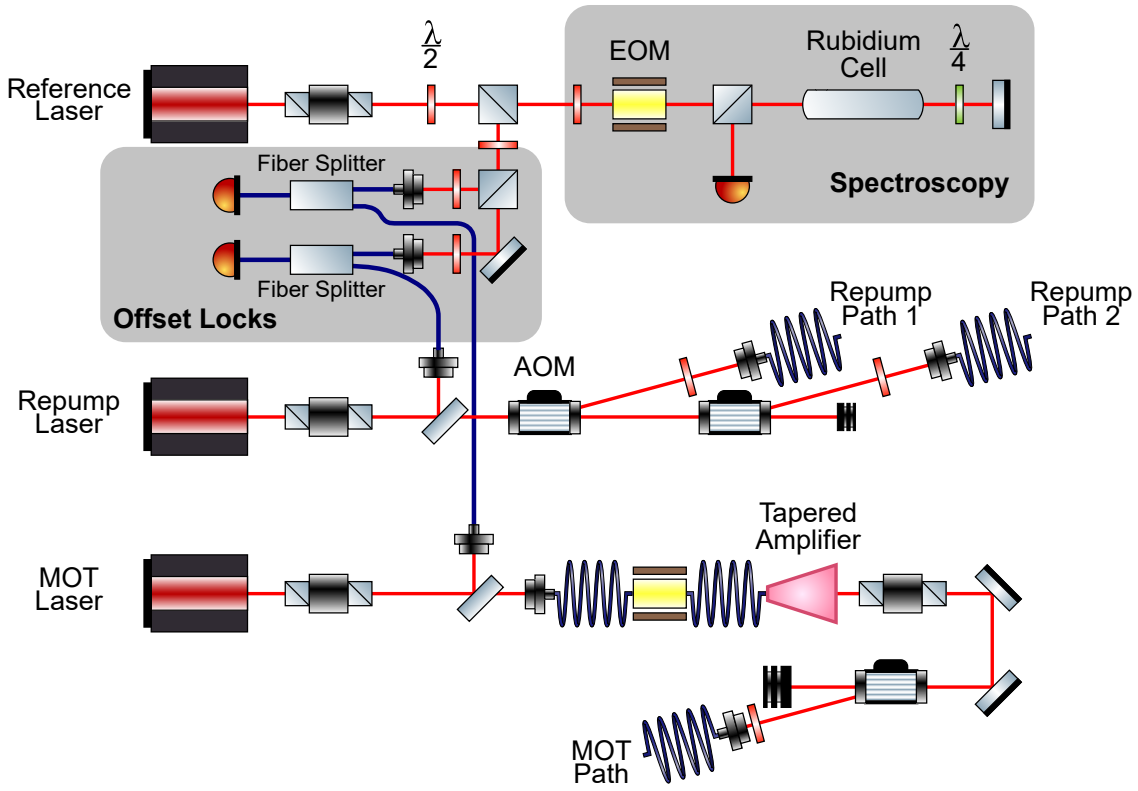

Figure 3.16: **Laser system for probing rubidium D_2 line.**

detrimental, as a random field was frozen in upon cooldown. However, by warming the cavity up, carefully optimizing the field, and cooling it back down, the field is permanently optimized, and is totally unaffected by environmental noise! Care must be taken when optimizing the fields, that they are allowed to stabilize fully. The field ringdown inside the (warm) cavity can be measured by the Zeeman shift in the atoms as a function of wait time since coil adjustment, as shown in Figure 3.15(c). The field in the cavity takes about 200 ms to stabilize.

3.5 Laser System

The laser system for probing the rubidium D_2 line is shown in Figure 3.16. All lasers are DFB diodes from Eagleyard. A reference laser is locked to via Doppler-free spectroscopy to a feature in the ^{87}Rb $|F = 1\rangle \rightarrow |F' = 2\rangle$ manifold, providing a stable frequency reference.

Two other diodes provide repumper and cycling transition light for the magneto-optical trap. The latter is amplified by a tapered amplifier, before both are fiber coupled and sent to the outside of the science chamber, where they are combined on a 50/50 beamsplitter.

The repump and MOT lasers are locked to the reference laser via beatnote offset locking. A small amount of power is split off from the laser, combined with light from the reference via a single-mode fiber splitter, and detected by a high-bandwidth photodiode (Hamamatsu G4176). The resulting signal is at the difference frequency between the lasers[3]. This beatnote is mixed down to near 200 MHz using an RF signal provided by an agile direct digital synthesizer. The signal is split, with one arm passed through a helical filter in transmission, which has a sharp resonance at $f_{hf} \approx 200$ MHz. The two arms are mixed together with the correct relative phase so there is a zero crossing at the helical filter resonance. This provides a suitable lock point. By changing the DDS frequency while in lock, the laser frequency adjusts to maintain a difference of f_{hf}.

3.5.1 Frequency Following

An additional locking scheme maintains resonance of all probe lasers with the science optical cavity, as shown in Figure 3.17. A narrow 1560 nm laser and some frequency doubled power at 780 nm are obtained from a fiber laser source in the adjacent "multimode polariton" lab. These beams are absolutely frequency stable. A transfer cavity in ultrahigh vacuum is used to transfer the stability of the 780 beam onto our 480 nm EIT control laser, so that the 480 nm laser can be absolutely stable at an arbitrary frequency.

With all lasers stable, an electro-optic modulator (EOM1) generates a sideband of the 780 nm beam at exactly the $|F = 3\rangle \rightarrow |F' = 4\rangle$ atomic resonance frequency. The cavity

3. The beatnote's signal-to-noise ratio is fundamentally limited by shot noise, but can also be limited by technical noise in the detection. If one laser is much stronger than the other, then both the signal and the noise scale with the square root of this beam's power. The power should be increased until shot noise determines the noise floor as measured on a spectrum analyzer, rather than technical noise. Past this, the SNR does not improve unless the other beam's power can be increased.

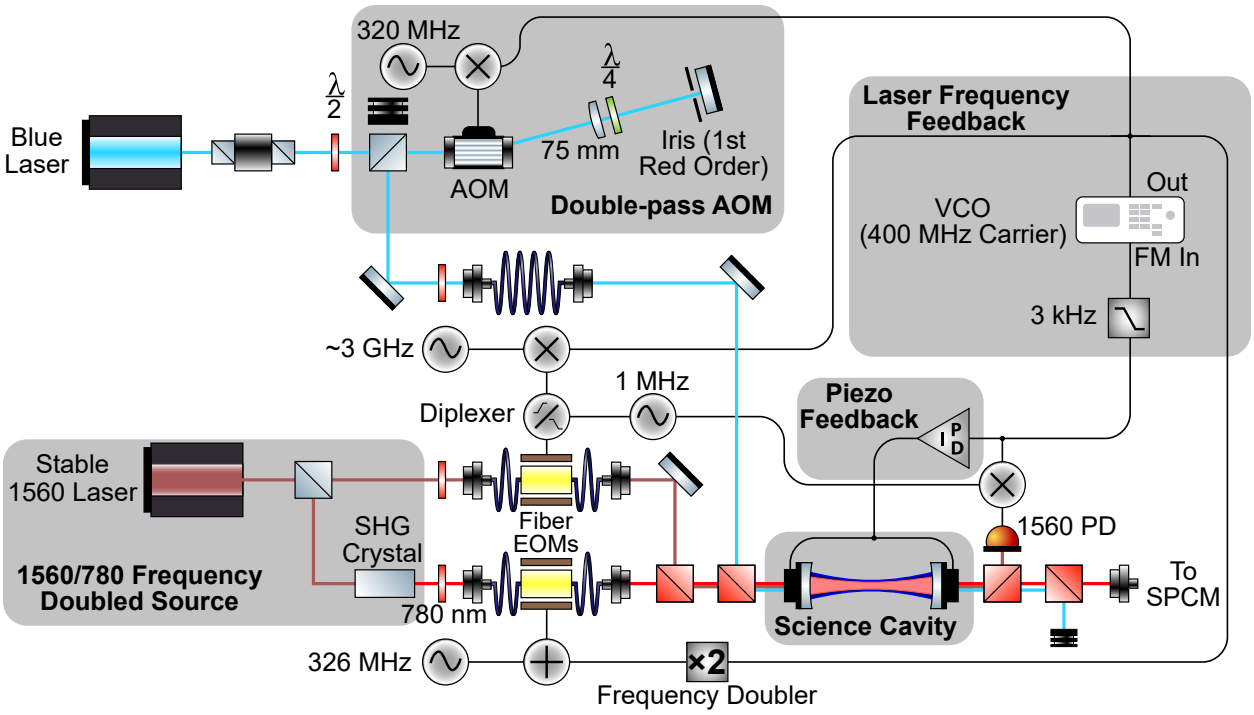

Figure 3.17: **Locking scheme for science cavity with frequency following.**

cannot be locked with 780 nm light, as this would interfere with the atoms. Instead, the cavity is first manually tuned to be resonant with the 780 nm sideband. A second modulator (EOM2) generates a sideband on the 1560 laser. This sideband is scanned until it is resonant with *any* cavity feature; then, locking the feature to this sideband stabilizes the cavity, while maintaining resonance with the 780 nm sideband. The blue laser is then tuned to two-photon resonance.

A unique feature of our locking scheme is the ability for the lasers to follow fast changes of the cavity length caused by pulse tube vibrations. Because the D_2 transition is quite broad, it is permissible for the 780 nm laser to change its frequency to follow the narrower cavity, so long as the 480 nm adjusts in the opposite direction to maintain two-photon resonance. Laser following is accomplished by feeding the cavity error signal to a voltage-controlled oscillator. The output of the VCO controls the 1560 sideband frequency at EOM2, closing the loop. Note that this lock is in parallel to the piezo lock of the cavity; it is preferable for the piezo

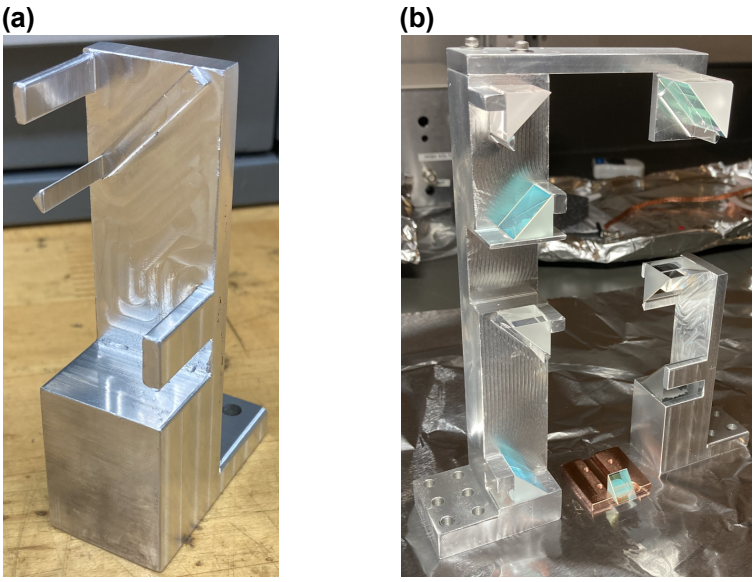

Figure 3.18: **Cryogenic optics mounts.** Custom cryogenic optics mounts have three lines and one plane of contact with right-angle prism mirrors, which are glued in place.

to stabilize the cavity length, but for high-frequency noise above the piezo bandwidth, laser following is useful.

The same VCO output is split and fed to both the 780 laser and the 480 laser. For the former it is doubled and fed to the EOM1 sideband, and for the latter it controls the frequency of a double-pass acousto-optic modulator. Now, because all three lasers move with the same VCO frequency, they will all follow the cavity shaking.

3.5.2 Cryogenic Optics

Custom optics were required due to limited optical access and the large amount of optical paths in the chamber: MOT cooling light and imaging, lattice guide mirrors, and optical cavity probes. Additionally, traditional methods of mounting optics can loosen at cryogenic temperatures, or tighten and induce stress. CNC-machined cryogenic beam elevators are shown in Figure 3.18. The mounts mounts have three lines and one plane of contact with right-angle prism mirrors, which are glued in place. This constrains all relevant degrees of freedom of the mirror, minimizing reliance on cryogenic epoxy, while maintaining a minimal

footprint to maintain room for the MOT beam. We have found that this highly constrained mirror design has held up to multiple cooldowns better than mounts where epoxy is the primary constraint.

3.6 Hybrid Cavity QED

With cold rubidium atoms transported into the hybrid cavity, we are able to characterize the light-matter coupling by probing the optical cavity in transmission. Each experiment begins by optically pumping the cavity with the narrow probe laser, tuned to the $|F = 3\rangle \rightarrow |F' = 3\rangle$ transition. Although the cavity is resonant with the $|F = 3\rangle \rightarrow |F' = 4\rangle$ cycling transition, sufficient light can be injected off resonance using a high probe power. An additional repumper beam tuned to $|F = 2\rangle \rightarrow |F' = 3\rangle$ is incident along the lattice path.

After pumping, the probe laser is swept over a range of 30 to 60 MHz around the atomic resonance in 1 ms, and the transmitted light is collected in an Excelitas single-photon counter module (SPCM). During this time some atoms are depumped, or the atoms that were initially pumped by the cavity mode drift away. Therefore we optically pump again, and probe again. The same sample of atoms can be probed 50 times in this manner before significant atom loss.

3.6.1 Electromagnetically-induced transparency

We begin by probing the atom-cavity system when it is far detuned from mm-wave resonance. The resulting transmission spectra, shown in Figure 3.19, are characteristic of vacuum Rabi splitting, or cavity electromagnetically induced transparency when the control laser is on. For all plots, black lines are fits to non-Hermitian perturbation theory from Chapter 2, where the cavity and atomic $5P$ linewidths are independentally calibrated.

In this data, taken before freezing the optimal field into the superconductor, the fitted γ_r is approximately 500 kHz, far above the natural linewidth of the Rydberg state. We

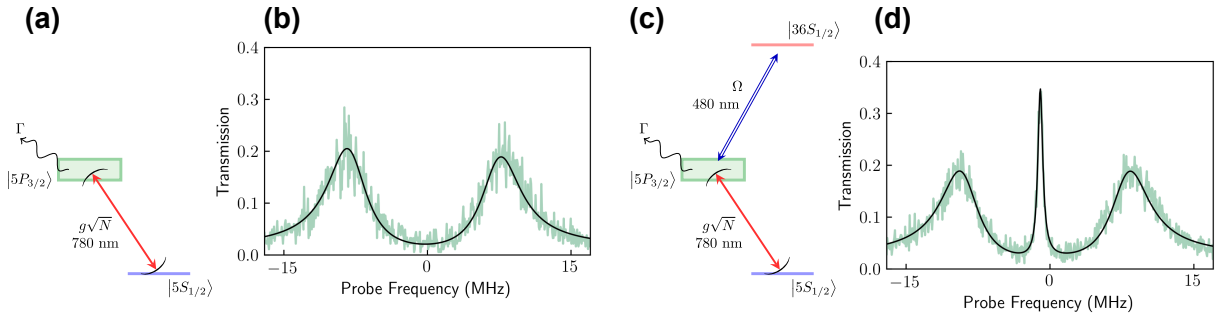

Figure 3.19: **Vacuum Rabi splitting and EIT transmission spectra in hybrid cavity.** **(a,b)** Level diagram and measured transmission spectrum for vacuum Rabi splitting induced by an atomic ensemble in a cavity. Black line is a fit to non-Hermitian perturbation theory. **(c,d)** Adding a classical control beam produces Rydberg EIT, evidenced by the narrow peak on two-photon resonance.

attribute this to imperfect optical pumping, so that the atoms are no longer an ideal 3-level system, causing decoherence of the collective state. This sort of decoherence mechanism is captured by the fitting function, but it is indistinguishable from actual decay of the Rydberg state.

After optimization of the magnetic field and optical pumping, the EIT spectrum improves dramatically, as shown in Figure 3.20. Better optical pumping allows all atoms to be in the stretched state with the highest Clebsch-Gordan coefficient for σ^+ probe light, improving the g (additionally, more atoms were loaded in the sample). Moreover, the fitted γ_r is 82 kHz, a dramatic improvement due to better coherence of the collective state. The remaining difference from the natural Rydberg linewidth is likely due to a combination of Doppler broadening and stray electric fields. This is currently being investigated.

3.6.2 Autler-Townes Splitting

We first observe coupling between a Rydberg polariton and the mm-wave field by driving a coherent tone at the Rydberg-Rydberg transition frequency, causing Autler Townes splitting in Figure 3.21. A clear avoided crossing is observed as the mm-wave tone frequency is swept over resonance in part (a). Subfigure (b) shows a single transmission trace taken near

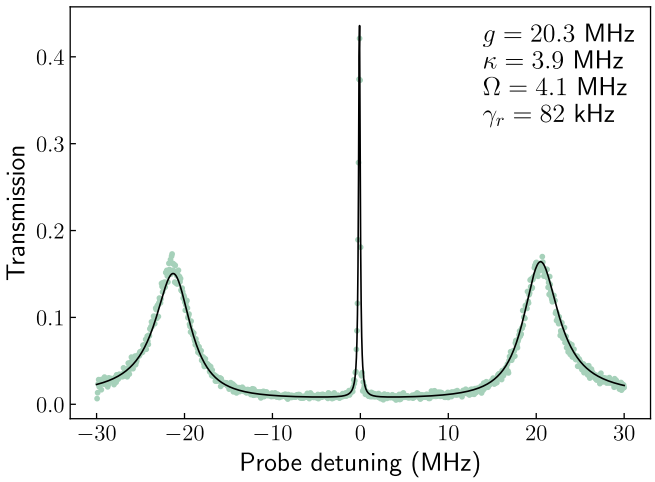

Figure 3.20: **EIT transmission spectrum with improved magnetic field control in superconductor.** Freezing in the correct field allows better control of polarizations and optical pumping, and correspondingly better coherence of the Rydberg polariton. Black line is non-Hermitian perturbation theory fit, where κ is indepdently calibrated. The rates in the inset are in units of natural frequency.

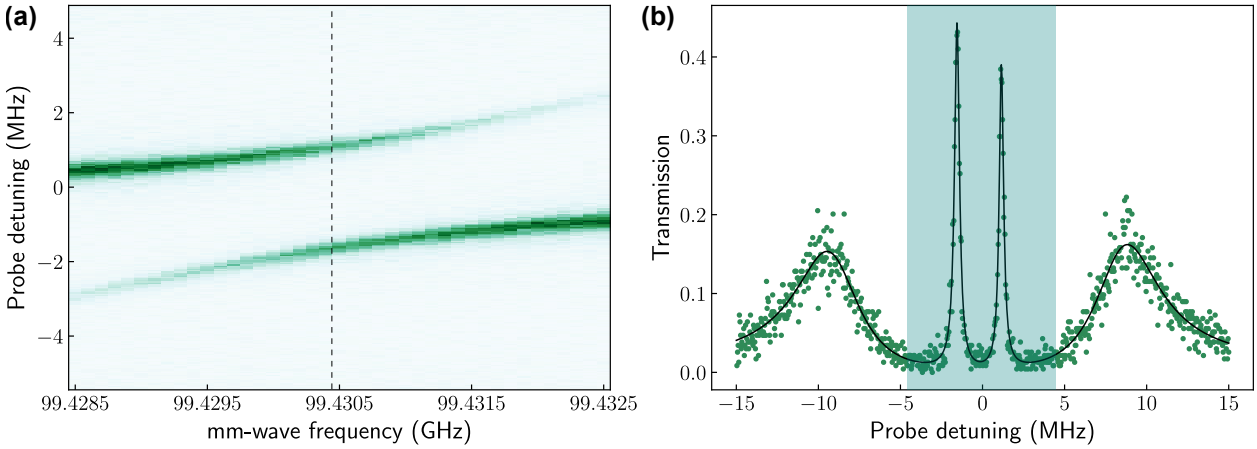

Figure 3.21: **Autler-Townes splitting in Rydberg manifold from mm-wave drive, (a)** Scanning a coherent mm-wave drive across the $|36S\rangle \leftrightarrow |35P\rangle$ Rydberg transition displays characteristic hybridization and AC Stark shit. **(b)** A single transmission spectrum with near-resonant mm-wave drive shows split EIT peak between bright polaritons.

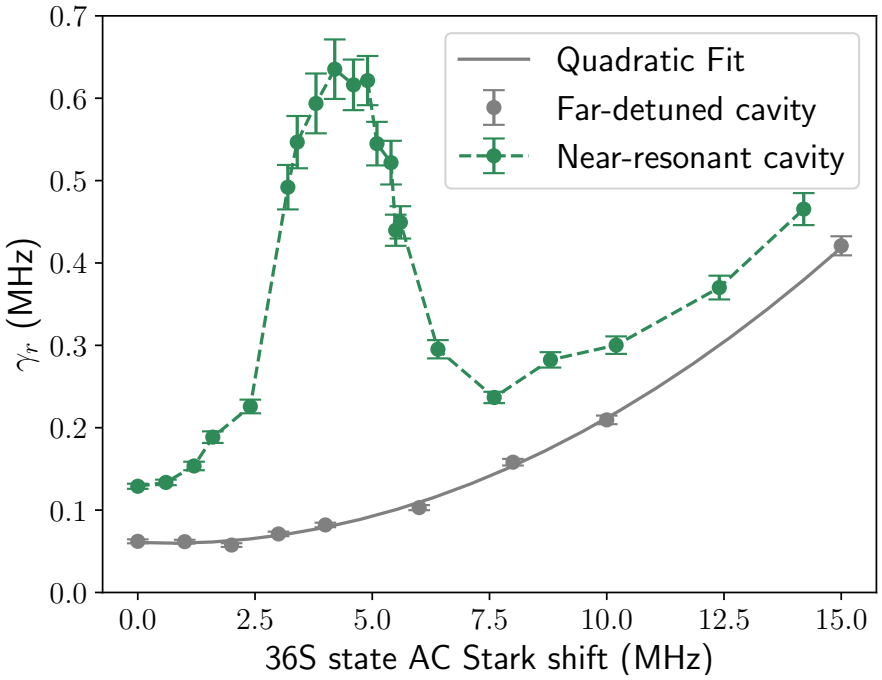

Figure 3.22: **Tuning of Rydberg transition into resonance with mm-wave cavity** Scanning a coherent mm-wave drive across the $|36S\rangle \leftrightarrow |35P\rangle$ Rydberg transition displays characteristic hybridization and AC Stark shit. **(b)** A single transmission spectrum with near-resonant mm-wave drive shows split EIT peak between bright polaritons.

resonance, where the split EIT peak lies between the two bright polaritons.

In this case, the mm-wave cavity is not resonant with the atomic transition, and the tuning tone is injected far from cavity resonance. Therefore this equivalent to a free-space coherent drive, and is not evidence of strong coupling to the cavity.

3.6.3 mm-wave Tuning and Hybrid Coupling Signature

Finally, we can use the Stark tuning scheme described in Section 3.3.2 to shift the atoms into resonance with the mm-wave cavity. Figure 3.22 shows fitted γ_r as a function of the atomic shift for two cavities. For each data point, the atomic levels are shifted with a coherent mm-wave tone at 101 GHz far from any atomic transition, and the frequency of the control beam is changed so that two-photon EIT resonance $\delta_{rc} = 0$ occurs at the same frequency as

atom-cavity resonance, $\delta_{ec} = 0$, producing the usual symmetric EIT spectrum.

The gray curve was taken using a mm-wave cavity that was far from atomic resonance, so no signature of atom-cavity coupling is expected. Nevertheless, we observe a quadratic increase of γ_r as the atom is progressively Stark shifted further. This effect is attributed to inhomogeneity of the mm-wave tuning mode across the atomic sample. Atoms closer to the mode center see a higher amplitude of the tuning field, while farther atoms are tuned less. This inhomogeneity leads direcly to decoherence of the collective state, displaying characteristic quadratic suppression of decoherence for dark state polaritons [70].

The green curve was taken using a mm-wave cavity a few MHz away from atomic resonance. When the atom is Stark tuned into cavity resonance, we see a clear signal in the increase of γ_r. This could be attributed to a near vacuum Rabi splitting of the EIT peak, but with a coupling too small to be resolved. In fact, the cavity is not in a vacuum state: at 5 K, we expect a mean thermal occupation $\overline{n} = 0.6$ photons. Nevertheless, this is clear evidence of coupling between a cavity Rydberg polariton and a mm-wave cavity with sub-photon occupation!

CHAPTER 4

VIBRATIONS AND MECHANICAL DESIGN

Optical cavities are a useful and versatile option to enhance the light-matter interaction in quantum systems. The effective optical depth (or cooperativity) of an atomic sample is enhanced by a factor of the cavity finesse $\mathcal{F}$, which can reach values of hundreds of thousands for state of the art dielectric mirrors. This provides an attractive option to reach the high cooperativity regime, as other methods to enhance the optical depth, such as increasing atomic density and tighter focusing of the beam, are limited with current technologies.

The linewidth of an optical cavity scales inversely with the finesse, so that the relative frequencies of the laser and cavity resonance peak must be controlled to a high precision. Stabilizing the cavity resonance to within a linewidth requires the length be stable to $\Delta L < \frac{\lambda}{2\mathcal{F}}$, where λ is the wavelength of light. Even for the relatively modest finesses $\mathcal{F} \sim 2000$ used here, this requires $\Delta L \sim 2$ Å for 780 nm light. This is by far the most stringent positional stability requirement in most experiments. Nevertheless, optical cavities are extremely common in AMO experiments, and it is somewhat remarkable that such stability is relatively easily achieved by attaching mirrors to a rigid structure (and sometimes locking with a piezoelectric actuator, which often only has low bandwidth to correct for slow drifts), and minimizing noise in the lab.

Unlike most atomic physics experiments, this experiment resides in a helium cryostat to suppress thermal mm-wave populations and enable the use of superconducting materials. Cryogenic systems generally add vibrational noise, significantly complicating the task of stabilizing an optical cavity. While wet cryostats introduce relatively modest vibrations from boiling cryogenic liquids [85], they must be refilled periodically, which is disruptive and expensive. Closed cycle cryogenic systems operate continuously with no need for refilling. However, closed cycle cryostats produce large vibrations with amplitudes around 10-20 μm due to high-pressure helium flow through the cold head [86], which occur about once per

second and have significant high-frequency components due to the impulse-like nature of the helium flow. As we will see, the vibrations of the cryostat are not the only difficulty – material property changes at low temperatures pose additional difficulties for stabilizing optical cavities.

In this chapter, I will first review methods of cryogenic vibration isolation that have been used successfully, and describe the particular challenges of our hybrid atomic system which must be addressed. I will then describe the performance of the custom low-vibration cryostat built for this experiment. Despite this vibration suppression, early optical cavities used in the system suffered from huge mechanical resonances which made them impossible to stabilize. I will show how a circuit model of mechanics helped to understand these issues, and to design a new generation of spring-stabilized cavities which provide stability at the 25 pm-rms level, sufficient for the experiments here. Finally, several options for further vibration suppression will be discussed, which could be useful if higher-finesse cavities are required.

4.1 Overview of Cryogenic Vibration Suppression

Cryogenic operation is necessary in a wide variety of experiments, many of which are also highly sensitive to acoustic noise. Cryogenic vibration suppression has received particular attention in scanning probe microscopy (SPM) experiments [85, 87, 88, 89], where the tip-sample distance must be stabilized to 10 or even 1 pm within a bandwidth of a few kHz [90].

Meanwhile, cryogenic optical resonators with finesses in the 10^5 range are used as stable frequency references in optical clock experiments, where vibrations can become a domninant source of instability at low integration times [91].

The past few years have seen growing interest in cryogenic solid-state quantum emitters inside optical fiber-based microcavities [92], which often require an in-situ 2D positioning system to scan through embedded emitters. In liquid-helium cryostats, fiber-based cavities

have been stabilized [93, 94] to a level of $4pm$ [95], and macroscopic optical cavities have also been successfully locked [19]. In closed-cycle cryostats, open microcavities have attained stability in the range of 30-100 pm rms [96, 97, 98, 99], or better in the quiet periods of the cryocooler cycle. One group has stabilized a finesse $120,000$ fiber cavity to less than 1 pm [100] using a combination of room-temperature vibration isolation with gas exchange cooling, and thermooptic feedback [101].

All of these systems, especially those in closed-cycle cryostats, employ various methods of vibration isolation to achieve the necessary mechanical stability. Many of these techniques fall into a few broad categories, which are reviewed here, both to understand the present experiment, and as a reference for future improvements if higher stability is required. The most important section for the present experiment is Section 4.1.4.

4.1.1 Mechanical Decoupling

The best possible method to isolate a sensitive experiment from the vibrations of a closed-cycle cryostat would be to leave them mechanically unconnected. Unfortunately, this is not possible. Vacuum integrity requires a continuous connection of the room temperature stage, while transmission of cooling power requires some sort of contact for heat transfer.

The next best thing is to rigidly fix the cryostat and experiment in place separately, and connect them with links which are as soft as possible. This is part of the design philosophy of nearly every optical cryostat, ours included. Vacuum connections are usually performed with flexible bellows, while heat transfer often occurs through flexible copper braids [102]. In reference [103], the cryocooler vacuum chamber is rigidly mounted on an aluminum pillar, while the cavity vacuum chamber is rigidly mounted on a separate optical table via a vibration isolation table. The only mechanical connections are the vacuum bellows and flexible thermal links. A very thorough design for mechanical decoupling via a long cold arm is presented by Micke et al [76].

As an alternative to flexible copper links, heat can be transfered through helium exchange gas [95, 100, 88, 89], which has much less vibration transmission, at the expense of design complication and some cooling power.

In addition to propagation through the vacuum chamber and thermal links, vibrations can propagate through the air and floor. These vibrations outside the vacuum assembly can be further attenuated. The motor and helium compressor can be placed far from the science chamber and cold head, even in a separate room [76], and the helium hoses can be guided through heavy sand-filled containers to damp vibrations [104]. The room-temperature components (pumps, compressor, cryostat chamber) can all be supported on separate vibration isolation platforms to isolate from floor vibrations [90, 87], while acoustic shielding can reduce ambient acoustic excitation. These measures also protect against ambient noise unrelated to to the cryostat.

4.1.2 Low-Pass Mechanical Filtering

A second option for vibration isolation is to build a platform which only passes low frequency vibrations, upon which the payload is mounted. The platform of mass M is supported by a spring with spring constant k; together they form a simple harmonic oscillator whose amplitude response falls off above the resonance frequency. The platform is isolated both from forces applied directly to the platform, and to vibrations of its support point (which appear as a force of $F = k\Delta x_{\text{support}}$). The platform can be suspended (common in SPM designs [105, 88, 89, 85]), or supported from below (common in microcavity designs [99, 96]).

The harmonic oscillator transmission $\frac{x}{F}$ falls off above resonance as $1/\omega^2$. Thus the displacement attenuation at high frequencies can be increased by a factor of 100 each time the filter resonance frequency is decreased by a factor of 10. This strategy has a limit: the resonance frequency of a mass supported vertically on a spring can be written $\omega_0 = \sqrt{\frac{g}{\Delta L}}$ where ΔL is the spring extension (or compression) length, so decreasing the resonance

frequency requires more space. One solution is to use a relatively stiff spring to support the mass with minimal compression, then place negative spring constant elements in parallel with the stiff spring, decreasing the effective spring constant k. An example of a negative k element is a beam on the edge of buckling, which tends to bow outward in the direction it is displaced. A more common strategy in cryogenic vibration isolation is to place multiple mass-spring systems in series; their high-frequency attenuations multiply, while the spring extension increases more slowly [106].

If the only connection between stages is through compliant springs, there is a tradeoff between high thermal conductance (scaling with cross-sectional area) and high spring compliance (scaling inversely with cross-sectional area). Additional thermalization elements like soft copper braids can be placed in parallel with the springs, so long as they are much softer than the springs, so that the total compliance is not compromised [105].

One potentially useful design for our system does not mount the cavity on a vibration isolation stage, but rather converts the cold arm between cryocooler chamber and science chamber into a low-pass filter by hanging it as a pendulum [76].

Mechanical low-pass designs generally rely on the properties of ideal masses and springs. However, at high frequencies, both masses and springs have internal resonances and may no longer act ideally. There are few measurements of high-frequency ($>$ kHz) vibration isolation, as high-frequency measurements are difficult, but it is very relevant to our system. A good primer on high-frequency vibration isolation can be found in reference [107]. One recent STM design has a high-corner frequency isolator before a low-corner isolator, so that the former can pre-filter high frequencies which might excite resonances of the latter [105].

4.1.3 Damping

An issue with resonant vibration isolation systems is that transmissibility increases near the resonance frequency. This may not be too problematic for optical cavity stabilization,

as rigid cavities are less susceptible to low-frequency vibration, and their lengths can be actively stabilized at low frequencies (see Subsection 4.1.4). Still, the stage resonances can be decreased with damping[1].

Damping is difficult in cryogenic environments due to altered material properties, ruling out common room-temperature designs like layered masses on elastomer rings [108]. The best solution is magnetic eddy current damping [109], where the relative motion of a conductor and magnets dissipates energy as eddy currents.

Damping also degrades high-frequency roll-off. A one-axis damped vibration isolator, with harmonic excitation at its support point with amplitude x_s, has equation of motion

$$\frac{d^2x}{dt^2} + 2\xi\omega_0\frac{d}{dt}\left(x - x_s e^{i\omega t}\right) + \omega_0^2(x - x_s e^{i\omega t}) = 0 \tag{4.1}$$

The magnitude of the response is

$$\left|\frac{x}{x_s}\right| = \sqrt{\frac{1 + (2\xi\omega/\omega_0)^2}{\left(1 - \omega^2/\omega_0^2\right)^2 + (2\xi\omega/\omega_0)^2}} \tag{4.2}$$

At $\omega \gg \frac{\omega_0}{\xi}$, the rolloff degrades from $1/\omega^2$ to $1/\omega$.

This problem only occurs when the motion of the platform is damped with respect to the source of vibrations. In this case the term $2\xi\omega_0\frac{d}{dt}x_s$ acts as a coupling whose magnitude increases with frequency. In principle, if the damping were instead relative to a fixed reference, e.g. by attaching the magnets to a very stable part of the room-temperature frame, this term goes away. Another option is a tuned mass damper, which has been implemented for a cryogenic optical cavity [99]. In this case an auxiliary mass is suspended via a spring from the main platform, and the relative motion between those two masses is damped, so that there is no dissipative coupling to the vibration source. The auxiliary mass and spring

1. Another option to reduce stage resonances is active feedback on the vibration isolation stage itself

are chosen to have a resonance frequency near ω_0, maximizing relative motion between the two at the problematic resonance frequency so that dissipation is maximized.

4.1.4 High-Pass Mechanical Filtering

An optical cavity is stable when the separation between its mirrors is constant. A rigid mechanical structure joining the mirrors acts as a high-pass filter for the mirror separation, converting vibrational noise to common-mode displacement which does not alter the length. The high-pass cut-off frequency is set by the structure's mechanical resonance frequencies. In fact, far below resonance frequencies, acceleration of the cavity support $\ddot{x}_s$ is equivalent to a gravity-like force on the cavity [110] $F(\boldsymbol{r}) = \rho(\boldsymbol{r})\ddot{x}_s = -\omega^2\rho(\boldsymbol{r})x_s$, which can easily be simulated in finite-element packages. This is a second order high-pass. The deflection is a function of this effective force (and thus density) and the cavity rigidity. Cavity length changes are further suppressed with highly symmetric spacer and mounting design, ensuring both mirrors are displaced identically.

Extremely stable cryogenic resonators have been constructed from rigid sapphire [91] or single-crystal silicon spacers [103, 111] with optically contacted mirrors and high symmetry.

Thus, high resonance frequencies perform three functions. Passive stability at low frequencies is increased due to the high-pass effect. Active stabilization bandwidth is increased as problematic resonance phase shifts are pushed higher. Finally, environmental noise couples strongly into resonances but tends to fall off at sufficiently high frequencies, so it is best to have resonances above significant noise.

It is this last factor that proves dominant for our current cavities.

As a final note, a combination of the mechanical low-pass and high-pass techniques could effectively cancel noise at all frequencies.

4.1.5 Requirements for Hybrid Atomic System

The techniques described in this section have been proven to reduce pulse tube vibrations to a level sufficient for locking a high-finesse optical cavity. However, there are various engineering tradeoffs for these solutions, some of which are at odds with the unique goals of our system.

In particular, low-pass vibration isolation stages require soft thermal interlinks between each stage, imposing significant thermal impedances and limiting cooling power and temperature at the payload. Even with very careful thermal design, in dilution fridge systems the cooling power is generally decreased by a factor of 7 or more [102, 112, 113], while vibration isolation stages on 4 K cryostats have demonstrated payload temperatures from 7 to 11 K [99, 97].

Likely with further engineering, these problems could be solved. However, our hybrid system is extremely sensitive to temperature, as the superconducting mm-wave cavity quality factor rises exponentially with lower temperatures. Furthermore, in the current design, the mm-wave circuitry is rigidly connected to the cavity. Thus this would also need to be isolated, adding to the size of the isolator, and putting great demands on cooling power due to the active mm-wave amplifier. Finally, our system already has many components due to being a hybrid system, and adding additional complication inevitably interferes with other subsystems. For these reasons, it is preferable to use a simple solution with high thermal conductance.

The goal of our system is to rigidly connect the cavity to the science chamber cold plate, maximizing cooling power, while ensuring that all cavity mechanical resonances are far above the noise frequencies. The cavity must also be stiff enough that low frequency noise is heavily suppressed. Several factors work in our favor. Our custom cryostat design already suppresses vibrations substantially. Furthermore, the optical cavity is only moderate high finesse, and can be rigidly constructed (compared to open cavity structures), thus

requiring correspondingly moderate vibration isolation. On the other hand, our cavity must be relatively long (> 1 cm), as the mm-wave quality factor is limited by the length of holes drilled for optical access. This decreases cavity rigidity. Also, this requires macroscopic mirrors to accomodate larger radii of curvature and mode sizes, adding mass to the system (compared to fiber mirrors). As will be seen later, this added mass causes problematic mechanical resonances, though they can be fixed with proper mechanical design.

4.2 Custom Low-Vibration Cryostat

Our experiment has a home-built cryostat designed to minimize transmission of vibrations from the cold head to the experiment. The system is based on a Cryomech PT410 pulse tube cryocooler with CPA298C compressor. This is a closed cycle cryocooler with two stages, providing 1 W of cooling power at 4.2 K and 40 W at 45 K, with a base temperature rated at 2.8 K. As the cooling performance was discussed in Chapter 3, we focus here on the low-vibration design.

The philosophy of the design is to mechanically decouple the experiment into two independently supported subsystems . The cold head subsystem contains the cold head and pumps, while the experiment subsystem contains the vacuum structure and all experimental components. The exterior is shown in Figure 4.2, where experiment components are colored green, cold head components blue, and flexible linkages between them orange.

The cold head subsystem consists of two plates supported by a t-slotted framing system, which is hung from structural elements in the ceiling. The cold head attaches directly to the upper plate. The lower plate has vacuum connectors to attach a turbomolecular pump. The frame extends from above down through a hole in an optical table, which allows the lower plate to sit below the table surface. This hole also facilitates access to the pulse tube from below, when the lower plate is removed.

The experiment subsytem is supported by the optical table, and consists of two vacuum

Figure 4.1: **Custom two-chamber cryostat with vibration-decoupling design.** Blue and green subsystems are independently supported, linked by flexible bellows (orange).

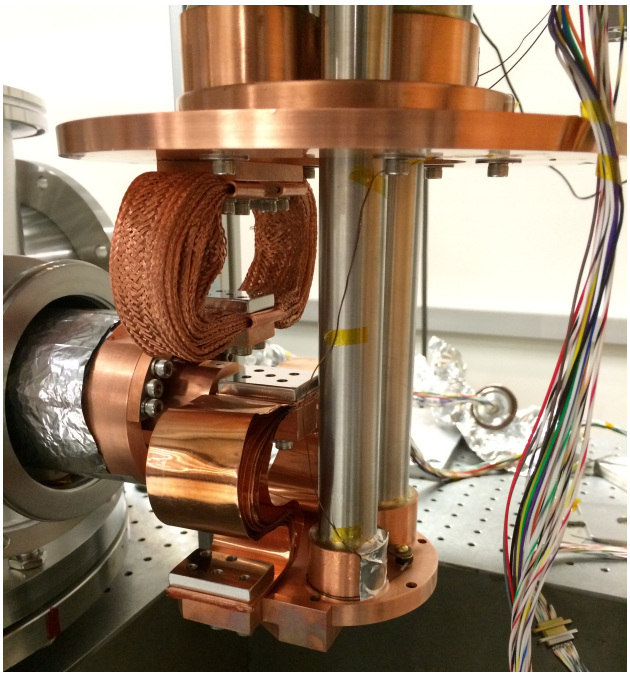

Figure 4.2: **Flexible thermal connection.** Fridge chamber interior with flexible braids connecting cold head to the cold arms.

chambers, rigidly connected together. The science chamber rests directly on the table, while the fridge chamber has 3 protrusions above the optical table. The space between the protrusions and the table is filled by shims, and then it is clamped together. The fridge chamber rests around the cold head. From the fridge chamber, one flexible vacuum bellows extends up to the top plate, while another extends down to the bottom plate, completing the vacuum exterior.

The pulse tube comes with the remote motor option, so that the motor rests far from the cold head and is connected to it by flexible helium lines. The helium compressor sits in a separate room, and is connected to the motor by similar lines.

Inside the vacuum chamber, the science chamber contains two copper plates meant to be thermalized to 35 K and 4 K. Two copper cold arms transfer cooling power from the cold head plates to the science chamber plates. The 35 K cold arm is a hollow tube, so that it can surround the 4 K arm to protect it from room temperature radiation.

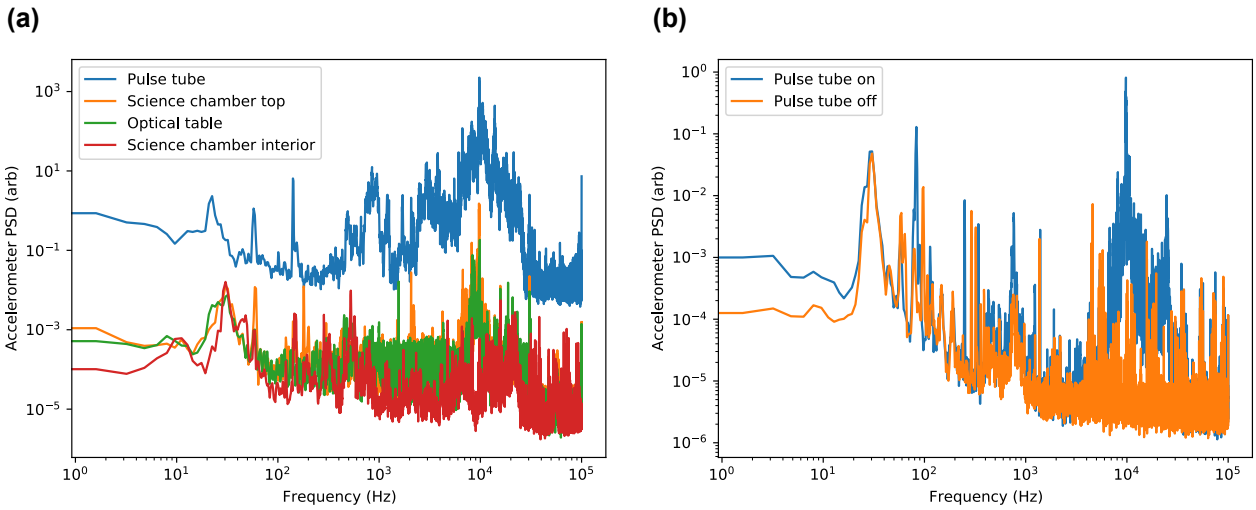

Figure 4.3: **Accelerometer measurement of vibration isolation.** **(a)** Pulse tube on in various locations. **(b)** Effect of pulse tube on science chamber top.

Both cold arms are attached to the cold head via flexible copper braids to minimize vibration transmission. In the initial design, the cold arms were also to be attached to the science chamber plates with flexible braids. Then the cold arms would be suspended by strings from the vaccum chamber walls, allowing them a pendulum degree of motion similar to a recent design [76]. Instead, to maximize cooling power, the cold arms are rigidly attached to the science chamber plates, so they are mechanically supported in a cantilever fashion and do not need to be suspended.

4.2.1 Accelerometer Measurement

The vibrational performance of the cryostat is ultimately measured by the spectrum of positional displacement at the payload. First, a convenient way to coarsely check the vibration suppression is to use a MEMS accelerometer. In Figure 4.3, we plot the power spectral density of the output voltage of an accelerometer, measuring along the vertical direction. These measurements are all taken at room temperature. In Figure 4.3a, the pulse tube is on, and the accelerometer is placed directly on the cold head (blue), on the science chamber top (orange), on the optical table (green), or on the 35K plate of the science chamber interior

(red). In Figure 4.3b, the accelerometer is placed on the science chamber top with the pulse tube on (blue) or off (orange).

The accelerometer is not rated for high frequencies, so the absolute calibration at any given frequency is unreliable. However, to the extent that it is linear, we can compare readings in two conditions to determine the relative suppresssion. Compared to the cold head, measurements at the other locations are uniformly lower by 3 to 4 orders of magnitude. There are also two qualitative features worth pointing out: first, the pulse tube adds significant broadband noise around 3 kHz, 10 kHz, and 20 kHz compared to ambient. Second, there is strong ambient noise at 30 Hz and 60 Hz even without the pulse tube. This is not 60 Hz electrical noise; we attribute it to a pendulum-like resonant mode of the whole vacuum chamber or optical table.

4.2.2 Interferometer Measurement

An optical interferometer can be used to measure vibrations at cryogenic temperatures, and with much greater precision. A self-heterodyne interferometer was constructed with a reference arm on the optical table, and the signal arm formed by a retroreflection mirror on the science chamber 35K plate. The mirror was oriented to measure displacements along the axis parallel to the cold arms. As the displacement was greater than a full fringe, the interferometer had to be locked. The interference of the two arms was measured on a photodiode outside the chamber, resulting in a signal

$$M \propto \sin\Delta\phi \approx \frac{2\pi f}{\nu} + \frac{2\pi\Delta L}{\lambda/2} \tag{4.3}$$

where $\Delta\phi$ is the phase difference between the arms, f is the laser frequency, $\nu = \frac{c}{2\left(L_{\text{signal}} - L_{\text{ref}}\right)}$ is the free spectral range of the interferometer, and ΔL is the displacement of the mirror. This signal was fed through a PI loop filter and into the laser controller's current modulation

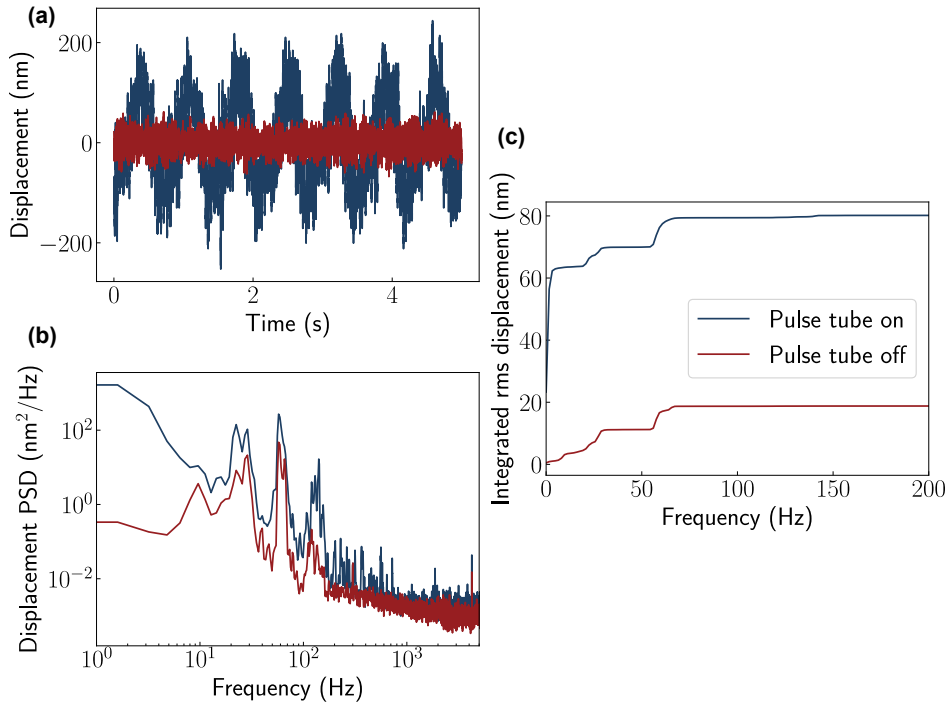

Figure 4.4: **Interferometer measurement on science chamber 35K vibrations. (a)** Absolute displacement, **(b)** Power spectral density of displacement, **(c)** Integrated RMS Displacement.

port, which modulates the laser frequency, to lock the relative phase of the two arms. The voltage sent to the laser then equals

$$V = \frac{1}{G}\frac{L}{1+L}\left(\frac{\nu\Delta L}{\lambda/2}\right) \tag{4.4}$$

where G is the laser transfer function from input voltage to frequency and L is the loop gain. For a tight lock ($L \gg 1$), this is $V = \frac{1}{G}\left(\frac{\nu\Delta L}{\lambda/2}\right)$. Calibrating the laser transfer function and interferometer free spectral range yields the displacement. The control loop had a unity gain bandwidth of 10 kHz, but no signal was visible above the noise floor past 2 kHz anyway.

The vibrational amplitude on the science chamber 35 K stage is 400 nm peak-to-peak, and around 80 nm rms. The majority of this occurs at the frequency of the pulse tube (around 1 Hz) and its first few harmonics. Again we see substantial motion at 30 Hz and 60 Hz, attributable to a vibrational mode of the whole chamber and optical table. Above 100 Hz, the vibrational noise is too small to be detected with the sensitivity of this instrument. Nevertheless, high-frequency vibration proved troublesome for early generations of optical cavities.

4.3 First Generation Optical Cavities

I now discuss the construction of our cryogenic optical cavities, starting with the first generation of highly vibration-prone designs. The requirements for our optical cavities are fairly simple. Two mirrors must be held rigidly apart by a spacer, and at least one mirror must be mounted on a piezoelectric actuator for length tunability. The spacer is made from a block of pure niobium, as it also functions as a superconducting mm-wave resonator. In our earliest cavities, these components were bonded with cryogenic epoxy. Because these resonators are fairly short and constructed from a single block of metal, we would expect them to be quite robust to vibrational noise. Indeed, this was the case at room temperature –

the pulse tube barely affected the cavities. However, once cooled to cryogenic temperatures, the cavity transmission peaks would shake by up to tens of linewidths, amounting to several nanometers of relative shaking between the mirrors. Here these early cavity designs will be described, and their poor performance explained.

4.3.1 Optical Cavity Components

Several features are common to the construction of all cavities presented here. The mirrors are 7.75 mm diameter round, UV fused silica substrates with 25 mm radius of curvature and 4 mm thickness. The spacers are bulk niobium, with varying lengths near 2 cm, and varying cross sections about 2 cm $\times$ 2 cm. The exact dimensions of the spacers are different for each cavity and haven't been seen to affect vibrational performance much (other factors are limiting), so the point won't be belabored.

We interchangeably used two piezoelectric actuators, both multilayer ring actuators: Thorlabs PA44LEW, and PI PD080.3x. The properties of these actuators are summarized in Table 4.1. For all cryogenic cavities, we mounted both mirrors on piezos and drove the two in parallel. At room temperature, the two piezos together were measured to have a range of 4-5 μm, or 10-13 free spectral ranges at 780 nm, with minor variations between piezos. At 4 Kelvin, the throw consistently decreased to approximatly 15% of the room temperature values. Forunately, this is still greater than a free spectral range at 780 nm. At cryogenic temperatures, piezos experience a large increase in the coercive field, making them extremely resistant to depoling. Therefore they can be driven with negative voltages, potentially doubling the range (though this was not necessary in our case).

The expected mass-on-spring resonance for the mirror and piezo, with one end fixed, is estimated from the mass of the mirror and the spring constant of the piezo. The mirror mass is $M = 0.50$ g for mirrors with the dimensions given above (and density of fused silica 2.63 g/cm^3). The spring constant of the piezo can be estimated as the ratio of the

Actuator	Thorlabs PA44LEW	PI PD080.3x	Unit
Outer diameter	8.3	8	mm
Inner diameter	3.0	4.5	mm
Height	2.0	2.5	mm
Travel range	2.6	2	μm
Blocking force	1800	> 1000	N
Capacitance	550	300	nF
Axial resonant frequency	515	> 500	kHz
Mass	0.72	~ 0.66	g

Table 4.1: Properties of the two piezos used for optical cavities.

blocking force to travel range, yielding $k = 7 \times 10^8$ N/m for the Thorlabs piezo. The axial resonance frequencies of the loaded piezo, fixed on one end, can be calculated by solving the one-dimensional wave equation in the piezo with appropriate boundary conditions, yielding a transcendental equation $0 = 1 - 2\pi f_r \frac{M}{\sqrt{k m_p}} \tan\left(2\pi f_r \sqrt{\frac{m_p}{k}}\right)$. For $M \gg m_p$ the first resonance frequency is approximately $f_r = \frac{1}{2\pi}\sqrt{\frac{k}{M+m_p/3}}$. For $M \ll m_p$ the first resonance frequency is approximately $f_r = \frac{\frac{1}{4}\sqrt{\frac{k}{m}}}{1+\frac{M}{m}}$. The exact resonance frequency is > 100 kHz. This is far above any frequencies of interest, so the piezo can be treated as an ideal spring supporting an effective mass $\frac{m}{3}$ according to a one-pole expansion of its mechanical transfer function [114].

4.3.2 Epoxy Cavity Construction

Early cavities were constructed by bonding mirrors and piezoelectric actuators to either side of the spacer with a cryogenic epoxy, largely following techniques from the Regal group at JILA [115]. Thin invar washers were also placed between spacer and piezo, and between piezo and mirror. The idea was that invar's low coefficient of thermal expansion would be better matched to that of the mirror and piezo, preventing cracking. However, we later stopped using the invar washers with little change in performance. We note that most cryogenic epoxies contract far more than the pieces being bonded anyway.

During construction, the piezo, mirror, and optional invar washers are held together by

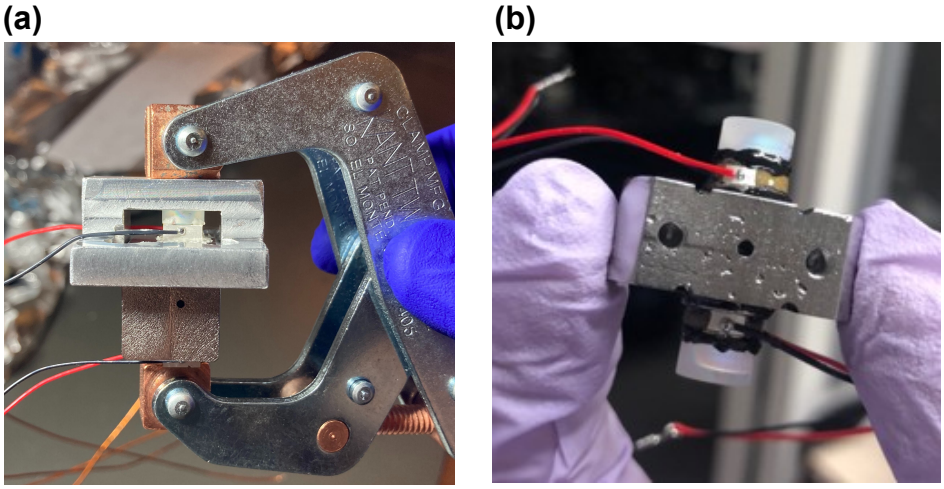

Figure 4.5: **Construction of epoxied cavities. (a)** Cavity in gluing jig (no invar design), **(b)** Finished cavity (invar design).

a clamp and a mounting jig, as shown in Figure 4.5(a). The mounting jig fits tightly around spacer and mirror to properly locate the mirror; sometimes a separate jig is used to center and glue the piezo first. Before the components are placed in the jig, they are all cleaned. The spacers are cleaned in an ultrasonic bath with the standard sequence of UHV-cleaning solvents. The piezos are wiped down with isopropyl alcohol using a lint-free cloth. If the mirrors have visible dust on their surfaces under a microscope, they are cleaned using First Contact polymer cleaning solution. For very persistent dust, one can fold a piece of lens tissue several times, grasp it in forceps, wet it with a couple drops of acetone, fold the tissue over the forceps so no metal is exposed, and firmly wipe it across the mirror surface. This is then repeated with methanol to remove residual solvent.

Once the stack of components is firmly clamped in the mounting jig, the epoxy is prepared. Early designs used Stycast 2850FT with Catalyst 9, a very common cryogenic epoxy. The resin and catalyst are mixed according to the recommended ratio for about 2 minutes. The mixing should be done as smoothly as possible to avoid introducing air bubbles. After mixing, the epoxy is placed in an o-ring sealed vacuum pot pumped by an oil-free scroll pump to degas it. The epoxy is left under vacuum for about 5 minutes, and a valve to atmosphere

is periodically cracked open so that the pressure does not go too far below 5 mbar. Apparently too low pressures can boil off some components of the epoxy, causing issues. I have not thoroughly verified that this degassing process has any effect on the ultimate performance of the epoxy bond, but it is said to be a good idea.

The epoxy is then painted in a full circle around each component in the stack using a toothpick or thin piece of music wire. Care should be taken to press the epoxy thoroughly into the corner between each component, as this part is responsible for much of the bond strength and stiffness. Also, the epoxy attaching the piezo to the spacer should not go too far up the side of the piezo, as this can bind the piezo and limit travel range. Once the epoxy is painted on, it is left to cure for the recommended cure schedule. A completed cavity with invar washers and Stycast 2850 FT is shown in Figure 4.5(b).

4.3.3 Epoxy Cavity Performance

After building a cavity as described above, we placed it in the vacuum chamber and cooled it down. At room temperature, even with the pulse tube on, it worked well. By the time it reached a temperature of 35 K, the cavity resonance peak was shaking around by tens of linewidths, making it impossible to lock. During subsequent cooldowns, the performance degraded further.

Various measures were tried to create a more stable cavity. Eventually one cavity shook around by only a few linewidths. The length excursions of this cavity were measured in a similar fashion to the interferometer in Equation 4.4. However, in this case the laser is locked to the cavity not by tuning the laser diode current, but by creating a sideband with an electro-optic modulator driven by a tunable voltage-controlled oscillator (Hewlett-Packard). Calibrating the output frequency of the VCO from its voltage input yields the cavity length change exactly as for the interferometer. In this case the resolvable signal is much better due to the high displacement sensitivity of the cavity, and because the unity gain bandwidth

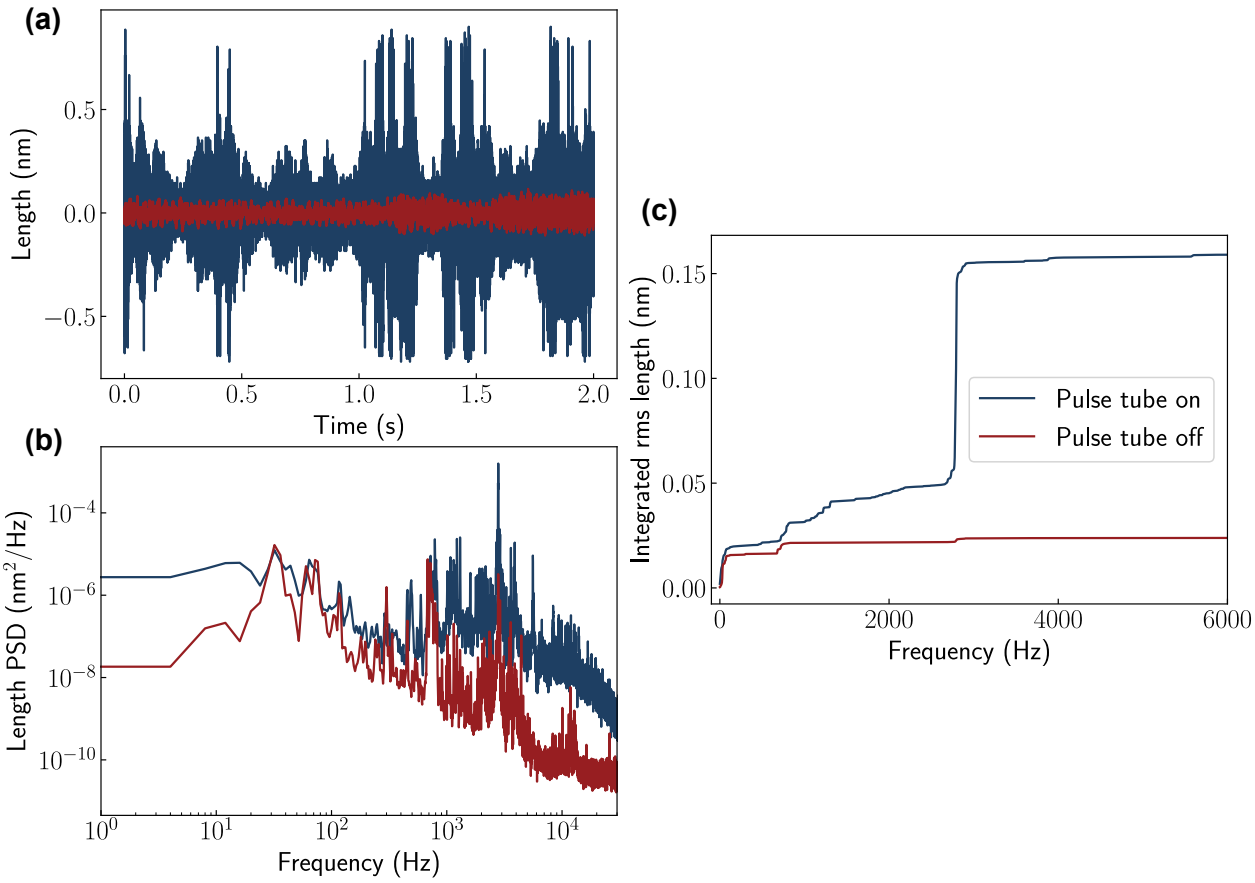

Figure 4.6: **Length shaking of epoxy cavity.** **(a)** Absolute displacement, **(b)** Power spectral density of displacement, **(c)** Integrated RMS Displacement.

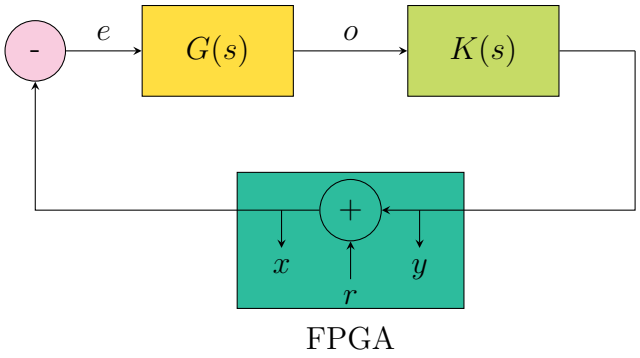

Figure 4.7: Block diagram for transfer function measurement.

of the lock is now 100 kHz.

The cavity length shaking is shown in Figure 4.6. The absolute length in Figure 4.6(a) shows peak-to-peak excursions of $\pm 0.6nm$, amounting to ± 6 linewidths for a finesse 4000 cavity, while the rms in Figure 4.6(c) is 0.15 nm. Most importantly, almost all of the shaking occurs at a frequency near 3 kHz.

This is suggestive of a resonance in the system. I measured the transfer function of the piezo to determine the properties of this resonance. The transfer function is measured in lock according to the scheme in Figure 4.7, where K represents the PI loop filter, G is the piezo driver and piezo mechanical response, and the loop gain is defined as $L \equiv KG$. The error signal is passed through a RedPitaya FPGA which injects a sinusoidal signal and measures the error signal before and after injection. Then the ratio $\frac{x}{y} = L$.

The transfer function, shown in Figure 4.8, indeed shows a very large resonance around 3 kHz. Similar resonances have been seen in cryogenic Fabry-Perot cavities before [115], but that experiment was in a wet fridge and so the resonance was not excite by pulse tube noise.

In addition to the main resonance, there are many smaller resonances that occur as pole-zero pairs, most prominently at 3.5 kHz. The large resonance, however, enters as a single pole; this is confirmed by the fact that the roll-off of the transfer function increases above 3 kHz. This form of the transfer function is enough to exactly identify the source of the large resonance. To understand this, we will take a brief diversion to discuss mechanical network

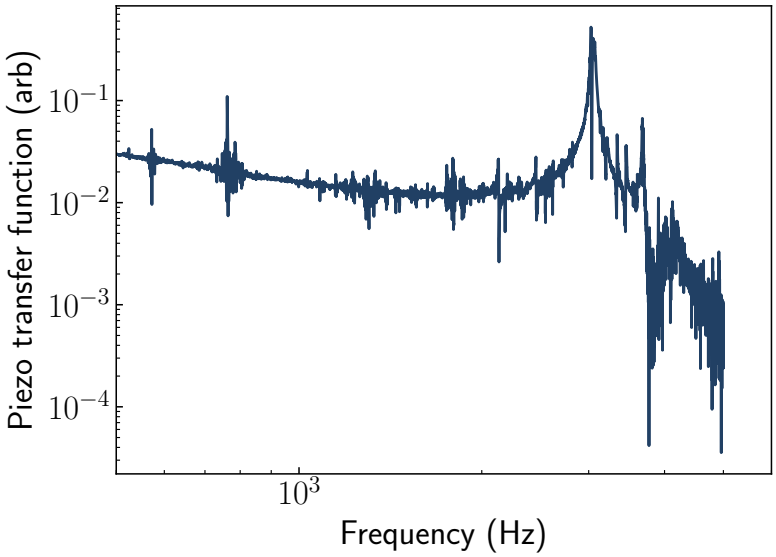

Figure 4.8: Piezo transfer function for epoxy cavity.

analysis.

4.4 Mechanical Network Analysis

The transfer function in Figure 4.8 incorporates the lockbox and piezo driver in the electrical domain, and the piezo's response in the mechanical domain. The electrical side is easy to understand; the transfer function falls off with frequency due to both the integrator in the lockbox, and the RC filter formed by the piezo driver with the capacitive piezo.

The mechanical side represents the combined properties of the piezo actuator, the mirror, and the entire mounting structure upon which the piezo sits. All of these objects have their own resonances, leading to the complicated transfer function observed. We wish to understand the properties of many interconnected mechanical objects. Luckily, every physicist knows a formalism for understanding interconnected electrical components: network analysis. Here we briefly review the analogous theory for mechanical networks, which will prove useful for understanding the issues with the previous cavity, and designing a proper

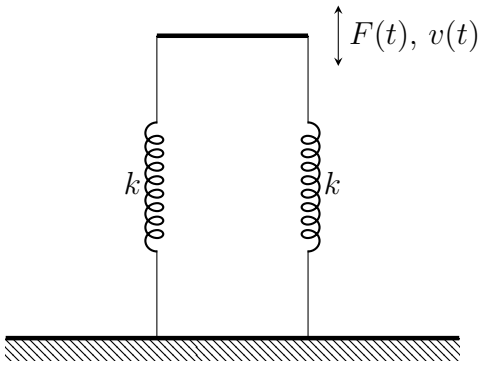

Figure 4.9: Two springs in parallel.

replacement.

4.4.1 Mobility Analogy

Consider an ideal spring fixed at one end, and driven sinusoidally on the other end. The position of the other end is goverend by Hooke's law, $F = kx$. Taking the time derivative and Fourier transform, this equation can be written in two suggestive ways:

$$F = \frac{k}{i\omega} v \tag{4.5}$$

$$v = \frac{i\omega}{k} F \tag{4.6}$$

where F is force, v is velocity, and k is the spring constant. Note that F and v are power-conjugate variables, exactly as are the voltage V and current I in the electrical domain.

The first equation resembles the definition of a capacitor's impedance, with the analogies $F \leftrightarrow V$, $v \leftrightarrow I$, and $\frac{1}{k} \leftrightarrow C$. Here C is capacitance.

Meanwhile, the second equation resembles an inductor's impedance, with the analogies $v \leftrightarrow V$, $F \leftrightarrow I$, and $\frac{1}{k} \leftrightarrow L$. Here L is inductance.

Which of these two interpretations should we choose? Consider now two springs in parallel, as in Figure 4.9. The spring constants should of course add, $k_{tot} = 2k$. In the first analogy, the springs are treated as capacitors with $C = \frac{1}{k}$, and the total capacitance is

Mobility Analogy			
Electrical		Mechanical	
Voltage	V	Velocity	v
Current	I	Force	F
Capacitance	C	Mass	m
Inductance	L	Compliance	$1/k$
Impedance	Z	Mobility	M

Table 4.2: Analogous quantities in the mobility analogy.

$C_{tot} = C + C = \frac{2}{k}$. The two spring constants have not added as expected.

In the second analogy, the springs are treated as inductors with $L = \frac{1}{k}$, and the total inductance is $L_{tot} = \frac{1}{1/L+1/L} = \frac{1}{2k}$. This latter correspondence produces the correct result. Thus we choose the so-called mobility analogy with $v \leftrightarrow V$, $F \leftrightarrow I$ to convert a mechanical network into an equivalent circuit[2]. The properties of the analogy are summarized in Table 4.2.

Another way to justify choosing this analogy is that charge Q and momentum p are both conserved quantities. Thus there is correspondence between Kirchhoff's current law (with $I = \frac{dQ}{dt}$) and Newton's second law (with $F = \frac{dp}{dt}$). Just as the sum of currents into a point must equal zero, the sum of forces on a point mass (including the inertial force $F = ma$) must equal zero. There is a similar correspondence between Kirchhoff's voltage law and velocity.

Two points are worth mentioning. First, one would expect that since $v \leftrightarrow V$, we would call the ratio of $\frac{v}{F}$ the impedance, so the impedance of a spring would be $Z_{\text{wrong}} = \frac{k}{i\omega}$. For all intents and purposes, this is correct. However, historically the other analogy was preferred, so it is universally agreed upon to call "mechanical impedance" the ratio of $\frac{F}{v}$. As that name is taken, we will call the the mobility $M = \frac{v}{F}$, which is the ratio of the "voltage-like" variable to the "current-like" variable in this analogy. Mechanical mobility thus plays

2. There is a circuit which produces the correct equations of motion using the first analogy, where $F \leftrightarrow V$, $v \leftrightarrow I$. However, this circuit has a different topology than the mechanical network. In fact, it is the dual topology, we can go from one analogy to the other simply by taking the dual circuit.

the same role as electrical impedance.

Second, the circuit analogy of a mass, which is a capacitor, always has one terminal connected to ground[3]. This is because the velocity of a mass is always measured with respect to a fixed reference frame. When writing out the equations of a motion for a point mass, one will never encounter a term like $m\left(\ddot{x}_1 - \ddot{x}_2\right)$.

4.4.2 Piezoelectric Transducers

We also need to construct the circuit equivalent of a piezoelectric transducer. The constitutive equations for a piezoelectric material can be modeled as [117, 118]

$$\boldsymbol{S} = \boldsymbol{s}^E \boldsymbol{T} + \mathfrak{d}^T \boldsymbol{E} \tag{4.7}$$

$$\boldsymbol{D} = \mathfrak{d} \boldsymbol{T} + \boldsymbol{\epsilon}^T \boldsymbol{E} \tag{4.8}$$

where $\boldsymbol{S}$ is the linearized strain tensor, $\boldsymbol{s}^E$ is compliance under constant $\boldsymbol{E}$ (short-circuit conditions), $\boldsymbol{T}$ is the stress tensor, $\mathfrak{d}$ is the piezoelectric tensor, $\boldsymbol{E}$ is the electric field, $\boldsymbol{D}$ is the electric flux density, and $\boldsymbol{\epsilon}^T$ is the permittivity tensor under constant $\boldsymbol{T}$ (unclamped conditions).

We use a 1D model, only considering uniaxial stress and strain, and only applying voltage in one direction. Further, we assume stress and strain are uniform through the piezo, which is valid because the axial resonant frequency of the piezo is far above the frequencies under consideration here (see Section 4.3.1). Then the quantities reduce to scalars: $\boldsymbol{S}$ becomes $\frac{\Delta l}{l}$ with piezo length l, $\boldsymbol{T}$ is $\frac{A}{k}$ with cross-sectional area A and spring constant k, $\boldsymbol{T}$ is $\frac{F}{A}$ with force F, $\mathfrak{d}$ is the piezoelectric charge constant, and $E = \frac{V}{t}$ with voltage V and layer thickness t.

3. Interestingly, the lack of an ungrounded capacitor makes it rather difficult to build a mechanical high-pass filter. In 2002, it was discovered that the mechanical equivalent of an ungrounded capacitor can in fact be built [116], though it is rather more complicated than just a mass. In fact, it need not Even be massive. Within four years, the so-called "inerter" was in use by Formula One cars.

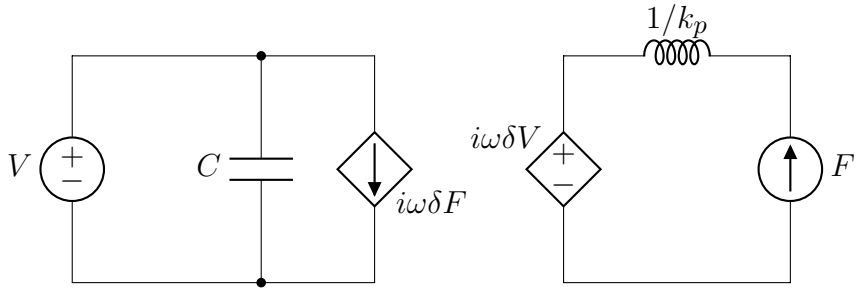

Figure 4.10: **Two-port network model of a 1D piezoelectric transducer.**

In the second equation $\boldsymbol{D}$ becomes $\frac{Q_l}{A}$ with free charge on each layer Q_l, $\boldsymbol{\epsilon}$ is $\frac{Ct}{AN_l}$ with capacitance C and number of layers N_l. Taking the time derivative and multiplying through by factors yields

$$v = \frac{1}{k}\dot{F} + \delta\dot{V} \tag{4.9}$$

$$I = \delta\dot{F} + C\dot{V} \tag{4.10}$$

where we have finally defined the effective piezoelectric charge constant of a multilayer actuator, $\delta = N_l\mathfrak{d}$.

This represents a two-port network, where one port is electrical and the other mechanical, as shown in Figure 4.10. On the mechanical side, the actuator looks like a velocity source (with magnitude $i\omega\delta V$), in series with a spring (i.e. an inductor with inductance $1/k_p$). There is an additional force F which comes from any mechanical elements external to the piezo. Now, we can use this model to understand the mechanical transfer function.

4.4.3 Circuit Model of Mechanical Resonances

The equivalent circuit of a piezoelectric actuator, attached on one end to a mounting structure and on the other end to a mirror, is shown in Figure 4.11(a).

The mount enters the model as an additional mobility M_m in series with the piezo, which

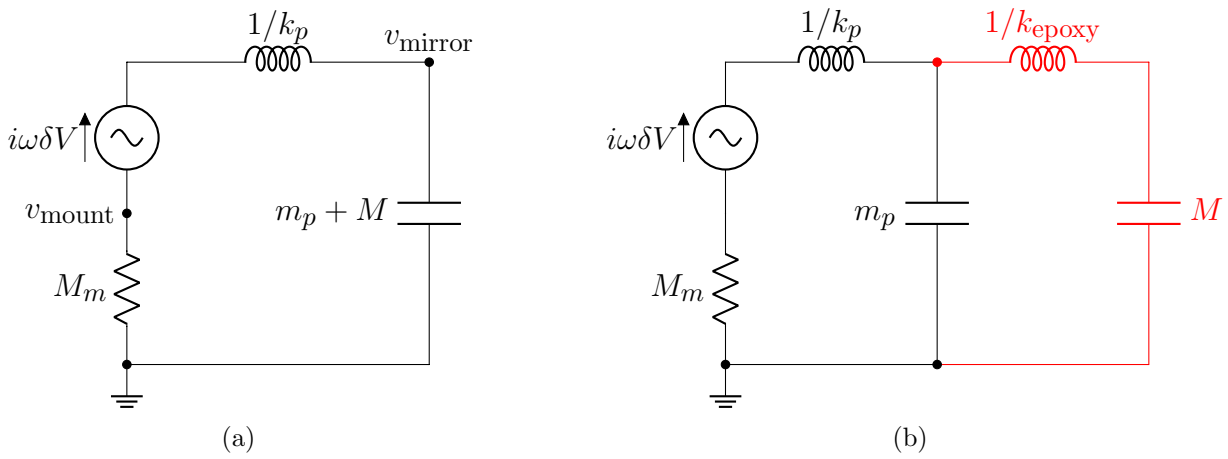

Figure 4.11: **Model of driven piezo interacting with mount and epoxy resonances. (a)** with very rigid epoxy, **(b)** with compliant epoxy.

may be an arbitrary function of frequency[4]. The length of the piezo defines a relative distance between its two faces, so active control of the piezo appears as a velocity source between the mount and mirror. In particular, this ensures that any "current" (force) entering the mirror is drawn from the mount – since there is no external force applied, the piezo must push on both equally for momentum conservation.

The origin of pole-zero type resonances is now clear. Suppose the mount has a resonance at frequency ω_a with a corresponding pole in M_m. At this frequency M_m diverges and the velocity at the mirror v_{mirror} goes to zero. This is an antiresonance frequency for the mirror[5].

However, because M_m rapidly goes from a small value to infinity and back, its magnitude passes through all real numbers in a small frequency interval. For a lightly damped structure, the phase can only be roughly 0 or π. Therefore at some nearby frequency ω_r, M_m exactly cancels the mobilities of the piezo and mirror. At this frequency v_{mirror} diverges, so this is a resonance for the mirror. Thus, resonances in the mount lead to pole-zero pairs in the mirror

4. Note that M_m is the actual transfer function of the mount, which may have a complicated 3D internal structure. We only require that its interaction with the piezo can be modeled as a 1D displacement

5. This is exemplary of a general result that, when driving and measuring at the same point, an anires-onance frequency corresponds to a resonance frequency for the rest of the structure, were that point held fixed [119]. This has interesting applications in characterizing quantum circuits, where a problematic lossy element can be tracked down by its very narrow antiresonance [120].

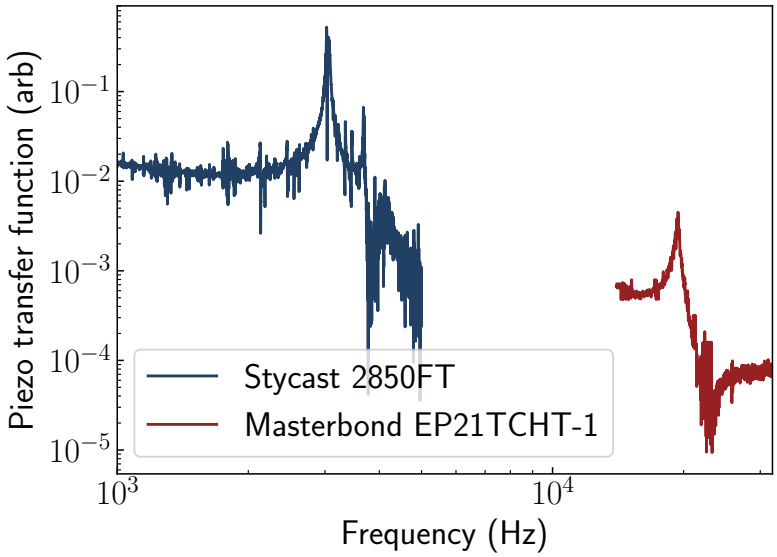

Figure 4.12: Comparison of mechanical transfer functions for different cryogenic epoxies.

transfer function. Generally, this is a consequence of Foster's reactance theorem [121].

What, then, is the origin of the lone pole in the transfer function from Figure 4.8? One explanation is a "mass-on-spring" or LC-type resonance of the piezo, where the impedance $\frac{i\omega}{k_p}$ and $\frac{1}{i\omega(m_p+M)}$ sum to zero at $\omega = \sqrt{\frac{k_p}{m_p+M}}$. However, the mirror is very light, and the piezo is very stiff, so this shouldn't occur until well over 100 kHz.

The answer is provided in Figure 4.11(b). Here we separate out the epoxy as a separate spring constant. Then there is a resonance defined by k_{epoxy} and M. Evidently, the epoxy loses its hold during cooldown, and becomes a very weak spring! This is the origin of the large resonance at 3 kHz.

To remedy this situation, I first tried constructing cavities with other cryogenic epoxies. The best results came from using Masterbond EP21TCHT-1. Figure 4.12 shows a comparison of transfer functions of the original Stycast cavity and a Masterbond cavity which also had the invar washers removed. The Masterbond cavity had a first resonance at 20 kHz, and indeed had excellent vibrational performance. However, even with this epoxy, results were inconsistent: an identically prepared cavity had a resonance at 10 kHz. This is right on

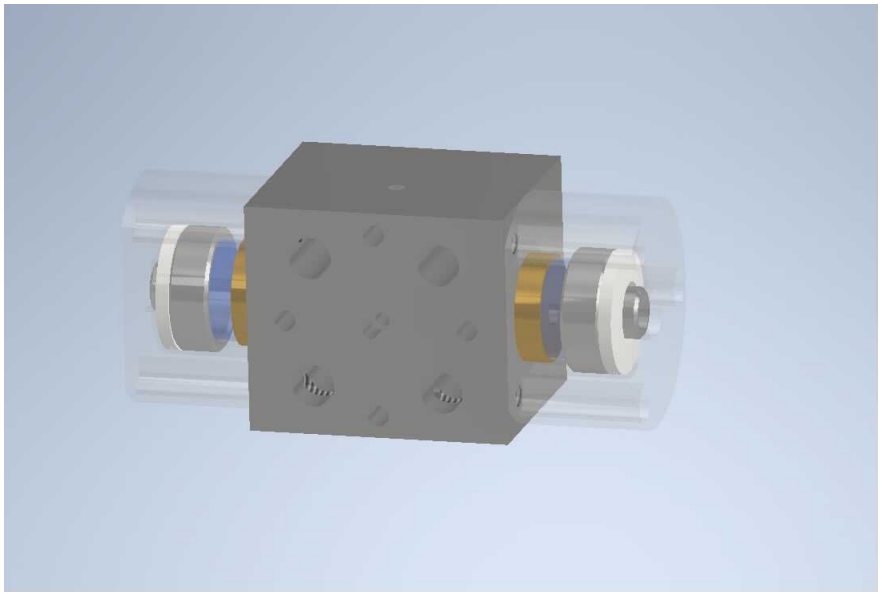

Figure 4.13: CAD model of spring preload mirror mounts on optical cavity.

top of the spike of pulse tube noise, so there was again order of 1 nm of shaking. Another solution is needed.

4.5 Spring Preload Cavities

The problem of constructing our optical cavity is essentially one of bonding dissimilar materials. The spacer, piezos, and mirrors are all of different composition. Normally epoxy is a fantastic solution to this problem, and epoxied mirror-piezo assemblies can reach resonance frequencies of 180 kHz or more [122], limited by factors besides the epoxy. However, as we have seen, the properties of epoxy degrade at cryogenic temperatures, introducing major resonances. Some ultrastable cryogenic resonators get around this problem by using only sapphire or single-crystal silicon components which can be optically contacted, but this is not an option for us.

Another possible solution is to clamp mirror, piezo, and spacer together, for example by screwing the stack between two metal plates. But a stiff clamp limits the motion of the piezo. Furthermore, the force applied by a stiff clamp varies strongly with length, so a tiny length

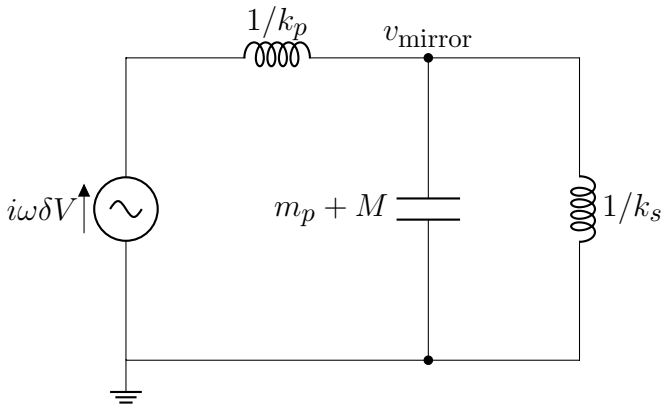

Figure 4.14: Circuit model of spring preload mirror mount.

intolerance would crack the mirror or loosen the clamp. Even with precision fabrication, thermal contraction during cooldown would change the clamp length.

All of these problems can be solved by placing a compliant spring with low spring constant k_s between the stack and the rigid clamp. Even with a weak spring, an arbitrarily high preload force can still be applied by compressing the spring sufficiently. The dependence of force on manufacturing tolerance and thermal contraction is small, $\frac{dF}{dL} = k_s$.

One might worry that the introduction of a compliant spring would introduce low-frequency resonances, similar to the weakened epoxy. However, examining the circuit model of a spring preload mirror mount in Figure 4.14, it is clear that the preloading spring enters in parallel to the piezo's compliance, rather than in series, so it increases the effective spring constant. It is also clear from this model that the zero-frequency range of the piezo is reduced by a factor of $\frac{k_p}{k_p+k_s}$, which is minor for small k_s.

A final concern is that the weak spring may have self-resonances due to its non-zero mass. A self-resonance frequency corresponds to infinite mobility, which the circuit model in Figure 4.14 suggests would have minimal effect as it is in parallel with the mirror. However, a spring self-antiresonance corresponds to infinite stiffness, so the mirror would see zero displacement. Along with this zero would come a corresponding pole in the piezo transfer function, by the same argument as before. Furthermore, above a spring's first self-resonance

frequency, we would not expect ideal behavior; modeling the spring as a 1D elastic bar reveals that the rolloff of a mass-spring system decreases to $1/\omega$ after the first resonance. For these reasons I choose a rather light and stiff spring which should have high self-resonance frequencies.

4.5.1 Preloading Piezoelectric Actuators

Piezo actuators very commonly have a compressive preload force applied to them by a compliant spring, in order to protect them from tensile stresses in dynamic operation. This is relevant when the actuator moves a large mass at high frequencies, and often a large compressive stress of order 15 MPa is used. In the present case, the preload serves an entirely different purpose: to keep the mirror pressed tightly to the piezo, and the piezo pressed tightly to the cavity. The preload force need only be sufficient to push the mirror against the piezo during the maximum expected acceleration. During locking, displacements are very small, so the maximum acceleration will occur while scanning for a resonance. The force needed to accelerate a mirror of mass M while scanning the piezo is

$$F_{\text{preload}} = Mx\omega_{\text{scan}}^2 \tag{4.11}$$

where x is the scan range and ω_{scan} is the scan frequency. For $M = 0.5$ g, $x = 2\mu$m (the full piezo range), and $\omega_{\text{scan}} = 2\pi \times 1$ kHz, $F_{\text{preload}} = 0.04$ N, with a stress of less than 1 kPa for the cross-sectional area of our piezos.

A much larger preload force will be used anyway, primarily because a reasonably stiff spring is desired, and it must be designed for at least ~ 0.1 mm compression to avoid unrealistic machining tolerances. Also, preloading is known to make the piezo behave more ideally and increase achievable strain [123]. This effect arises from the alignment of ferroelectric grains which were not perfectly aligned in the poling process.

There is a tradeoff for preload spring stiffness. A low stiffness allows for looser dimensional tolerances, but a high stiffness-to-mass ratio may push resonance frequencies higher.

4.5.2 Spring Preload Design

A CAD model of the spring mirror mount design, attached to an optical cavity, is shown in Figure 4.13. The individual components are shown laid out in Figure 4.15. The design consists of the usual piezo and mirror, as well as a guidepin, two stacked conical disc springs (Belleville disc springs), an aluminum housing tube, and an optional lid. One end of the guidepin has a depression to fit the mirror. The other end of the guidepin is a long, hollow tube, which passes through both the disc springs, and a central hole in either the housing or the lid, depending on the design. This serves to center both mirrors and disc springs relative to the housing. All components have central holes to allow light into and out of the structure.

The stack of piezo, mirror, guidepin, and springs is assembled inside the aluminum housing. Then the cavity spacer can be attached to the housing with screws (no lid design), or a lid can be attached similarly (lid design), and later the assembly can be attached to the cavity spacer. The inside length of the housing equals the height of the stack (measured precisely with a height gauge), minus the desired deflection of the springs.

The lid design is slightly more convenient for its portability; also, the piezo can be centered precisely by matching its ID to a hole in the housing, and passing a cylinder through both during assembly. However, the lid design has slightly more mass, which could in principle hurt vibrational performance.

The disc springs are McMaster-Carr part number 9713K14. Each has outer diameter 0.343", inner diameter 0.164", thickness 0.019", height 0.028", and mass 0.13 g. The rated working load is 55 lbf (245 N), at which point the deflection is 0.005" (0.13 mm). This deflection is well within the machining tolerance of the housing. Usually two disc springs,

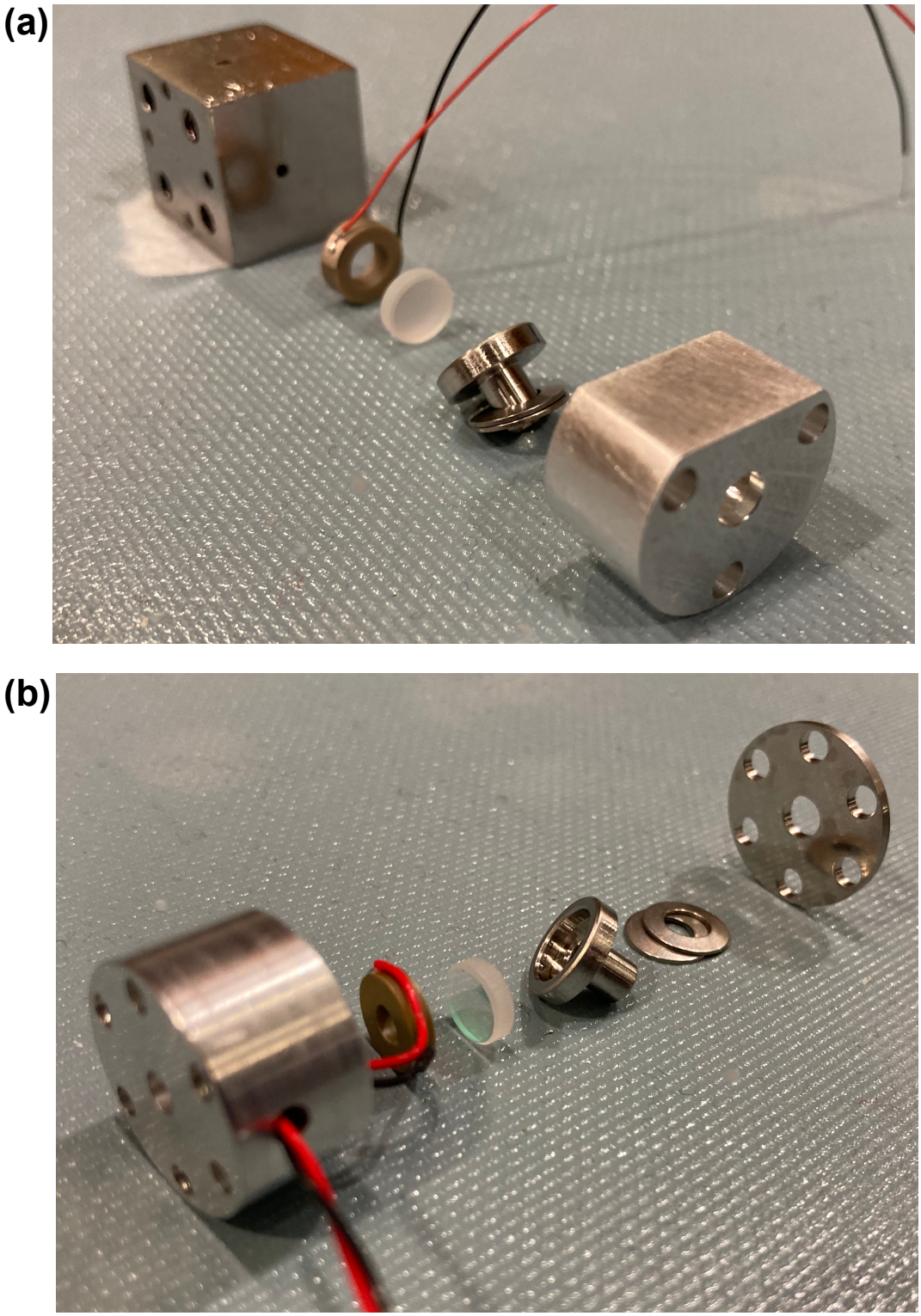

Figure 4.15: **Components of spring mirror mounts laid out.** **(a)** no lid design, **(b)** lid design.

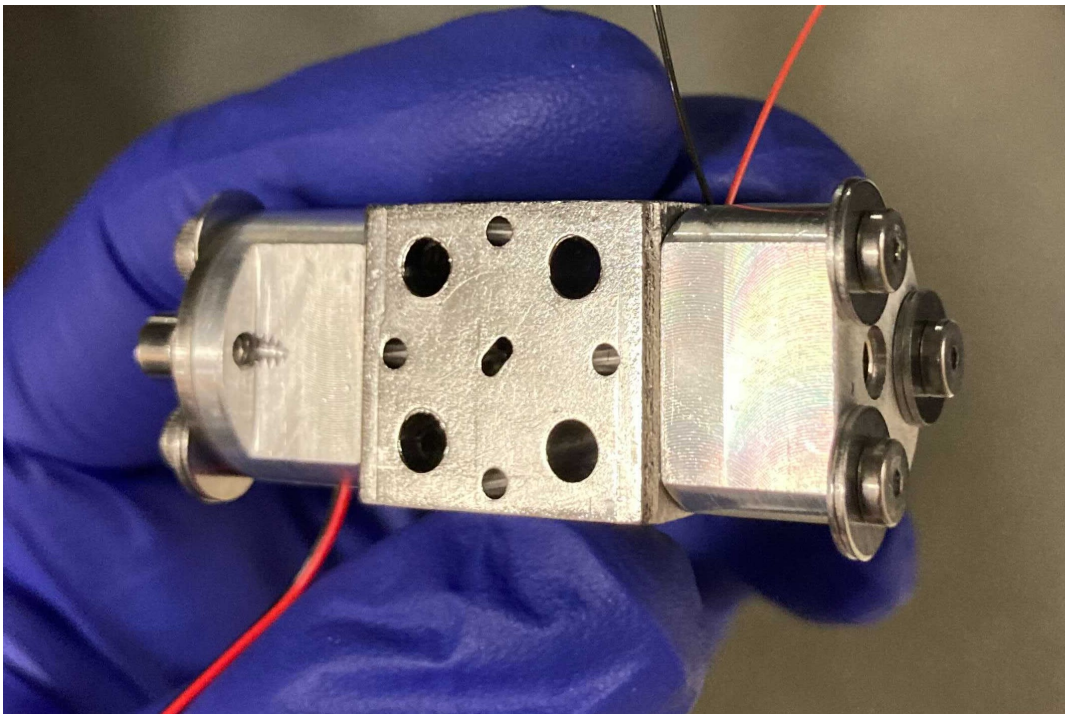

Figure 4.16: Completed cavity with spring mirror mounts.

stacked in the same orientation (this is known as the parallel configuration), are used to double the stiffness [124], though one spring has been found to work similarly well. Disc springs stacked in opposite orientations add like springs in series, so this is known as the series configuration.

The guidepins have a mass of 2.26 g. This has varied mildly between various designs. The clearance between the guidepin and its matching hole in the housing (or lid) is 0.002" in our design, to accomodate thermal contraction. At one point after a warmup the guidepin apparently became stuck due to stiction with the housing. The piezo would not move, and the cavity finesse degraded considerably, perhaps due to mirror stress. After the maximum piezo voltage was applied, there was a loud click as the stiction loosened, and the piezo movement and cavity finesse were both recovered.

A completed cavity with spring mirror mounts in shown in Figure 4.16, where one mount is the lid design and the other is the no lid design. The two show similar performance.

4.5.3 Material Considerations

Spring material selection is usually guided by the need for an extremely high yield strength, as well as high stiffness and, ideally, low density. We have the additional requirement that the material be nonmagnetic, even at cryogenic temperatures. As a general rule, density and elastic moduli are mostly unaffected by alloying elements, while yield strength and magnetic properties are affected.

Some useful information about cryogenic material properties can be found in [125, 126]. The 300 series stainless steels are nonmagnetic, due to their austenitic crystal structure. Still, even nonmagnetizable steels at room temperature may become magnetizable at cryogenic temperatures. The more stable the austenite structure, the better. 304 steel is good, 316 is sometimes considered better, nitrogen-containing austenitic steels are excellent, and high-manganese steels are the best.

Austenitic stainless steels can be used as springs, but only when their yield strength is increased by strain hardening. Some austenitic steels, including X10CrNi18-8, become magnetizable after strain hardening, while others, including X5CrNiMo17-12-2, are resistant. Nevertheless, we chose 302 steel disc springs available on McMaster-Carr and haven't had any issues.

Aluminum and titanium alloys are nonmagnetic, but may become brittle at cryogenic temperatures (less so for extra-low-interstitial titanium alloys). Also, aluminum springs are usually not manufactured due to its lack of a fatigue limit and low yield strength. Likely none of these are important limitations due to the low forces involved in mirror positioning, and future designs would likely benefit from using aluminum or titanium alloys. One worry is that Ti-6Al-4V goes superconducting between 4K and 5K. Aluminum, titanium, and steel all have high (and roughly equal) ratios of Young's modulus to density, which is important for high resonance frequencies.

Beryllium copper is nonmagnetic and has excellent cryogenic properties. However, it has

a worse ratio of elastic moduli to density than other options. Also it is highly toxic if inhaled.

Disc spring manufacturers usually specify strict requirements for the mating surfaces of the springs. For example, Christian Bauer recommends that the clearance between the spring's inner diameter and the guidepin be 0.15 mm. They also recommend that the guidepin and both flat surfaces compressing the spring have surface hardness > 55 HRC and be ground and polished to reduce friction. Finding cryogenic, nonmagnetic materials with such properties is difficult.

As a substitute, I used nitronic 60 stainless steel for the guidepins and lids, as it is known to have excellent resistance to galling, and excellent magnetic properties at cryogenic temperatures, as nitrogen stabilizes the austenitic structure. However, the no lid design, which uses aluminum on one compression surface, had equal performance as the lid design. Because the forces on these springs are small, likely these guidelines matter very little.

4.5.4 Performance of Spring Mirror Mounts

The vibrational performance of the spring mirror mount is shown in Figure 4.17, measured with similar techniques as in Section 4.3.3. The first major mechanical resonance in the transfer function occurs at 18 kHz. As expected, the overall shaking amplitude is much less than for the epoxy cavity, at approximate 0.15 nm peak-to-peak ((a)) or 0.02 nm rms ((c)). Even the peak-to-peak shaking is less than the linewidth of a finesse 2500 cavity. This allowed a complementary measurement of the shaking in which the VCO lock was turned off, and the error signal was monitored directly, which was be calibrated to give the cavity length. The result was very similar to this VCO lock measurement.

Examining the integrated rms length ((c)) shows that noise enters gradually in a band around 10 kHz, and again in the range of 18-30 kHz. The 10 kHz noise can be attributed to the large spike in pulse tube noise at this frequency, observed qualitatively by the accelerometer in Figure 4.3. The noise between 18 and 30 kHz, on the other hand, can be tied exactly

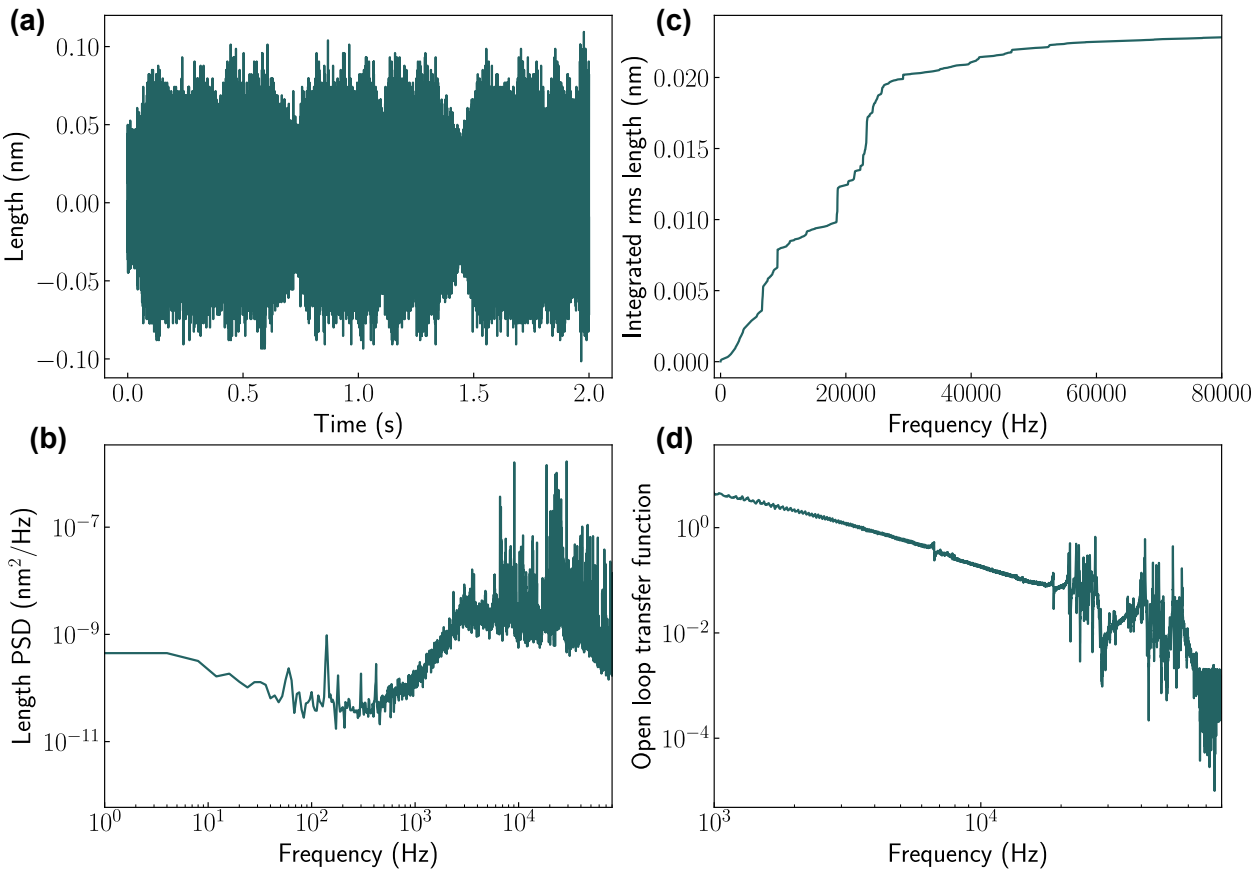

Figure 4.17: **Length shaking of spring cavity.** **(a)** Absolute displacement, **(b)** Power spectral density of displacement, **(c)** Integrated RMS Displacement, **(d)** Transfer function.

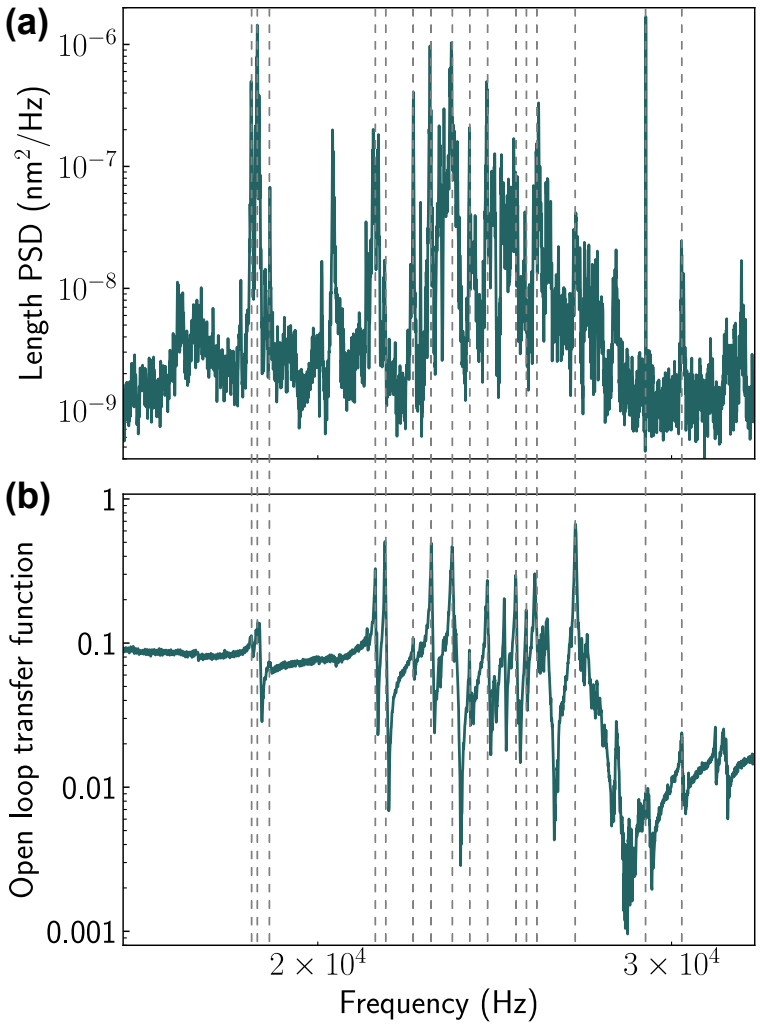

Figure 4.18: Zoomed-in view of **(a)** Power spectral density of displacement, **(b)** transfer function, showing correspondence between resonances and noise.

to the cavity resonances seen in the transfer function.

A detailed comparison between the power spectral density and transfer function in this range is presented in Figure 4.18. The shaking occurs exactly at the mechanical resonances, with noise suppressed 2-3 orders of magnitude at other frequencies. This confirms that the majority of the cavity length instability arises from mechanical resonances in the cavity structure, which are excited by ambient noise from the pulse tube. It seems there would be additional benefit from pushing these resonance frequencies even higher.

Mechanical resonances occur frequently above 20 kHz, separated by less than a kHz.

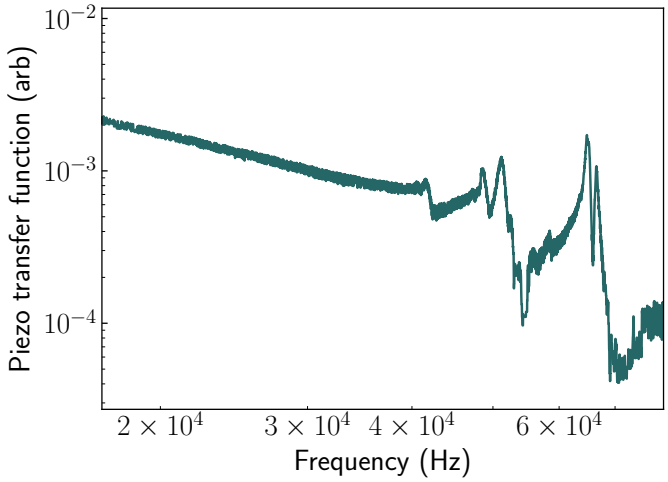

Figure 4.19: Mechanical transfer function for a shorter mirror in a spring-piezo mount, with higher resonance frequencies.

A similar transfer function was observed when the spring box was mounted standalone, so the resonances probably do not come from the cavity spacer. It is unlikely that the mass-on-spring mode of the mirror and guidepin mass and piezo stiffness plays a role, as that is estimated to occur around 100 kHz, and also all observed resonances enter as pole-zero pairs. One possibility is that these could be self-resonances in the disc springs. Another is that the resonances could belong to the aluminum housing tube, plus the associated screws attaching it to the cavity. Finite element simulation of the tube alone suggests no resonances below 44 kHz, but mechanical resonances arising from bolted structures can be difficult to simulate.

To help distinguish between these possibilities, I created another spring-mounted mirror, but using a flat, 2 mm thick mirror rather than a 4 mm thick mirror with 25 mm radius of curvature. The housing tube is correspondingly shorter by 2 mm, with 7.85 mm total length. The transfer function is shown is Figure 4.19. In this case, the first resonance occurs above 40 kHz, a dramatic improvement. The change seems to rule out self-resonances in the disc spring. This lends support to the explanation that the resonances arise from the mechanics of the housing tube and associated fasteners. In any case, I expect that incorporating this

shorter-mirror design into the cryostat would improve vibrational performance dramatically.

4.5.5 Temperature Dependence

There is a clear connection between resonance frequencies and vibrational performance: pushing the first resonance to higher frequencies is helpful, because there is less noise to resonantly couple in at higher frequencies.

In addition, we have observed a change in vibrational performance with temperature. Figure 4.20(a) shows the rms length of the cavity as a function of time, averaged in 4 ms bins, at 245 K and 9 K temperatures. The peak amplitude is similar. However, the vibrations ring down quickly after each pulse tube hit at warm temperatures, whereas they ring almost until the next pulse tube hit at cryogenic temperatures. An obvious explanation is increased material quality factors at cryogenic temperatures [127, 128, 129], which would lead to longer resonance ringdowns. This should appear as narrower peaks in the transfer function; indeed, Figure 4.20(b) shows peaks about 10 times narrower and significantly taller at cryogenic temperatures. It is also possible that noise in the environment persists longer due to increased quality factors of the copper plates, etc.

4.6 Conclusion

By joining the components of an optical cavity with compliant springs instead of epoxy, we have eliminated the problematic resonances which result from degradation of epoxy at cryogenic temperatures. The spring preloaded mirror mount cavities are sufficiently stable for our current experiments at finesse ~ 3000.

For higher finesse cavities, the linewidth decreases, generally requiring higher stability. However, for many of our experiments, the absolute frequency of the cavity is not too important, so long as it is within ~ 1 atomic linewidth (6 MHz) from the rubidium D2 transition frequency. Then we can simply have the laser follow the cavity with no penalty.

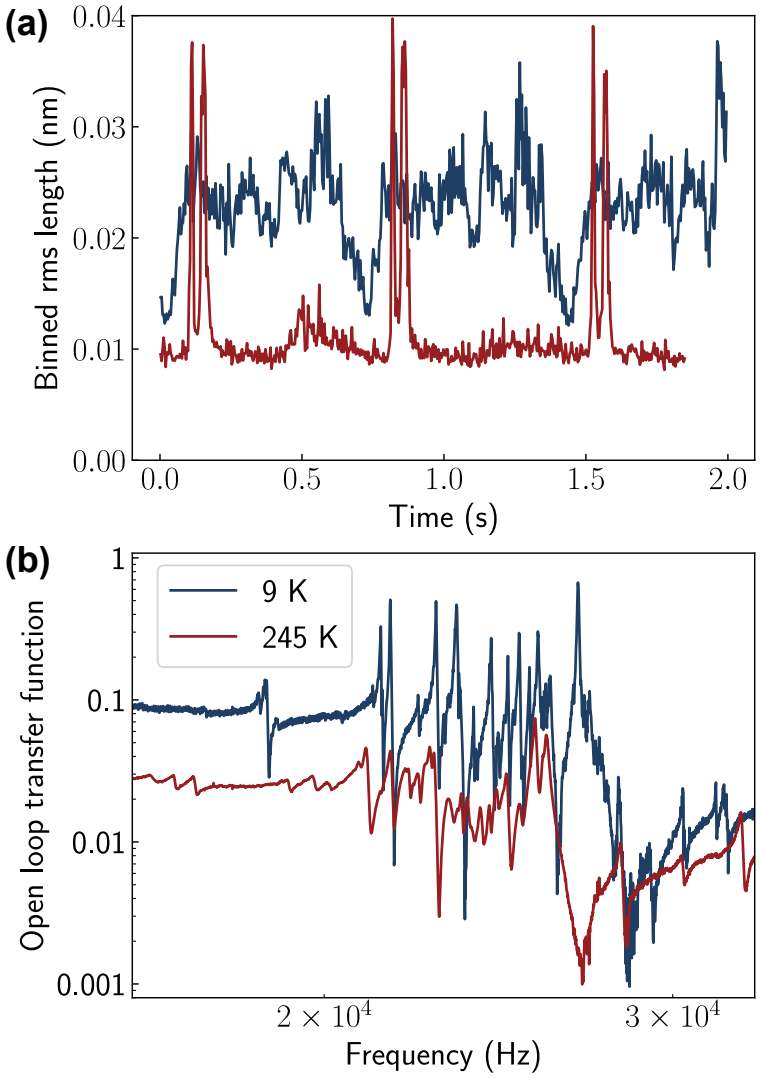

Figure 4.20: Temperature variation in spring cavity of **(a)** RMS vibrational amplitude (averaged in 4 ms bins), **(b)** transfer function, showing increased quality factor at low temperatures.

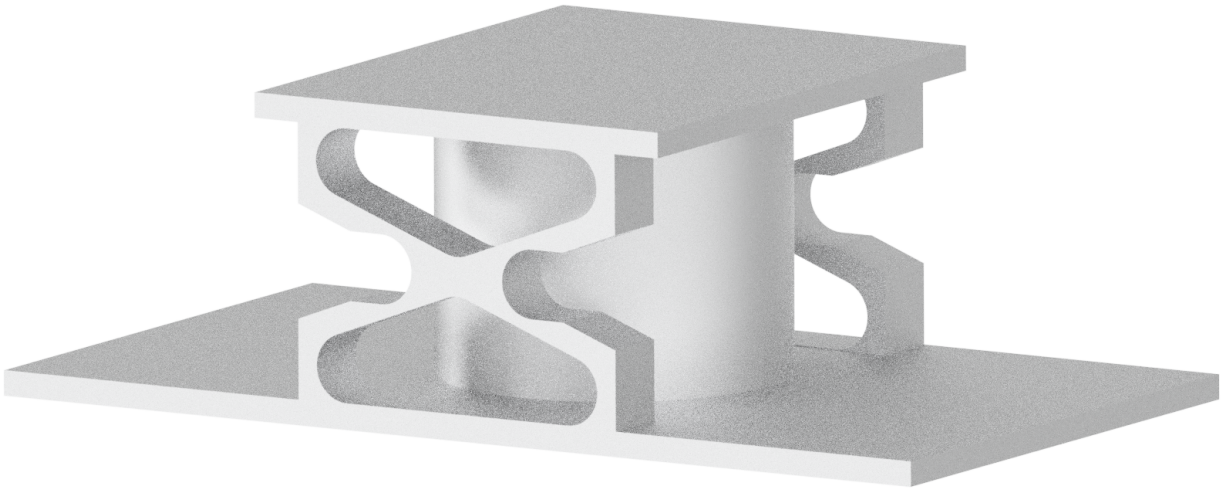

Figure 4.21: Potential design for an extensional flexure spring mirror mount.

For other experiments, it may be useful to improve vibrational performance further. The easiest solution would be to go to smaller mirror substrates. Indeed, fiber mirrors seem to be immune to these epoxy resonances, as they are very light and can be completely encapsulated in epoxy, though larger mirrors than this are needed to surround the mm-wave cavity. All of the strategies discussed in Section 4.1 could be helpful, particularly low-pass vibration isolation stages. There will also likely be a large benefit from the shorter mirror design shown in Figure 4.19, which pushes the first resonance frequency from 18 kHz to > 40 kHz.

No doubt the mechanical design could be optimized further. A number of groups have created nanopositioners using blade flexures to preload piezoelectric actuators [130, 131, 132], which could be adapted for mirror mounting. These have achieved resonance frequencies up to 26 kHz, but would likely be better with shorter piezos. Another group has created a preloaded cryogenic mirror mount [133] using a flexural extension spring in parallel to the piezo. A similar concept shown in Figure 4.21 has simulated resonances over 40 kHz, and could be machined as a single piece using waterjet or EDM, avoiding bolt resonances. Pushing the resonance frequencies up further with such designs would improve resilience to noise from the cryocooler.

CHAPTER 5

OPTICAL TO MM-WAVE TRANSDUCTION

The goal of this chapter is primarily to introduce the mathematical formalism we use to understand optical to mm-wave transduction in atomic systems, and also to describe the state of the experimental progress toward this goal, which is ongoing. An ideal quantum transducer can be described by a beam-splitter Hamiltonian, $H = c^\dagger b + b^\dagger c$. In the input-output formalism, this Hamiltonian creates a linear and entanglement-preserving mapping from input field operators in the mm-wave domain to output field operators in the optical domain (or vice versa). At the same time, the internal state of the transducer should be left unchanged, so that no information is left in the transducer.

We will begin by writing down the Hamiltonian for our transducer, with two cavities and two control beams coupled to an ensemble of atoms. This Hamiltonian has two significant differences from the analysis of cavity electromagnetically induced transparency in previous chapters. First, the collective states which greatly simplified the Hamiltonian in previous sections can only do so when all atoms couple uniformly to all fields in this case. Second, the presence of a classical ultraviolet control field coupled to the ground state of the atoms means that we can no longer separate the Hilbert space into a single zero-excitation vacuum state, plus a small set of higher-order excitation states. This separation is essential for the linearized perturbation theory employed in earlier chapters. Indeed, each atom can be in a different superposition of its ground state and a Rydberg state coupled by the ultraviolet laser, giving 2^N possible states.

There are two regimes where the system is easily solved. First, in far off-resonant operation, there is negligible population of all non-ground atomic states, and adiabatic elimination of the atoms [134, 24] recovers a unique vacuum state and a beamsplitter Hamiltonian. Second, in the presence of a very strong or far-detuned ultraviolet drive, the atoms can be expressed in the dressed state basis, and the off-resonant dressed state for each atom can be

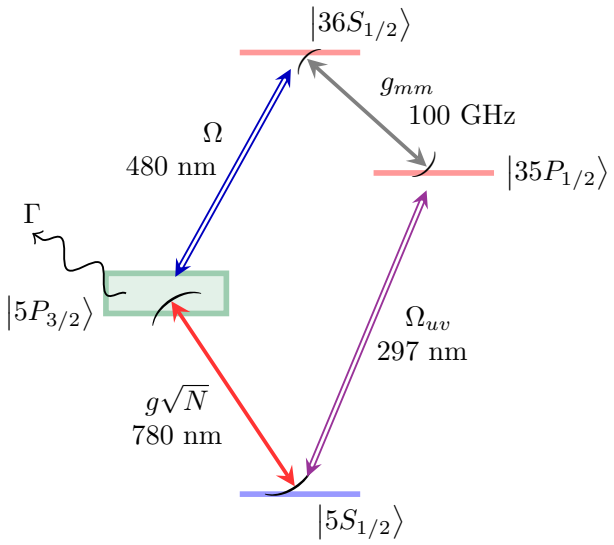

Figure 5.1: Relevant energy levels for optical-mmwave transduction.

dropped from consideration. This again recovers a unique vacuum state. The latter scheme is valid even for all-resonant operation, and reduces to the former when all beams are far detuned. Using this analysis, we will predict the performance of the transducer under realistic experimental conditions.

5.1 Basics of Atomic Transduction

An ideal quantum transducer performs a unitary transformation between photons at two frequencies. This means that the conversion process is reversible, lossless, and coherent. These conditions are required to perform transduction without altering the quantum state of the information.

Practically, the solution involves a mediator which can be excited by light at either frequency. The rate at which photons are absorbed by the mediator must be much greater than the rate of any loss processes; this ensures lossless conversion, and is quantified by the cooperativity at each frequency. The coupling rate at one frequency should equal the coupling rate at the other frequency; this is the impedance matching condition, and ensures

that photons are transduced instead of simply reflected. Finally, the coupling rates set a maximum bandwidth for conversion, and thus should exceed the expected rate of input photons.

We will use a cloud of rubidium atoms as a mediator. A diagram of the relevant energy levels is shown in Figure 5.1. Rubidium has a strong electron dipole transition from the ground state $|5S_{1/2}\rangle$to the excited state $|5P_{3/2}\rangle$at 780 nm, which will be used to interface with the optical field. Meanwhile, an atom in a Rydberg state has strong inter-Rydberg level transitions with frequencies dependent on the choice of Rydberg level. By working at $n = 36$, we have access to transitions near 100 GHz. A strong ultraviolet laser is used to promote atoms from the ground state to this Rydberg level.

Transduction can be simply understood as a cyclic process for the atoms. An atom is promoted by a laser at 297 nm to the $|^{35}P_{1/2}\rangle$ state. An incoming 100 GHz photon brings the atom to the $|^{36}S_{1/2}\rangle$ state, aided by a resonator. Another classical beam at 480 nm brings the atom down to the $|5P_{3/2}\rangle$state, where it can emit a photon at 780 nm, again aided by a resonator.

The beams at 297 nm and 480 nm provide the energy to bring the atom up and down to the Rydberg manifold, maintaining energy conservation. There are thus four frequencies at play, making this a four-wave mixing (FWM) process. Other schemes for microwave-to-optical transduction have proposed using an atomic ground state hyperfine transition to interface with the microwave field. These schemes need only one classical beam at the difference frequency of the optical and microwave fields to ensure energy conservation, so a three-wave mixing process is also possible[1]. However, the ground state magnetic dipole transition is quite weak, making it difficult to achieve sufficient coupling rate.

1. Since all transitions used in the FWM scheme couple to the electron dipole moment, selection rules require that $\Delta L = \pm 1$. Therefore, a cyclic process requires an even number of transitions, another reason for using a four-wave mixing process. In the three-wave mixing process, the microwave transition couples to the ground state magnetic dipole moment, altering the selection rules

5.1.1 Transducer Hamiltonian

By adding an ultraviolet laser, we can write down the Hamiltonian for optical - mm-wave transduction. In the rotating wave approximation, the Hamiltonian is:

$$H = \omega_a \hat{a}^\dagger \hat{a} + \omega_b \hat{b}^\dagger \hat{b} + \sum_i \Big[\omega_e \hat{\sigma}_i^{ee} + \omega_r \hat{\sigma}_i^{rr} + \omega_f \hat{\sigma}_i^{ff} + \left(g_i \hat{a} \hat{\sigma}_i^{eg} + h.c. \right) + \left(\Omega_i e^{-i\omega_{blue} t} \hat{\sigma}_i^{re} + h.c. \right) + \left(h_i \hat{b} \hat{\sigma}_i^{rf} + h.c. \right) + \left(\Upsilon_i e^{-i\omega_{uv} t} \hat{\sigma}_i^{fg} + h.c. \right) \Big] \quad (5.1)$$

The usual procedure to remove time dependence of the classical coupling fields is to transform all atomic levels into the rotating frame. In the present case, due to the cyclic nature of the transitions, there will be additional constraints on the rotating frame transformation. We will work in a frame where the optical and mm-wave cavity field operators $\hat{a}$ and $\hat{b}$ rotate at frequencies of ω_o and ω_m, respectively, which will ultimately correspond to the input and output frequencies. Meanwhile, the atomic levels $|e\rangle$, $|r\rangle$, and $|f\rangle$ rotate at frequencies ω_o, $\omega_o + \omega_{blue}$, and $\omega_o + \omega_{blue} - \omega_m$.

This transformation will result in a Hamiltonian with no time dependence, except for one term which becomes $\frac{\Upsilon_i}{2} e^{i(\omega_o + \omega_{blue} - \omega_m - \omega_{uv})t} \hat{\sigma}_i^{fg}$. This time dependence can only be canceled if we choose ω_o and ω_m such that

$$\omega_o + \omega_{blue} - \omega_m - \omega_{uv} = 0 \quad (5.2)$$

This constraint arises because $|f\rangle$ (and every other state) is connected to the ground state by two paths, both of which must have their time dependence canceled. The constraint can be viewed is a statement of energy conservation – for an input optical photon at frequency ω_o and fixed pump frequencies, the output mm-wave photon will be emitted at a frequency of $\omega_m = \omega_o + \omega_{blue} - \omega_{uv}$.

Our rotating frame amounts to examining a transformed wavefunction $|\tilde{\psi}\rangle = e^{iAt} |\psi\rangle$,

with $A = \omega_o a^\dagger a + \omega_m b^\dagger b + \sum_i \left[\omega_o \hat{\sigma}_i^{ee} + (\omega_o + \omega_{blue})\,\hat{\sigma}_i^{rr} + (\omega_o + \omega_{blue} - \omega_m)\,\hat{\sigma}_i^{ff}\right]$. In this rotating frame, the Hamiltonian becomes

$$H = \delta_a \hat{a}^\dagger \hat{a} + \delta_b \hat{b}^\dagger \hat{b} + \sum_i \Big[\delta_e \hat{\sigma}_i^{ee} + \delta_r \hat{\sigma}_i^{rr} + d_f \hat{\sigma}_i^{ff} + \left(g_i \hat{a} \hat{\sigma}_i^{eg} + h.c.\right) + \left(\Omega_i \hat{\sigma}_i^{re} + h.c.\right) + \left(h_i \hat{b} \hat{\sigma}_i^{fr} + h.c.\right) + \left(\frac{\Upsilon_i}{2} \hat{\sigma}_i^{fg} + h.c.\right)\Big] \quad (5.3)$$

Here $\delta_a = \omega_a - \omega_o$, $\delta_b = \omega_b - \omega_m$, $\delta_e = \omega_e - \omega_o$, $\delta_r = \omega_r - \omega_{blue} - \omega_o$,$\delta_f = \omega_f - \omega_{uv}$, and we have chosen $\omega_o, \omega_m$to satisfy the aforementioned equality in Equation 5.2.

5.1.2 Phase Matching

So far we have not mentioned the propagation phase factor $e^{i\boldsymbol{k}\cdot\boldsymbol{r}}$ of each laser, which is implicit in the coupling constants $\Omega_i, \Upsilon_i, g_i$ for an atom at position $\boldsymbol{r}_i$.These phase factors can be removed with an additional unitary transformation to the atomic wavefunctions, $|\tilde{\psi}_i\rangle = T_i^\dagger |\psi_i\rangle$,and

$$T_i^\dagger = \begin{pmatrix} 1 & 0 & 0 & 0 \\ 0 & e^{-i\boldsymbol{k}_{780}\cdot\boldsymbol{r}_i} & 0 & 0 \\ 0 & 0 & e^{-i(\boldsymbol{k}_{480}+\boldsymbol{k}_{780})\cdot\boldsymbol{r}_i} & 0 \\ 0 & 0 & 0 & e^{-i\boldsymbol{k}_{uv}\cdot\boldsymbol{r}_i} \end{pmatrix}$$

This yields a Hamiltonian (now explicitly including spatial phase factors)

$$H = \delta_a \hat{a}^\dagger \hat{a} + \delta_b \hat{b}^\dagger \hat{b} + \sum_i \Big[\delta_e \hat{\sigma}_{ee}^i + \delta_r \hat{\sigma}_{rr}^i + d_f \hat{\sigma}_{ff}^i + \left(g_i \hat{a} \hat{\sigma}_{eg}^i + h.c.\right) + \left(\Omega_i \hat{\sigma}_{re}^i + h.c.\right) + \left(P_i h_i \hat{b} \hat{\sigma}_{rf}^i + h.c.\right) + \left(\frac{\Upsilon_i}{2} \hat{\sigma}_{fg}^i + h.c.\right)\Big] \quad (5.4)$$

with all of the phase factors included in the factor

$$P_i = e^{-i(\boldsymbol{k}_{480}+\boldsymbol{k}_{780}-\boldsymbol{k}_{mm}-\boldsymbol{k}_{uv})\cdot\boldsymbol{r}_i} \tag{5.5}$$

As was the case for the time dependence, the spatial phase for each atom cannot be removed from the Hamiltonian unless $\boldsymbol{k}_{480} + \boldsymbol{k}_{780} - \boldsymbol{k}_{mm} - \boldsymbol{k}_{uv} = 0$. Given the previously stated requirement that $\omega_o + \omega_{blue} - \omega_m - \omega_{uv} = 0$ and $\omega = c\,|k|$, the phase matching condition is met when all beams are copropagating[23]. We will assume this is the case, so that $P_i = 1$,[4] which yields the final Hamiltonian under phase-matched conditions.

5.2 Resonant Transduction

Far off-resonant operation allows all excited states of the atoms to be adiabatically eliminated from the problem [134, 24], yielding reversible transduction between optical and mm-wave frequencies. However, the conditions of adiabatic elimination require negligible atomic population of the Rydberg f state. Thus, while the Rabi frequency of the 780 nm transition in our scheme is enhanced by a factor of $\sqrt{N}$, where N is the atom number, the mm-wave Rabi frequency is just the single-atom value. Even though the single-atom mm-wave Rabi frequency is quite high in our system (200-300 kHz), this is lower than the other frequencies in the system, and thus is a limiting factor for the bandwidth.

It is thus desirable to have macroscopic population of the lower Rydberg state f. This

2. Generally we do not have good control over the wave vector for our mm-wave mode, which leads to phase mismatch on the order of $P_i = e^{ik_m z_i}$. This leads to a phase variation of 2π over one mm-wave wavelength. As long as the dimension of the atomic cloud is much less than the mm-wave wavelength, all atoms emit in phase, so this effect is negligible

3. The laser wave vectors in a near-resonant atomic medium can be strongly modified from their free space values, as demonstrated in slow-light EIT. This effect will not be considered here.

4. It is also important to note that the phase of the optical mode is only $e^{i\boldsymbol{k}_{780}\boldsymbol{r}}$ in a running wave cavity. In a standing wave cavity, as is used in our experiment, the coupling strengths $g_i \propto \cos(k_{780}z)$ can be decomposed into two counterpropagating modes $g_i \propto \frac{1}{2}\left(e^{ik_{780}z} + e^{-ik_{780}z}\right)$. We will not explore this in detail, but in the end we expect a 50% reduction in transduction efficiency, as only one running wave mode participates in transduction, while the other scatters strongly into free space [135].

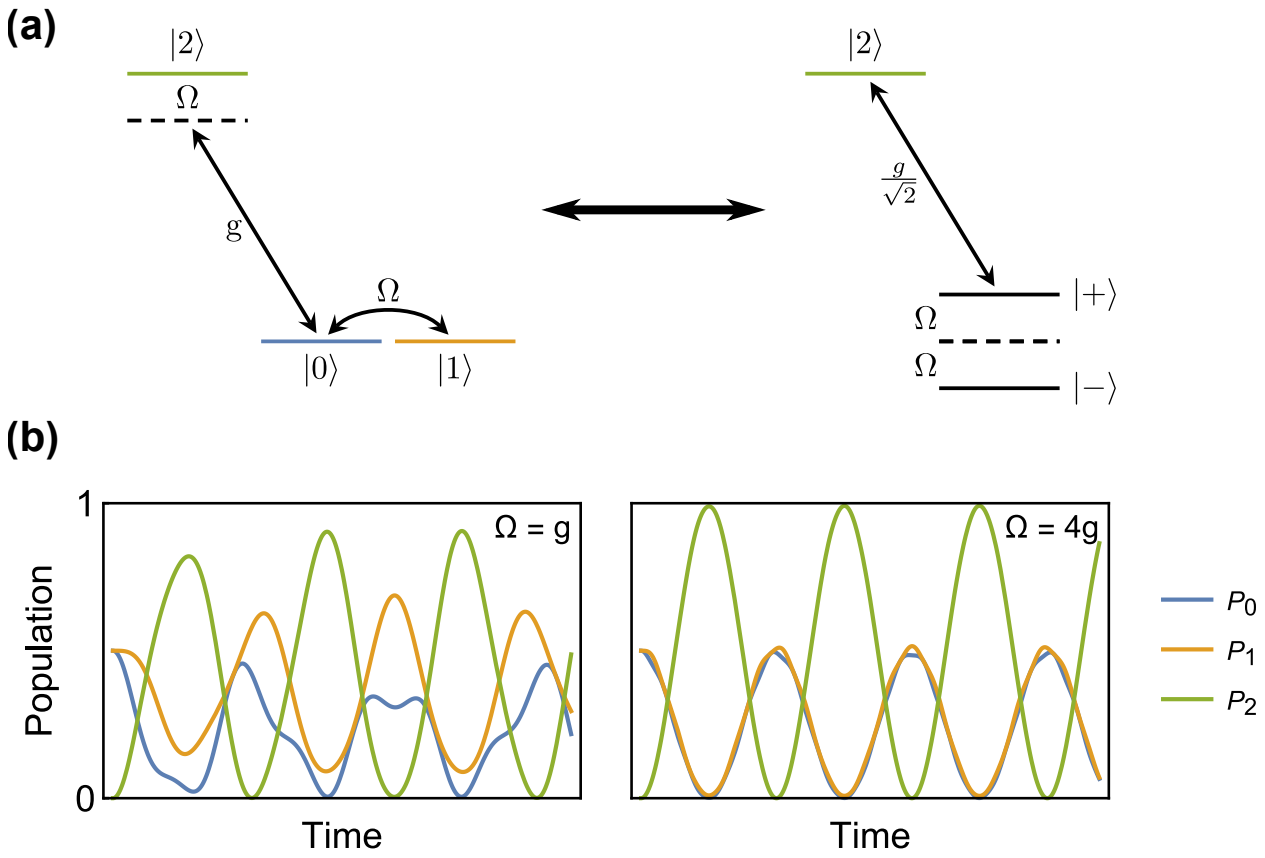

Figure 5.2: The dressed state elimination approximation used in resonant transduction, but demonstrated in a simpler three level system. (a) Change of basis from the bare atomic states to the Ω dressed states. In the bare states picture, the two ground states $|0\rangle$ and $|1\rangle$ are assumed to be at equal energies, and are coupled with Rabi frequency Ω. Only the $|0\rangle$ state is coupled to the upper state $|2\rangle$, with Rabi frequency g. In the dressed state picture, the states $|+\rangle$ and $|-\rangle$ are equal superpositions of the original ground states, and are thus each coupled to $|2\rangle$ with strength $\frac{g}{\sqrt{2}}$. However, if the detuning on the $|0\rangle \leftrightarrow |2\rangle$ coupling is Ω, then one dressed state is resonantly coupled, while the other is off-resonant. (b) Time evolution of an atom initially prepared in the dressed state $|+\rangle$. In the left panel, the dressing beam Ω is weak so that both dressed states are relevant, leading to interference in the Rabi oscillations. In the right panel, $\Omega \gg g$, and the atom oscillates between the resonantly coupled dressed state $|+\rangle$ and the upper state $|2\rangle$. The other dressed state $|-\rangle$ is irrelevant to the dynamics and can be eliminated, leaving an effective two-level system.

can be engineered by increasing the strength of the classical ultraviolet beam, or moving it closer to resonance. Indeed, a fully resonant ultraviolet beam will couple the g and f states to yield atomic dressed states $|\pm\rangle = \frac{1}{\sqrt{2}}(|g\rangle \pm |f\rangle)$. Clearly an atom prepared in $|-\rangle$ will couple to both the optical and mm-wave fields. With all atoms prepared in the $|-\rangle$ state, we would then expect an enhancement of $\frac{\sqrt{N}}{2}$ on both optical and mm-wave transitions.

However, consider what occurs when a single atom in the $|-\rangle$ state absorbs an optical cavity photon. The atom transitions to a state $\frac{1}{\sqrt{2}}(|e\rangle - |f\rangle) = \frac{1}{\sqrt{2}}\left[|e\rangle + \frac{1}{\sqrt{2}}(-|+\rangle + |-\rangle)\right]$. When the atom emits back into the cavity, it can be coupled back into either the $|-\rangle$ or $|+\rangle$ state. In fact, the cavity may so couple every atom into a superposition of $|-\rangle$ and $|+\rangle$, so that the state space expands to a size of 2^N. What's more, the two dressed states couple to the mm-wave field with opposite signs, so we expect destructive interference in the transduction process.

The situation is resolved when the two dressed states are well-separated in energy. In this case, when the system is initially prepared in one dressed state ($|-\rangle$), all couplings to the other dressed state are off-resonant, so it can be dropped from the problem. This process is shown in a simple 3-level system in Figure 5.2. Here, an atom's two ground states $|0\rangle$ and $|1\rangle$ are coupled by Rabi frequency Ω, and the atom is prepared in its $|-\rangle$ state. A separate beam couples the $|0\rangle$ state to a higher-energy $|2\rangle$ state. Even though this coupling beam has matrix elements which mix the dressed states, the off-resonant $|+\rangle$ state can be eliminated from the problem. The result is an effective two-level system, with Rabi oscillations between $|-\rangle$ and $|2\rangle$.[5]

This situation is analogous to driving the D_1 transition in rubidium with a laser, while ignoring the D_2 transition. The dipole operator only couples to the orbital angular momentum quantum number l, so one might expect it to couple the initial $J = \frac{1}{2}$ state to both the

5. In this illustration, we also choose detunings such that the dressed state $|-\rangle$ is *resonantly* coupled to the remaining state. Otherwise the atom would just stay in the initial $|-\rangle$ state instead of undergoing Rabi oscillations.

$J' = \frac{1}{2}$ and $J' = \frac{3}{2}$ states. However, due to the strong fine structure splitting (analogous to the Ω drive), it can be engineered that only one J' state is resonant with the drive.

In our transducer, elimination of one dressed state recovers the situation where we have a unique vacuum, and a small number of one-excitation states. We will treat this mathematically in the next section.

5.2.1 Elimination of Dressed State

We pass from the bare state basis to the dressed state basis by applying a unitary transformation to each atomic wavefunction [136], examining the states $|\tilde{\psi}_i\rangle = U_i^\dagger |\psi_i\rangle$. This transformation is chosen to diagonalize part of the Hamiltonian: $H_{uv} = \sum_i \left[\delta_f \hat{\sigma}^i_{ff} + \left(\Upsilon_i \hat{\sigma}^i_{fg} + h.c.\right)\right]$. The dressed states have energies

$$E^i_\pm = \frac{1}{2}\left(\delta_f \pm \sqrt{\delta_f^2 + 4\left|\Upsilon_i\right|^2}\right) \tag{5.6}$$

and take the form (for positive δ_f)

$$|+\rangle_i = \sin\frac{\theta_i}{2}|g\rangle + \cos\frac{\theta_i}{2}|f\rangle \tag{5.7}$$

$$|-\rangle_i = \cos\frac{\theta_i}{2}|g\rangle - \sin\frac{\theta_i}{2}|f\rangle \tag{5.8}$$

with

$$\tan\theta_i = \frac{2\Upsilon_i}{\delta_f} \tag{5.9}$$

The change of basis is

$$U_i^\dagger = |+\rangle_i \langle +|_i + |-\rangle_i \langle -|_i$$
$$U_i^\dagger = |+\rangle_i \left(\sin\frac{\theta_i}{2}\langle g| + \cos\frac{\theta_i}{2}\langle f|\right) + |-\rangle_i \left(\cos\frac{\theta_i}{2}\langle g| - \sin\frac{\theta_i}{2}\langle f|\right)$$

In this basis, the Hamiltonian from Equation 5.4 becomes

$$H = \delta_a \hat{a}^\dagger \hat{a} + \delta_b \hat{b}^\dagger \hat{b} + \sum_i \Big[\delta_e \hat{\sigma}^i_{ee} + \delta_r \hat{\sigma}^i_{rr} + E^i_- \hat{\sigma}^i_{--} + E^i_+ \hat{\sigma}^i_{++} + \left(g_i \cos\frac{\theta_i}{2} \hat{a}\hat{\sigma}^i_{e-} + g_i \sin\frac{\theta_i}{2} \hat{a}\hat{\sigma}^i_{e+} + h.c. \right) + \left(\Omega_i \hat{\sigma}^i_{re} + h.c. \right) + \left(-h_i \sin\frac{\theta_i}{2} \hat{b}\hat{\sigma}^i_{r-} + h_i \cos\frac{\theta_i}{2} \hat{b}\hat{\sigma}^i_{r+} + h.c. \right) \Big]$$

There are now two ground states for each atom, $|-\rangle$ and $|+\rangle$, which are superpositions of the atomic $|g\rangle$ and $|f\rangle$ states. Both states are coupled to both cavity modes. As noted before, a single photon in either cavity mode can transfer each atom between the two ground states, as can be seen by repeated application of the $\hat{H}$ operator. This leads to an accessible Hilbert space which is exponential in the atom number.

However, the ground states are split by

$$E_{\text{split}} = E_+ - E_- = \sqrt{\delta_f^2 + 4\left|\Upsilon_i\right|^2} \tag{5.10}$$

If the atoms are initially prepared in the $|-\rangle$ state, and all Rabi frequencies and loss rates are much less than this splitting, then we may neglect coupling to the $|+\rangle$ state and drop any terms containing it from the Hamiltonian.[6] This yields

$$H = \delta_a \hat{a}^\dagger \hat{a} + \delta_b \hat{b}^\dagger \hat{b} + \sum_i \Big[\delta_e \hat{\sigma}^i_{ee} + \delta_r \hat{\sigma}^i_{rr} + E^i_- \hat{\sigma}^i_{--} + \left(g_i \cos\frac{\theta_i}{2} \hat{a}\hat{\sigma}^i_{e-} + h.c. \right) + \left(\Omega_i \hat{\sigma}^i_{re} + h.c. \right) + \left(-h_i \sin\frac{\theta_i}{2} \hat{b}\hat{\sigma}^i_{r-} + h.c. \right) \Big]$$

Finally, for a cleaner form we will go into a frame where the atomic levels $-^i$, e^i, r^i (but

6. Even if the initial state preparation is imperfect and some population lies in the $|+\rangle$ state, it is possible to choose detunings such that the $|-\rangle$ state is *resonantly* coupled to e, r. In this case, the $|-\rangle$ state will participate much more strongly in the transduction process, and we still expect little influence from atoms in the $|+\rangle$ state.

not the cavity operators) rotate at E^i_-. We will also define $\overline{g}_i = g_i \cos\frac{\theta_i}{2}$, $\overline{h}_i = -h_i \sin\frac{\theta_i}{2}$. Then

$$H = \delta_a \hat{a}^\dagger \hat{a} + \delta_b \hat{b}^\dagger \hat{b} + \sum_i \Big[\delta^i_e \hat{\sigma}^i_{ee} + \delta^i_r \hat{\sigma}^i_{rr} + \Big(\overline{g}_i \hat{a} \hat{\sigma}^i_{e-} + h.c.\Big) + \Big(\Omega_i \hat{\sigma}^i_{re} + h.c.\Big) + \Big(\overline{h}_i \hat{b} \hat{\sigma}^i_{r-} + h.c.\Big)\Big] \quad (5.11)$$

where $\delta^i_e = \omega_e - E^i_- - \omega_o$, $\delta^i_r = \omega_r - E^i_- - \omega_{blue} - \omega_o$. Note that each atom may see a different light shift due to inhomogeneity of the ultraviolet laser. In the rotating frame, this yields atom-dependent δ^i_e, δ^i_r.

In summary, by eliminating one dressed state, we have obtained a unique zero-excitation vacuum state when no cavity photons are in the system,

$$|0\rangle = |0, 0, - - - \cdots\rangle \quad (5.12)$$

i.e. zero optical photons, zero mm-wave photons, and all atoms in the $|-\rangle$ state. The vacuum state couples to both optical or mm-wave cavity modes with strength $g\cos\frac{\theta}{2}$ and $-h\sin\frac{\theta}{2}$, which is useful for transduction – by changing the ultraviolet Rabi frequency and detuning, we can redistribute the coupling strength between these two transitions. In the presence of a cavity photon, the Hamiltonian couples the vacuum+photon state to a small set of other one-excitation states, i.e. those with one atom in an e or r state. This is a good starting point for applying our standard perturbation theory.

The condition for validity of this elimination was that $E_+ - E_- = \sqrt{\delta_f^2 + 4\,|\Upsilon_i|^2}$ is much greater than any Rabi frequencies or loss rates. This condition encompasses the conventional condition for adiabatic elimination of the f state (large δ_f), but also includes the case of large UV Rabi frequency, even with no detuning. We anticipate that this will allow large population of the f state and large collective enhancement of the mm-wave transition.

5.2.2 Decay of the Dressed States

Our transduction bandwidth is greatly increased by placing some of the atomic population in the lower Rydberg state. However, this state has a finite lifetime, and the atoms will eventually decay. As long as this process is slow compared to the transduction bandwidth, then many photons can be transduced before decay becomes important. Eventually, the atomic sample may need to be repumped or replenished, making this a pulsed process. Generally, as the Rydberg decay rates γ_r are much slower than any other timescales in the problem, we expect these effects to be small.

If the $g \leftrightarrow f$ transition were closed, then the steady-state density matrix of the atoms under a UV drive could be calculated with the optical Bloch equations. For example, resonant light would produce a steady state which is a 50/50 statistical mixture of g and f. In this case, the g atoms would be distinguishable from the f atoms, and we anticipate that the absorption of a transduction photon would be collectively enhanced, but the emission at the other frequency would not. In reality the transition is not closed, and atoms which decay from the f state may be shelved in other metastable states. Other experiments have still found good agreement with the steady-state optical Bloch equations for a closed transition [26]. In the worst case, we can model atoms which decay as lost (until they are repumped).

The number of atoms in the f state is $N \sin^2 \frac{\theta}{2} \equiv N_f$, and the decay rate per Rydberg atom is γ_f. Thus atoms decay at a rate $N_f \gamma_f$, and the total atomic sample is depleted at a rate $\Gamma_{\text{sample}} = \gamma_f \frac{N_f}{N}$. With 100 atoms in the f state, the collective mm-wave Rabi frequency is $h\sqrt{\alpha N} = h\sqrt{100} \approx 2$ MHz, yielding a sufficient bandwidth. If the total atom number in the cavity is $N = 1,000$, then $\alpha = 0.1$, and for $\gamma_f = 5$ kHz the sample is depleted at a rate of $\Gamma_{\text{sample}} = 500$ Hz, which is much less than the transduction bandwidth.

There is another depumping mechanism: an excited atom can off-resonantly emit a cavity photon and fall into the $|+\rangle$ state, after which the cavity photon can leave with rate κ (or κ_m). These processes occurs at a rate $P_e \left(\frac{\overline{g}\sqrt{N}}{E_{\text{split}}}\right)^2 \kappa$, where P_e is the per-atom population

of the e state, and $P_r \left(\frac{\overline{h}\sqrt{N}}{E_{\text{split}}}\right)^2 \kappa_m$, where P_r is the per-atom population of the r state. The former process is suppressed both by $\left(\frac{\overline{g}\sqrt{N}}{E_{\text{split}}}\right)^2$ and by P_e, where P_e is kept small anyway to minimize free-space scattering from the e state. The latter process is more severe, but $\frac{\overline{h}\sqrt{N}}{E_{\text{split}}}$ will still generally be very small, as we generally operate in parameter ranges where $\overline{h}\sqrt{N} \approx 1$ MHz, while $E_{\text{split}} \approx 50$ MHz. Additionally, this is the atom depletion rate; the sample depletion rate is less by a factor of N.

These couplings to the $N_+ = 1$ manifold additionally cause an AC Stark shift of our desired atomic states, which can be calculated in a similar fashion.

5.3 Transducer Performance

In this section we will derive analytical and numerical results for the expected performance of the transducer from Equation 5.11, given reasonable experimental parameters. Following the treatment of EIT from previous sections of the thesis, we can restrict to a single excitation in the system, and identify a single collective state corresponding to each atomic level. The transitions from the ground state will be enhanced so that the $- \leftrightarrow e$ coupling is $g_{coll} = \overline{g}\sqrt{N}$, and the $- \leftrightarrow f$ coupling is $h_{coll} = \overline{h}\sqrt{N}$. Actually, as we will see in the next section, collective states are only valid here in the maximally symmetric case, i.e. if *all* couplings are uniform between atoms. Such a situation can be engineered, for example, by trapping the atoms in a volume small compared to all beam waists (or depumping atoms outside this volume). Moreover, these results give useful analytical forms, and small corrections will be calculated in Section 5.5.

The one-excitation Hamiltonian can then be written in matrix form. The phase of cou-

plings can be chosen to make them real. Then

$$H = \begin{pmatrix} \delta_a - i\frac{\kappa}{2} & g_{coll} & 0 & 0 \\ g_{coll} & \delta_e - i\frac{\gamma}{2} & \Omega & 0 \\ 0 & \Omega^* & \delta_r - i\frac{\gamma_r}{2} & h_{coll} \\ 0 & 0 & h_{coll} & \delta_b - i\frac{\kappa_m}{2} \end{pmatrix} \tag{5.13}$$

with $|1,0,-\rangle = \begin{pmatrix} 1 \\ 0 \\ 0 \\ 0 \end{pmatrix}$, $|0,0,E\rangle = \begin{pmatrix} 0 \\ 1 \\ 0 \\ 0 \end{pmatrix}$, $|0,0,R\rangle = \begin{pmatrix} 0 \\ 0 \\ 1 \\ 0 \end{pmatrix}$, $|0,1,-\rangle = \begin{pmatrix} 0 \\ 0 \\ 0 \\ 1 \end{pmatrix}$.

The system begins in the vacuum state $|0\rangle$ from Equation 5.12, with each atom in a single dressed state $-$, and no optical or mm-wave photons present. The system is driven into a steady state given by $|\psi_1\rangle = \left[\hat{H}_0\right]^{-1} \hat{V}\,|0\rangle$, where the perturbation is $\hat{V} = \sqrt{\kappa}E_{\text{in}}\left(\hat{a}^\dagger + \hat{a}\right)$.[7] Then the transmitted mm-wave field amplitude to linear order is given by $t(\omega) = \sqrt{\kappa_m}\,\langle 0|\hat{b}|\psi_1\rangle$. Note we are calculating transmission from an optical input to mm-wave output, but the result is the same in the other direction.

Finally, all energies will be expressed relative to the cavity frequency ω_a, which amounts to defining variables $\delta_a \equiv -\omega$, $\delta_e \equiv \delta_{ea} - \omega$, $\delta_r \equiv \delta_{ra} - \omega$, $\delta_b \equiv \delta_{ba} - \omega$.

5.3.1 Optimal Transducer Parameters

The expression for $t(\omega)$ is easily calculated, but is messy, so it is not shown here. This expression can be used to calculate the optimum blue Rabi frequency to maximize on-resonance efficiency, setting $\left[\frac{d|t(\omega)|^2}{d\Omega}\right|_{\Omega=\Omega_{\text{opt}}} = 0$. As explained in Section 2.7.3, the optimal Ω is chosen to guarantee impedance matching. If all levels are resonant ($\delta_{ea} = \delta_{ra} = \delta_{ba} = 0$),

7. The perturbation in a non-rotating frame is $\hat{V} = \sqrt{\kappa}E_{\text{in}}\left(\hat{a}^\dagger e^{i\omega_d t} + \hat{a}e^{-i\omega_d t}\right)$, where ω_d is the frequency of the drive laser. However, recall that we have already expressed the Hamiltonian in a frame with $\hat{a}$ rotating at an arbitrary frequency ω_o. Identifying ω_o with the drive laser frequency eliminates all time dependence.

the result is

$$\Omega_{\text{opt}} = \sqrt{\eta_o + 1}\sqrt{\eta_m + 1}\sqrt{\gamma_e \gamma_r} \tag{5.14}$$

We denote the efficiency with $\Omega = \Omega_{\text{opt}}$ as $T(\omega) = \left[|t(\omega)|^2\right]_{\Omega=\Omega_{\text{opt}}}$. On resonance, this becomes

$$T(0) = \frac{\eta_o \eta_m}{(\eta_o + 1)(\eta_m + 1)} \tag{5.15}$$

Thus the on-resonance efficiency depends only on the cooperativities of the two transitions. This could have been anticipated from the less thorough calculation in Section 2.7.3.

With typical parameters, it is easy to achieve $\eta_o, \eta_m > 20$, leading to efficiencies exceeding 90%. With $g_{coll} = 15$ MHz, $\kappa = 4$ MHz, $\gamma_e = 6$ MHz, $h_{coll} = 1$ MHz, $\kappa_m = 2$ MHz, and $\gamma_r = 30$ kHz, we have $\eta_o = 38$, $\eta_m = 67$.

In the high-cooperativity regime necessary for high efficiency, the expression for Ω_{opt} simplifies to $\Omega_{\text{opt}} \approx 2\frac{g_{coll} h_{coll}}{\sqrt{\kappa \kappa_m}}$. The blue Rabi frequency scales with the optical and mm-wave Rabi frequencies, but scales inversely with the geometric mean of the cavity decay rates. Increasing the cavity linewidths decreases blue power requirements, but also decreases efficiency.

Finally, we can plot transducer efficiency as a function of frequency. Because g, h are comparable to κ, κ_m, the lineshape may not simplify to a simple Lorentzian. In Figure, we plot transducer lineshapes for several values of κ_m, showing that a full-width half max of ~ 3 MHz can be expected, limited by the collective mm-wave coupling rate of 1 MHz for our chosen parameters.

5.3.2 Off-Resonant Operation

The previous expressions were all developed for the case of all-resonant operation (except the UV transition, which had no such restrictions). Analytic formulae can be obtained for the

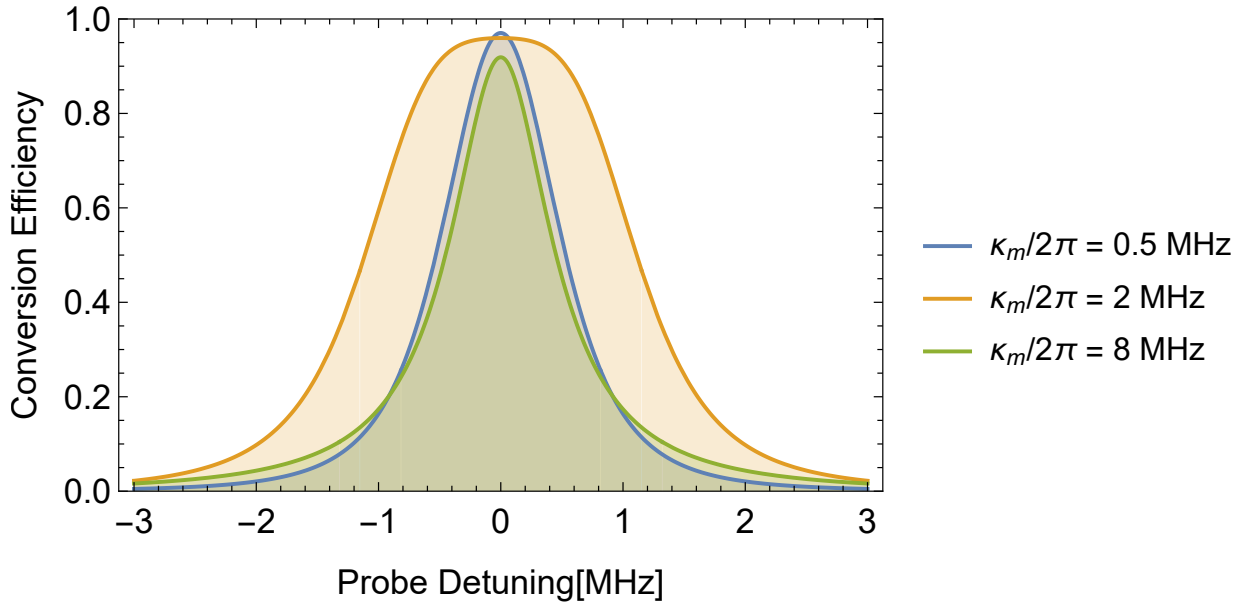

Figure 5.3: **Transducer bandwidth versus mm-wave cavity linewidth.** Parameters are $g/2\pi = 15$ MHz, $\Gamma/2\pi = 6$ MHz, $\kappa/2\pi = 4$ MHz, $h/2\pi = 1$ MHz, $\gamma_r/2\pi = 30$ kHz. Note the non-Lorentzian shape when $h \sim \kappa_m$.

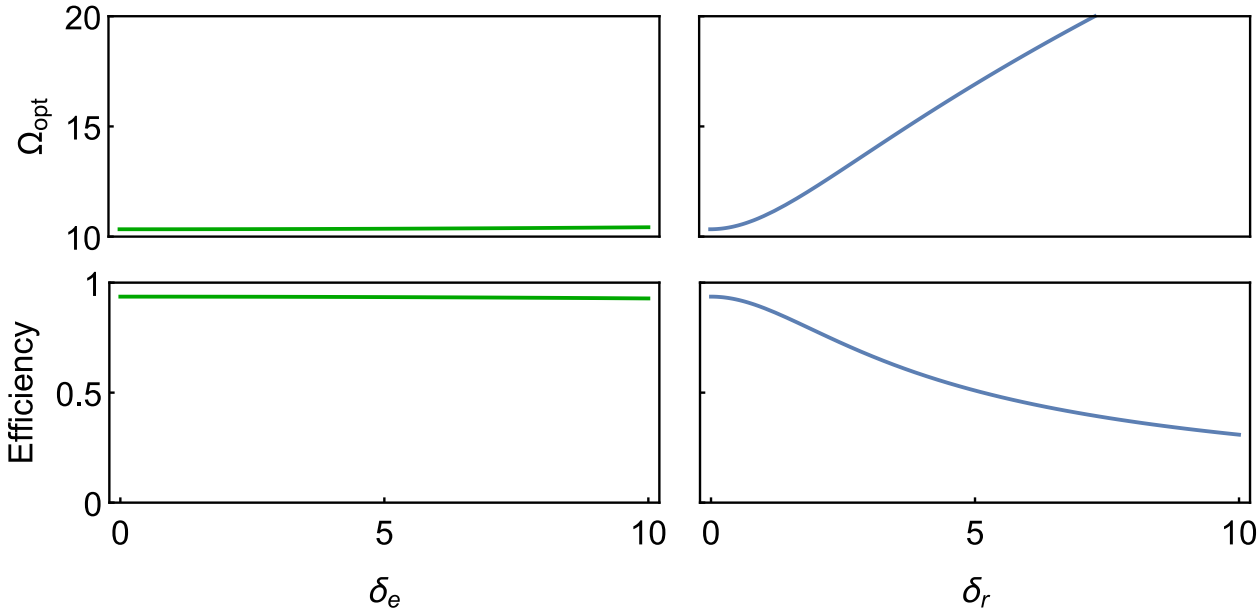

Figure 5.4: **Off-resonant transducer efficiency.** Parameters are $g/2\pi = 10$ MHz, $\Gamma = 6$ MHz, $\kappa = 4$ MHz, $h = 2$ MHz, $\gamma_r = 30$ kHz, $\kappa_m = 4$ MHz.

case of off-resonant operation. However, they are quite lengthy. In Figure 5.4, the optimal value of Ω, and the corresponding transduction efficiency, are plotted as functions of δ_e and δ_r. The blue power requirement increases, while achievable efficiency goes down: all-resonant operation (except for UV) appears to be strictly better.

The performance decreases strongly with $|\delta_r|$, but only modestly with $|\delta_e|$. This can be understood by the former breaking the approximate EIT condition, causing population of the lossy $|5P_{3/2}\rangle$ state.

5.4 Transducer Collective States

In previous chapters we have seen that a resonator coupled to an atomic ensemble can be described nearly exactly by considering just a few collective atomic states and their coupling rates to the light fields, rather than keeping track of the entire atomic ensemble. This simplification worked even when atoms had non-uniform couplings to the resonator, so long as they coupled uniformly to all other beams.

In the case of the transducer, however, it is generally insufficient to consider a single collective number and collective coupling rate for each transition. We may see a problem by calculating the collective states directly. As before, we can begin with all atoms in the ground state, and apply the part of the Hamiltonian corresponding to optical excitation. This results in a state

$$|E\rangle = \frac{1}{g_{coll}} \sum_i g_i \hat{\sigma}^i_{eg}$$

However, we could also have applied the UV excitation, then the mm-wave excitation, then the classical 480 nm coupling parts of the Hamiltonian. If all of these couplings are uniform, the collective state is

$$|\tilde{E}\rangle = \frac{1}{\sqrt{N}} \sum_i \hat{\sigma}^i_{eg}$$

Excitation via these two path ways does not commute, and there are generally multiple

UV excitations present in the system at a given time. The end result is that the collective states no longer provide a clear solution to the Hamiltonian. One exception is the maximally symmetric case, when all atomic couplings are equal on all transitions, in which case the usual collective state procedure can be followed.

Previous work [134] has observed that inhomogeneous couplings could induce an additional loss mechanism for the converter, and suggested working far off-resonance as a solution. The worry is that atoms are far from the waist of the optical mode are still coupled to the mm-wave mode and UV laser. These atoms will absorb mm-wave photons and be coupled by the blue beam to the lossy $|5P_{3/2}\rangle$state, scattering into free space and losing the mm-wave photons. In the next section, we will introduce a method to calculate the transduction efficiency with all atoms considered, and find that in reality this effect is small.

5.5 Transducer with Non-Uniform Couplings

We have a Hamiltonian which has a unique zero-excitation state, instead of the 2^N possible combinations of atoms in the g and f states. From here we would like to reduce the problem to a linear one by following the prescription from previous chapters: identify 3 or 4 collective states which constitute a complete set of accessible one-excitation states, and use first-order non-Hermitian perturbation theory to compute transmission from mm-wave to optical. Unfortunately, as we have seen, there are no privileged collective states in most circumstances – all one-excitation states must be considered.

Still, there are only $2N+2$ one-excitation states: an optical photon, a microwave photon, one of N atoms in the e state, or one of N atoms in the r state. We can still restrict to this manifold and apply first-order non-Hermitian perturbation theory to calculate the transmission spectrum. The resulting $(2N+2) \times (2N+2)$ matrix could be solved with a full matrix inversion. However, it turns out that the sparsity of this matrix can be used to calculate the transmission in closed-form, without any matrix inversion. This will allow

efficient computation of transduction efficiency even in the presence of non-uniform couplings.

We begin with the vacuum state $|0\rangle$ from Equation 5.12, with each atom in a single dressed state $-$, and no optical or mm-wave photons present. The system is driven into a steady state given by $|\psi_1\rangle = -\left[\hat{H}_0\right]^{-1}\hat{V}\,|0\rangle$, where the perturbation is $\hat{V} = \sqrt{\kappa}\xi\left(\hat{a}^\dagger + \hat{a}\right)$.Then the transmitted mm-wave field amplitude to linear order is given by $t(\omega) = \sqrt{\kappa_m}\,\langle 0|\hat{b}|\psi_1\rangle$. Note we are calculating transmission from an optical input to mm-wave output, but the result is the same in the other direction.

The Hamiltonian from Equation 5.11 is rewritten to include loss terms:

$$H = \Delta_a\hat{a}^\dagger\hat{a} + \Delta_b\hat{b}^\dagger\hat{b} + \sum_i\Big[\Delta_e^i\hat{\sigma}_{ee}^i + \Delta_r^i\hat{\sigma}_{rr}^i + \left(\overline{g}_i\hat{a}\hat{\sigma}_{e-}^i + h.c.\right) + \left(\Omega_i\hat{\sigma}_{re}^i + h.c.\right) + \left(\overline{h}_i\hat{b}\hat{\sigma}_{r-}^i + h.c.\right)\Big] \quad (5.16)$$

where the detunings are loss rates are combined into $\Delta_e^i = \delta_e^i - i\frac{\gamma_e}{2}$.

We write $|\psi_1\rangle$ in a basis of single-excitation states:

$$|\psi_1\rangle = \left[A_a a^\dagger + \sum_i\left(A_e^i\sigma_i^{eg} + A_r^i\sigma_i^{rg}\right) + A_b b^\dagger\right]|0\rangle \quad (5.17)$$

The previous equation for determining $|\psi_1\rangle$ is rewritten as:

$$H_0\,|\psi_1\rangle = \sqrt{\kappa}E_{in}\hat{a}^\dagger\,|0\rangle \quad (5.18)$$

This yields a system of linear equations

$$\sqrt{\kappa}E_{in} = \Delta_a A_a + \sum_i \overline{g}_i^* A_e^i \tag{5.19}$$

$$0 = \overline{g}_i A_a + \Delta_e^i A_e^i + \Omega_i^* A_r^i \tag{5.20}$$

$$0 = \Omega_i A_e^i + \Delta_r^i A_r^i + \overline{h}_i A_b \tag{5.21}$$

$$0 = \sum_i \overline{h}_i^* A_r^i + \Delta_b A_b \tag{5.22}$$

We may use the two middle equations to eliminate A_e^i and A_r^i in terms of A_a and A_b. Substituting these values into the first and last equations will then leave two equations for the optical cavity and mm-wave cavity amplitudes. Elimination yields

$$A_e^i = \frac{-\overline{g}_i \Delta_r^i A_a + \Omega_i^* \overline{h}_i A_b}{\Delta_e^i \Delta_r^i - |\Omega_i|^2} \tag{5.23}$$

$$A_r^i = \frac{-\overline{h}_i \Delta_e^i A_b + \Omega_i \overline{g}_i A_a}{\Delta_e^i \Delta_r^i - |\Omega_i|^2} \tag{5.24}$$

Finally, substituting this into the two cavity mode equations:

$$\sqrt{\kappa}E_{in} = \left(\Delta_a - \sum_i \frac{|\overline{g}_i|^2 \Delta_r^i}{\Delta_e^i \Delta_r^i - |\Omega_i|^2}\right) A_a + \left(\sum_i \frac{\overline{g}_i^* \Omega_i^* \overline{h}_i}{\Delta_e^i \Delta_r^i - |\Omega_i|^2}\right) A_b \tag{5.25}$$

$$0 = \left(\Delta_b - \sum_i \frac{|\overline{h}_i|^2 \Delta_e^i}{\Delta_e^i \Delta_r^i - |\Omega_i|^2}\right) A_b + \left(\sum_i \frac{\overline{h}_i^* \Omega_i \overline{g}_i}{\Delta_e^i \Delta_r^i - |\Omega_i|^2}\right) A_a \tag{5.26}$$

These two equations can be easily solved for A_a, A_b. Then the transducer transmission is $t(\omega) = \sqrt{\kappa_m} A_b$.

A similar method can be used to calculate closed-form EIT transmission spectra and, with a litle more complication, g_2 statistics in systems with interacting Rydberg polaritons (see the supplement of Reference [137])

5.5.1 Elimination of Atomic Degrees of Freedom

Equations 5.25 resemble input-output equations for the two cavity fields.[8] We may wish to find a simple Hamiltonian containing only cavity operators which yields these input-output equations. However, the terms $\Delta_e^i = \omega_e - E_-^i - \omega_o - i\frac{\gamma_e}{2}$ and Δ_r^i contain the input/output frequencies ω_o and ω_m, which makes this difficult.

If all atomic states are far detuned, then $\omega_e - E_-^i - \omega_o$ is approximately constant as ω_o is swept over the bandwidth of the converter, and it is also much larger than $\frac{\gamma_e}{2}$. In this case we may approximate the detunings as real constants, $\Delta_e^i \approx \delta_{e0}^i$, $\Delta_r^i \approx \delta_{r0}^i$. The equations simplify to

$$\sqrt{\kappa}E_{in} = \left(-i\frac{\kappa}{2} + \omega_a - \beta_a - \omega_o\right) A_a + SA_b \tag{5.27}$$

$$0 = \left(-i\frac{\kappa_m}{2} + \omega_b - \beta_b - \omega_m\right) A_b + S^* A_a \tag{5.28}$$

with constants

$$S = \sum_i \frac{\overline{g}_i^* \Omega_i^* \overline{h}_i}{\delta_{e0}^i \delta_{r0}^i - |\Omega_i|^2} \tag{5.29}$$

$$\beta_a = \sum_i \frac{|\overline{g}_i|^2 \delta_{r0}^i}{\delta_{e0}^i \delta_{r0}^i - |\Omega_i|^2} \tag{5.30}$$

$$\beta_b = \sum_i \frac{|\overline{h}_i|^2 \delta_{e0}^i}{\delta_{e0}^i \delta_{r0}^i - |\Omega_i|^2} \tag{5.31}$$

These input-output equations are generated by a Hamiltonian

$$H_{adiabatic} = (\omega_a - \beta_a)\,\hat{a}^\dagger \hat{a} + (\omega_b - \beta_b)\,\hat{b}^\dagger \hat{b} + \left(S\hat{a}^\dagger \hat{b} + S^* \hat{b}^\dagger \hat{a}\right) \tag{5.32}$$

8. Of course, these equations involve amplitudes A_a, A_b, instead of operators $\hat{a}$, $\hat{b}$. In the one-excitation manifold, operators and amplitudes are interchangeable – for a wavefunction in the form of Equation 5.17, we have $\hat{a}\,|\psi_1\rangle = A_a$. The Hamiltonian we will obtain by replacing the amplitudes with operators will only be correct to first order. However, if the full system can be regarded as nearly linear, then it becomes exact.

Note that this equation is valid even for a near-resonant ultraviolet beam. For far-detuned UV, we identify $\cos\frac{\theta_i}{2} \approx 1$, $\sin\frac{\theta_i}{2} \approx \frac{\Upsilon_i}{\delta_f}$. Then neglecting terms in $\frac{|\Omega_i|^2}{\delta^i_{e0}\delta^i_{r0}}$ and ignoring the frequency pulling terms β_a, β_b yields exactly the Hamiltonian obtained by adiabatic elimination in References [134, 24].

5.6 Conclusion

A major argument for microwave (or mm-wave) to optical conversion is that optical photons can be transmitted over great distances through room temperature fiber optics, while preserving their quantum state. The optical wavelength most convenient for interfacing with rubidium, 780 nm, can have an attenuation as low as $\sim$ 3 dB/km in optical fibers, limited by Rayleigh scattering. While a better option than cryogenic mm-wave links, this would require quantum repeaters at kilometer or sub-kilometer intervals to transmit over larger distances [15]. At ideal telecom wavelengths around 1560 nm, losses can be below 0.2 dB/km [138]. Other atoms such as ytterbium have convenient transitions at these wavelengths [24]. The techniques described in this chapter are broadly applicable to other atomic species.

CHAPTER 6

TUNABLE FINESSE AND MODE CONVERSION

This chapter is based on Reference [139].

High fidelity mode conversion and sorting are crucial tasks for quantum communication [140, 141], as well as high-bandwidth mode-division multiplexed classical communication [142]. At the transmitting end of a communication network, mode conversion enables the encoding of information into the transverse spatial degrees of freedom of an optical field or fiber, thereby substantially increasing the bit-rate. At the receiving end, mode-sorting enables decoding of the previously encoded spatial information. While both mode conversion and sorting are fundamentally *linear* in the electromagnetic field, they are technically challenging because the necessary linear transformations are not generically quadratic in the transverse spatial coordinates and as such cannot be directly implemented with standard optics like mirrors, lenses, and beam splitters.

At moderate efficiency, "mode shaping" can be achieved with a single phase plate [143, 144] or digital micromirror device [145] that redirects a fraction of an incident optical field into a diffracted target mode. Near-unity efficiency requires implementing a unitary transformation of *all* of the incident mode to the target mode. In the special case of Hermite-Gauss $\leftrightarrow$ Laguerre-Gauss interconversion, this unitary transformation can be realized via a pair of astigmatic lenses [146], since HG and LG modes are related to one another by only the relative phase of horizontal and vertical mode excitations. More general approaches to high fidelity mode-converting unitaries include numerically optimized nanostructured couplers between waveguides [147, 148]; adiabatically varying coupling between macroscopic optical fibers [149]; conformal beam transformations implemented in two or more holographic phase gratings [150, 151, 152]; meshes of Mach-Zehnder interferometers [153, 154]; and long period fiber gratings [155].

Implementing an arbitrary mode converter is formally equivalent to changing one quan-

tum mechanical wave-function into another using only *spatially local* potentials which cannot *themselves* redistribute probability in space, but can impose phase gradients that result in such redistribution under the influence of a kinetic energy term. While lenses and mirrors can impart spatially varying phase profiles onto an incident optical field, it is the subsequent diffraction that must redistribute intensity; reshaping the mode via attenuation would irreversibly reduce the conversion efficiency. To our knowledge, prior work fits predominantly into three paradigms: adiabatically varying the system Hamiltonian such that an input mode/initial eigenstate is smoothly converted into the desired output mode/final eigenstate (as in coupled fibers); bang-bang unitaries that, in discrete steps separated by free evolution/diffraction, convert between input and output modes (as in cascaded diffraction gratings and long-period fiber gratings); or something in-between that implements a "shortcut to adiabaticity" [156].

In this work we explore a fourth paradigm relying on impedance mismatches between optical cavities to achieve near-unity efficiency mode conversion [157] without nanophotonics or non-quadratic optics. Using only lenses and mirrors, we demonstrate conversion of an HG_{00} mode into an arbitrary target HG_{m0} mode by simply varying the length of a Fabry-Pérot resonator over a few nanometers. The large propagation distances required for other approaches are realized in our work by repeated round trips through the structure of the coupled cavities. Related ideas [158, 159] in a nanofabricated setup allow mode conversion in a ring resonator coupled to a multimode waveguide, with mode-dependent phase matching providing mode selectivity; that approach affords $\sim 5\%$ bidirectional conversion, as fabrication imperfections limit the (fine-tuned during fabrication) impedance match, and fiber-to-chip coupling induces losses. Indeed, resonant impedance matching between cavities has enabled efficient coupling of a Y-junction to a waveguide [160] without any mode control. In our work, coupled macroscopic resonators enable rapidly tunable impedance matching to arbitrary modes and remove the need to couple to a chip.

In Section 6.1 we introduce the simpler problem of coupled, impedance-mismatched Fabry-Pérot cavities in the *single-mode* limit. Here the result is a cavity of tunable finesse $\mathcal{F}$. We experimentally demonstrate such finesse tunability over a decade. In Section 6.3 we consider the full problem of coupled, misaligned *multimode* Fabry-Pérot cavities, where the resulting behaviour corresponds to an optical mode converter. Implementing these ideas, we demonstrate optical conversion efficiency $>75\%$ for the first 6 Hermite-Gauss modes, limited by mirror loss. In Section 6.4 we explore applications of these tools.

6.1 Tunable Finesse Cavity

We begin by analyzing two single-mode Fabry-Pérot cavities coupled through a shared mirror, as shown in Fig. 6.1a. We will find that this arrangement acts as a tunable finesse cavity— it traps light for a short duration (low finesse) or a long duration (high finesse). The two cavities have identical waists and share a mutual axis to avoid inter-mode coupling.

The total optical transmission of this arrangement can be calculated in the S-matrix formalism (see Supplement 1) in terms of the lengths of the two cavities, the wavenumber k of incident light, and the power reflection and transmission coefficients of the mirrors M_1, M_2, and M_3. A more intuitive understanding arises by observing that any single-mode scattering element is fully described by its (frequency $\delta \equiv 2kL$ dependent) reflection and transmission coefficients. It is thus valid to combine mirrors M_2 and M_3 with the propagation distance L between them, into a single composite "effective mirror" M_{23} with reflection and transmission coefficients $r_{23}(\delta)$, $t_{23}(\delta)$ (Fig. 6.1a, inset).

In this picture, what remains is the simple two-mirror "primary" cavity defined by the separation between M_1 and M_{23}. The total transmission of the primary cavity is thus precisely that of a simple two-mirror Fabry-Pérot with a frequency-dependent reflection coefficient for one end-mirror. The finesse of the primary cavity can be computed [162] as $\mathcal{F} \approx \frac{2\pi}{T_1+T_{23}+X_1+X_{23}}$ so long as the properties of M_{23} remain $\sim$ constant across said

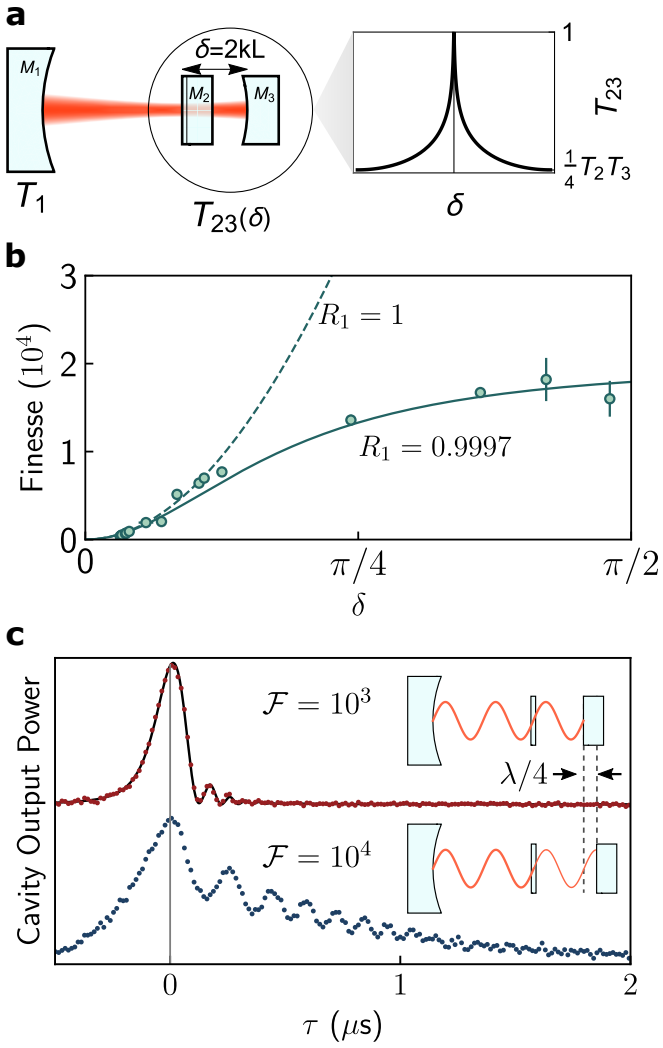

Figure 6.1: **Tunable finesse optical cavity**. **a,** Schematic of two coupled single-mode cavities. Mirrors M_2 and M_3 act as a single "effective mirror" M_{23} with frequency-dependent transmission $T_{23}(\delta)$, where $\delta \equiv 2kL$ is the round-trip propagation phase in M_{23}. Sub-λ variations in the M_2-M_3 separation change their joint transmission, and thereby the finesse $\mathcal{F}$ of the composite M_1-M_{23} cavity. T_{23} varies from unity at resonance to $\frac{1}{4}T_2T_3$ between resonances (T_i is the power transmission of mirror i). **b,** Measured $\mathcal{F}$ of the M_1-M_{23} cavity as a function of the round-trip optical phase δ in M_{23}, obtained from cavity ringdowns (for high $\mathcal{F}$) and transmission spectra (for lowest $\mathcal{F}$). The solid line is theory from measured mirror reflectances, limited by the reflectance ($R_1 = 0.9997(1)$) of M_1 ($R_1 = 1$ shown dashed). Error bars represent 1 s.d. **c,** Typical low- and high-$\mathcal{F}$ ringdown measurements with representative exp-erfc fit [161] (black line). Top inset: the cavities are mutually resonant (support an integer number of half wavelengths $\lambda/2$) for low $\mathcal{F}$. Bottom inset: displacing M_3 by a $\lambda/4$ detunes M_{23}, reducing its transmission and achieving high $\mathcal{F}$.

resonance. Here T_1 and T_{23} are power transmission coefficients and X_1, X_{23} are power loss coefficients. As T_{23} is tuned, the finesse $\mathcal{F}$ varies. Since T_{23} is simply the transmission of the Fabry-Pérot consisting of M_2 and M_3, it can range from unity to near zero as the length L tunes the cavity from resonance to anti-resonance, thereby varying $\mathcal{F}$ from small to large values.

Harnessing these principles, we construct a tunable finesse cavity using mirrors with reflectances $R_1 = 0.9997(1)$ and $R_2 = R_3 = 0.990(2)$ for 780 nm light. The finesse is tuned by varying M_{23}'s length with a piezoelectric actuator, and is then measured either spectroscopically or by cavity ringdown [161] (Fig. 6.1c). The computed transmission of M_{23}, T_{23} is shown in the black curve of Fig. 6.1a, varying from unity on resonance to $\frac{1}{4}T_2T_3 \approx 2.5 \times 10^{-5}$ at maximum detuning. The measured finesse (Fig. 6.1b) is in close agreement with a parameter-free theory (solid curve).

The finesse saturates at $1.7(2) \times 10^4$, limited by the reflectance of M_1, and is compared to theory for a perfect M_1 ($R_1 = 1$) in the dotted curve of Fig. 6.1b. From there, the next bound on finesse is set by the minimum transmission of the variable reflector, $\mathcal{F}_{\max} = \frac{8\pi}{T_2T_3} \approx 2.5 \times 10^5$ for $R_2 = R_3 = 0.99$. In practice, we anticipate an ultimate finesse limit set by scattering and absorption losses of the mirror coatings, akin to a conventional Fabry-Pérot cavity (see Supplement 1). Losses from the M_2 substrate and M_3 coating are strongly suppressed in high-finesse configurations, where very little power resides within M_{23}. A single-pass substrate loss of 1% (0.1%) only limits $\mathcal{F} \leq 1 \times 10^5$ (2×10^5), which improves further with higher R_2, R_3. Furthermore, fused-silica glass can exhibit loss < 1 ppm/cm [163], obviating this limitation.

When the detuning between the cavities is smaller than the linewidth of the secondary cavity, the above picture breaks down, because (a) the M_{23} transmission T_{23} becomes strongly frequency dependent, or equivalently (b) there is an avoided crossing between the two coupled cavity modes. In practice, this limits the round-trip loss of the primary cavity

$L_{rt} < T_1 + T_3$.

6.2 Impedance Matching Physical Picture

The mode converter presented in the next section relies on multimode impedance matching. This is analogous to impedance matching in a single-mode cavity: at resonance, a two-mirror, single-mode cavity with equal in- and out- coupling $T_1 = T_2$ transmits all light. This is a somewhat surprising result: a single mirror may be highly reflective, but two together, separated by an integer number of wavelengths, is 100% transmissive.

In the lossless case, impedance matching ensures 100% transmission. More generally, we say a system is impedance matched when there is zero reflection.

To understand this phenomenon, consider the reflection from a single-mode optical cavity where the input mirror has field reflection coefficient r_1 and is assumed to be lossless. The cavity reflection is given by the well-known formula [162]

$$S_{11} = \frac{1}{r_1} \frac{r_1^2 - g_{rt}}{1 - g_{rt}}$$

where g_{rt} is the round trip gain including reflection from all mirrors, and a phase factor. The reflection goes to zero when $r_1 = \frac{g_{rt}}{r_1}$. Clearly the phase factor of g_{rt} must be zero, i.e. the cavity is resonant. Squaring both sides, impedance matching requires

$$R_1 = G \tag{6.1}$$

where $G \equiv \frac{g_{rt}^2}{R_1}$ is the round trip power gain of all components *except* the input mirror.

This is a general condition for impedance matching with lossless input mirror. More insight can be gained in the high-finesse case, where all reflectances are nearly 1 and $R_i = 1 - T_i$, $T_i \ll 1$. Then G is a product of small losses, $G = \prod_{i \neq 1} (1 - L_i) \approx \sum_{i \neq 1} L_i$, and the sum is again over all losses besides the input mirror, including transmission through

non-input mirrors. The high-finesse impedance matching condition becomes

$$T_1 = \sum_{i \neq 1} L_i \tag{6.2}$$

In the high-finesse case the circulating power at any point in the resonator is approximately constant – the loss throughout a round trip is negligible – and we can describe the cavity's state with a single amplitude a.

Finally, the condition in Equation 6.2 can be easily understood by energy conservation. Energy conservation implies $P_{in} = P_{lost}$. The power lost is $P_{lost} = |a|^2 \sum_{i \neq 1} L_i$. Here the sum excludes transmission through the input mirror because, by construction, there is zero reflection, i.e. no power leaving from the input mirror.

To obtain Equation 6.2, we would then like to say that $P_{in} = |a|^2 T_1$. This is not immediately obvious. However, consider the time-reversed case[1]. Then the power leaving mirror 1 is clearly equal to $|a|^2 T_1$. So in the un-time reversed case, we must have $P_{in} = |a|^2 T_1$, and our statement of energy conservation implies the impedance matching condition.

This completes the rigorous explanation for the standard high-finesse impedance matching condition, $T_1 = \sum_{i \neq 1} L_i$. For very low-finesse cavities, Equation 6.1 is more correct. The two are identical for two-mirror cavities (with lossless input mirror).

6.3 Mode Converter

Coupled optical cavities, as shown in Fig. 6.2a, enable near-unity efficiency mode conversion by a multimode generalization of single-mode impedance matching: at resonance, a two-mirror, single-mode cavity with equal in- and out- coupling $T_1 = T_2$ transmits all light. The two coupled resonators explored in the prior section can be understood as one single-

1. The time reversal argument is easier if there are no losses (only transmission through mirrors) in the cavity. Otherwise, in the time reversed case the lossy elements have to be generating light. We can imagine this occurs by sources inside those elements.

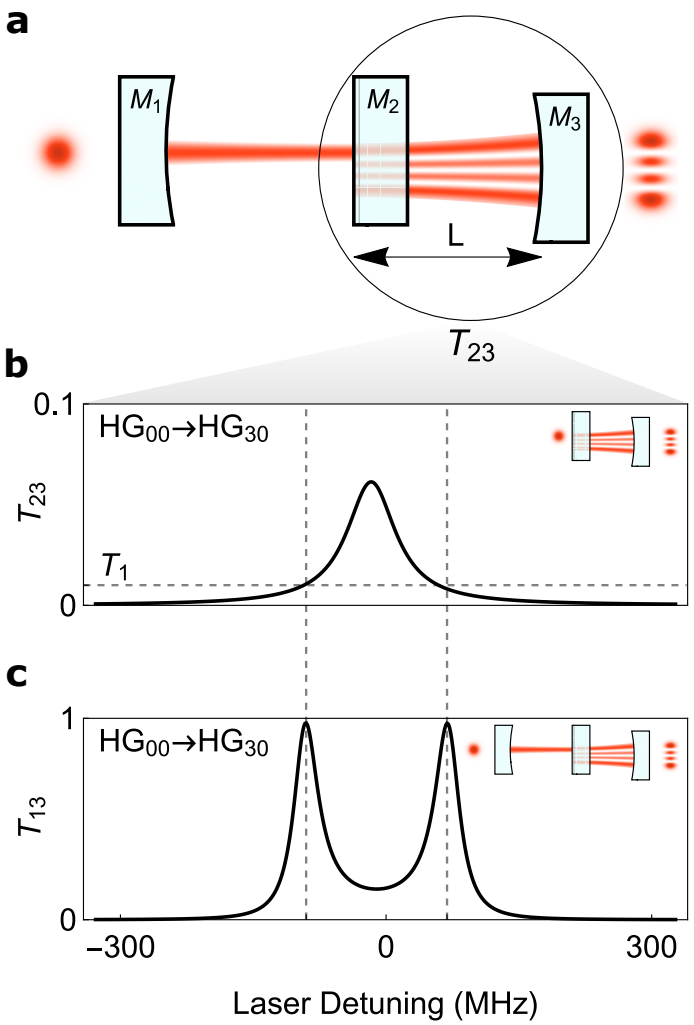

Figure 6.2: **Principle of Cavity Optical Mode Conversion**. **a,** Two coupled Fabry-Pérot resonators can act as an optical mode converter when a small transverse offset is introduced between their axes to couple their otherwise-orthogonal transverse modes. Mirrors M_2 and M_3 act as a single "effective mirror" M_{23} with frequency- and mode- dependent transmission $T_{23}^{i\leftrightarrow j}$, for input/output modes $\mathrm{HG}_{i/j,0}$. Near-unity efficiency $i \leftrightarrow j$ mode conversion through the full system M_1+M_{23} is achieved when the input- and output- couplings to the composite cavity M_1/M_{23} are equal, $T_1 = T_{23}^{i\leftrightarrow j}$ (the "impedance matching" condition), and no light leaks out through other modes. **b,** Simulated transmission of the effective mirror M_{23} (in the absence of M_1), with a translated $\mathrm{HG}_{0,0}$ input generating an $\mathrm{HG}_{3,0}$ output. The transmission $T_{23}^{0\leftrightarrow 3}$ is limited by the (translated) 0/3 mode overlap of $\approx 6\%$, and the dashed horizontal line denotes T_1. The frequency dependence of the transmission guarantees that there are two frequencies where $T_1 = T_{23}^{0\leftrightarrow 3}$ (dashed vertical lines), resulting in perfect mode conversion at these frequencies once mirror M_1 is introduced, as shown in **c**.

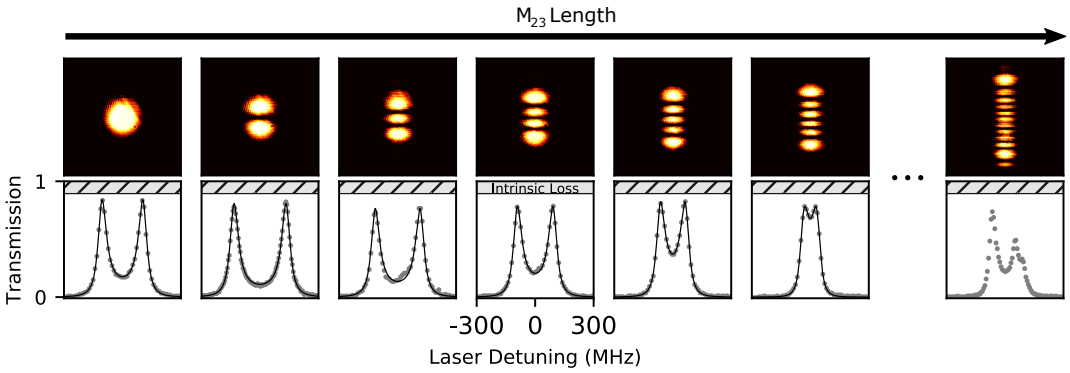

Figure 6.3: **Demonstration of High-Efficiency Mode Conversion**. An input HG_{00} mode may be coherently converted into any higher order HG_{m0} mode by using two coupled, transversely offset Fabry-Pérot cavities. The output spatial profile (top) and end-to-end conversion efficiency (bottom) are plotted for output modes HG_{00}...HG_{50} and $HG_{10,0}$. As the length of output cavity M_{23} is tuned with a piezoelectric actuator, its higher-order modes are individually brought near resonance with the drive laser. Each resonant mode of the M_{23} cavity satisfies the impedance matching condition at two laser frequencies (Fig. 6.2), giving two peaks with near-unity efficiency mode conversion. In each panel the laser frequency is swept by ± 300 MHz around the mutual resonance, demonstrating a mode-conversion bandwidth of ~ 50 MHz. Mirror absorption and scattering limits the maximum conversion efficiency (hashed region). Optical power may be diverted into other accidentally degenerate modes, distorting the output mode and spectrum (right-most panel). Model fits (solid lines) are consistent with a transverse offset between cavities of 1.30(1) waists.

mode cavity with input coupling T_1 and (frequency-dependent) output coupling $T_{23}(\omega)$ of the composite mirror M_{23}. Unity transmission again occurs when in- and out- couplings are equal, $T_1 = T_{23}(\omega)$. Because T_{23} exhibits a resonance peak whose center frequency can be tuned by adjusting the length L between M_2 and M_3, it is always possible to satisfy the impedance matching condition for a given drive frequency $\omega = \omega_d$.

In the absence of transverse mode coupling, an input $HG_m \equiv HG_{m0}$ mode produces an output HG_m mode, and the single-mode analysis applies. Introducing a transverse offset between the coupled cavities breaks orthogonality between their higher-order modes and generates inter-mode couplings (Fig. 6.2a). In this case, the HG_0 mode of the primary cavity appears displaced on M_{23}, and thus has non-zero overlap with all modes of M_{23}. As such, M_{23} now exhibits frequency- and *mode*- dependent transmission $T_{23}^{i\leftrightarrow j}(\omega) = \left|\alpha_{ij}\right|^2 T_{23}^{j}(\omega)$,

with input and output modes i and j having an overlap integral α_{ij}. The transverse modes of M_{23} each have their own transmission function $T_{23}^{j}(\omega)$, all with identical linewidths, but different resonant frequencies due to the round-trip Gouy phase of M_{23} [162]. The simulated $\mathrm{HG}_0 \rightarrow \mathrm{HG}_3$ transmission peak is shown in Fig. 6.2b.

We expect unity transmission to occur when $T_1 = T_{23}^{i \leftrightarrow j}(\omega_d)$, where in-coupling occurs through the HG_i mode at M_1, and out-coupling occurs through the HG_j mode of M_{23}. The multimode S-Matrix calculation shown in Fig. 6.2c (and detailed in the Supplement) supports this intuition, showing nearly 100% conversion efficiency. As the length of M_{23}, L, is tuned, its higher order modes individually approach resonance with the drive laser and primary cavity, satisfying the impedance matching condition at two drive-laser frequencies and thus permitting conversion of any input mode i into any output so long as $\left|\alpha_{ij}\right|^2 > T_1$. Indeed, for the theory in Fig. 6.2, the mode overlap between HG_0 and HG_3 is only $\sim 6\%$, but near-unity conversion still occurs.

To demonstrate these principles, we construct a mode converter using mirrors with reflectances $R_1 = R_3 = 0.965(5)$, $R_2 = 0.972(1)$ at 780 nm, whose performance is shown in Fig. 6.3. In each panel, the laser frequency is scanned to satisfy the resonance condition. Between panels, the length L of M_{23} is varied with a piezoelectric actuator to bring the target mode to resonance with the HG_0 mode of the primary cavity. The transmission is monitored on a large-area photodiode to determine conversion efficiency, and on a CCD camera to ascertain mode shape. With the cavities transversely offset by $\sim$1 waist, HG_0 through HG_5 were generated with total conversion/transmission in excess of 75%. To access higher order modes, the offset was increased to $\sim$2.5 waists, yielding conversion of modes up to HG_{12}; the HG_{10} mode is shown with 75% total transmission.

6.4 Outlook

We have presented a new framework for understanding coupled multimode optical resonators, where one resonator acts as a frequency- and mode- dependent mirror for the other resonator. Harnessing this new perspective, we demonstrate both a variable finesse cavity and an arbitrary spatial mode converter. By introducing an intracavity electro-optic modulator [164], we anticipate rapid tunability of finesse and output mode, enabling control of photon dynamics within a cavity lifetime.

In our approach, the mode conversion bandwidth is set by the cavity linewidth, and so can be increased by scaling down to micro-resonators. Working with small ROC fiber Fabry-Pérots [92] should enable bandwidths up to ∼10 GHz, and extending these ideas to nanophotonic platforms would allow further bandwidth gains [165, 147]. Meanwhile, superpolished mirrors with loss < 3 ppm [166] should enable efficiency up to 99%, limited by leakage into undesired modes. The mode converter is inherently bidirectional and can thus convert $TEM_{m0} \rightarrow TEM_{00}$.

The techniques introduced in this work can be employed to interconvert between field profiles of *any* physical system in which coupled resonators can be realized whose eigenmodes are the desired input and output field profiles. Coupling to a twisted optical resonator [167] whose eigenmodes are Laguerre-Gauss (LG) would enable high-efficiency generation of optical orbital angular momentum states for optical communication. Similarly, the use of astigmagtic cavities would allow control over both mode indices of the HG_{mn} output. Indeed, these concepts transcend even light: by coupling together phononic resonators with disparate mode structures, it should be possible to deterministically and efficiently reshape acoustic waves [168].

REFERENCES

[1] Iulia M Georgescu, Sahel Ashhab, and Franco Nori. Quantum simulation. *Reviews of Modern Physics*, 86(1):153, 2014.

[2] Stuart J Freedman and John F Clauser. Experimental test of local hidden-variable theories. *Physical Review Letters*, 28(14):938, 1972.

[3] Robert Jördens, Niels Strohmaier, Kenneth Günter, Henning Moritz, and Tilman Esslinger. A mott insulator of fermionic atoms in an optical lattice. *Nature*, 455(7210):204–207, 2008.

[4] Chen-Lung Hung, Xibo Zhang, Nathan Gemelke, and Cheng Chin. Observation of scale invariance and universality in two-dimensional bose gases. *Nature*, 470(7333):236–239, 2011.

[5] Waseem S Bakr, Amy Peng, M Eric Tai, Ruichao Ma, Jonathan Simon, Jonathon I Gillen, Simon Foelling, Lode Pollet, and Markus Greiner. Probing the superfluid–to–mott insulator transition at the single-atom level. *Science*, 329(5991):547–550, 2010.

[6] David Deutsch. Quantum theory, the church–turing principle and the universal quantum computer. *Proceedings of the Royal Society of London. A. Mathematical and Physical Sciences*, 400(1818):97–117, 1985.

[7] Peter W Shor. Algorithms for quantum computation: discrete logarithms and factoring. In *Proceedings 35th annual symposium on foundations of computer science*, pages 124–134. Ieee, 1994.

[8] Thomas Monz, Philipp Schindler, Julio T Barreiro, Michael Chwalla, Daniel Nigg, William A Coish, Maximilian Harlander, Wolfgang Hänsel, Markus Hennrich, and Rainer Blatt. 14-qubit entanglement: Creation and coherence. *Physical Review Letters*, 106(13):130506, 2011.

[9] Nicolai Friis, Oliver Marty, Christine Maier, Cornelius Hempel, Milan Holzäpfel, Petar Jurcevic, Martin B Plenio, Marcus Huber, Christian Roos, Rainer Blatt, et al. Observation of entangled states of a fully controlled 20-qubit system. *Physical Review X*, 8(2):021012, 2018.

[10] Ahmed Omran, Harry Levine, Alexander Keesling, Giulia Semeghini, Tout T Wang, Sepehr Ebadi, Hannes Bernien, Alexander S Zibrov, Hannes Pichler, Soonwon Choi, et al. Generation and manipulation of schrödinger cat states in rydberg atom arrays. *Science*, 365(6453):570–574, 2019.

[11] Rainer Blatt and David Wineland. Entangled states of trapped atomic ions. *Nature*, 453(7198):1008–1015, 2008.

[12] David S Weiss and Mark Saffman. Quantum computing with neutral atoms. *Physics Today*, 70(7), 2017.

[13] Rami Barends, Julian Kelly, Anthony Megrant, Andrzej Veitia, Daniel Sank, Evan Jeffrey, Ted C White, Josh Mutus, Austin G Fowler, Brooks Campbell, et al. Superconducting quantum circuits at the surface code threshold for fault tolerance. *Nature*, 508(7497):500–503, 2014.

[14] Gershon Kurizki, Patrice Bertet, Yuimaru Kubo, Klaus Mølmer, David Petrosyan, Peter Rabl, and Jörg Schmiedmayer. Quantum technologies with hybrid systems, 2015.

[15] H Jeff Kimble. The quantum internet. *Nature*, 453(7198):1023–1030, 2008.

[16] Stephan Ritter, Christian Nölleke, Carolin Hahn, Andreas Reiserer, Andreas Neuzner, Manuel Uphoff, Martin Mücke, Eden Figueroa, Joerg Bochmann, and Gerhard Rempe. An elementary quantum network of single atoms in optical cavities. *Nature*, 484(7393):195–200, 2012.

[17] Alfredo Rueda, Florian Sedlmeir, Michele C Collodo, Ulrich Vogl, Birgit Stiller, Gerhard Schunk, Dmitry V Strekalov, Christoph Marquardt, Johannes M Fink, Oskar Painter, et al. Efficient microwave to optical photon conversion: an electro-optical realization. *Optica*, 3(6):597–604, 2016.

[18] Timothy P McKenna, Jeremy D Witmer, Rishi N Patel, Wentao Jiang, Raphaël Van Laer, Patricio Arrangoiz-Arriola, E Alex Wollack, Jason F Herrmann, and Amir H Safavi-Naeini. Cryogenic microwave-to-optical conversion using a triply resonant lithium-niobate-on-sapphire transducer. *Optica*, 7(12):1737–1745, 2020.

[19] Reed W Andrews, Robert W Peterson, Tom P Purdy, Katarina Cicak, Raymond W Simmonds, Cindy A Regal, and Konrad W Lehnert. Bidirectional and efficient conversion between microwave and optical light. *Nature physics*, 10(4):321–326, 2014.

[20] A. P. Higginbotham, P. S. Burns, M. D. Urmey, R. W. Peterson, N. S. Kampel, B. M. Brubaker, G. Smith, K. W. Lehnert, and C. A. Regal. Harnessing electro-optic correlations in an efficient mechanical converter. *Nature Physics*, 14(10):1038–1042, 2018.

[21] Mohammad Mirhosseini, Alp Sipahigil, Mahmoud Kalaee, and Oskar Painter. Quantum transduction of optical photons from a superconducting qubit. *arXiv preprint arXiv:2004.04838*, 2020.

[22] Wentao Jiang, Christopher J. Sarabalis, Yanni D. Dahmani, Rishi N. Patel, Felix M. Mayor, Timothy P. McKenna, Raphaël Van Laer, and Amir H. Safavi-Naeini. Efficient bidirectional piezo-optomechanical transduction between microwave and optical frequency. *Nature Communications*, 11(1):1–7, 2020.

[23] M. Hafezi, Z. Kim, S. L. Rolston, L. a. Orozco, B. L. Lev, and J. M. Taylor. Atomic interface between microwave and optical photons. *Physical Review A - Atomic, Molecular, and Optical Physics*, 85(2):1–9, 2012.

[24] Jacob P Covey, Alp Sipahigil, and Mark Saffman. Microwave-to-optical conversion via four-wave mixing in a cold ytterbium ensemble. *Physical Review A*, 100(1):1–9, 2019.

[25] Bryan T. Gard, Kurt Jacobs, R. McDermott, and M. Saffman. Microwave-to-optical frequency conversion using a cesium atom coupled to a superconducting resonator. *Physical Review A*, 96(1):1–10, 2017.

[26] Jingshan Han, Thibault Vogt, Christian Gross, Dieter Jaksch, Martin Kiffner, and Wenhui Li. Coherent microwave-to-optical conversion via six-wave mixing in rydberg atoms. *Physical review letters*, 120(9):093201, 2018.

[27] Thibault Vogt, Christian Gross, Jingshan Han, Sambit B Pal, Mark Lam, Martin Kiffner, and Wenhui Li. Efficient microwave-to-optical conversion using Rydberg atoms. *Physical Review A*, 99(2):1–6, 2019.

[28] Donald W Booth, Joshua Isaacs, and M Saffman. Reducing the sensitivity of rydberg atoms to dc electric fields using two-frequency ac field dressing. *Physical Review A*, 97(1):012515, 2018.

[29] Marek Pechal and Amir H Safavi-naeini. Millimeter-wave interconnects for microwave-frequency quantum machines. 042305(June):1–13, 2017.

[30] Y Kaluzny, P Goy, M Gross, JM Raimond, and S Haroche. Observation of self-induced rabi oscillations in two-level atoms excited inside a resonant cavity: The ringing regime of superradiance. *Physical review letters*, 51(13):1175, 1983.

[31] D Meschede, Herbert Walther, and G Müller. One-atom maser. *Physical review letters*, 54(6):551, 1985.

[32] Michel Brune, F Schmidt-Kaler, Abdelhamid Maali, J Dreyer, E Hagley, JM Raimond, and S Haroche. Quantum rabi oscillation: A direct test of field quantization in a cavity. *Physical review letters*, 76(11):1800, 1996.

[33] Michel Brune, E Hagley, J Dreyer, X Maitre, Abdelhamid Maali, Ch Wunderlich, JM Raimond, and S Haroche. Observing the progressive decoherence of the "meter" in a quantum measurement. *Physical Review Letters*, 77(24):4887, 1996.

[34] A Boca, R Miller, KM Birnbaum, AD Boozer, J McKeever, and HJ Kimble. Observation of the vacuum rabi spectrum for one trapped atom. *Physical review letters*, 93(23):233603, 2004.

[35] CJ Hood, MS Chapman, TW Lynn, and HJ Kimble. Real-time cavity qed with single atoms. *Physical review letters*, 80(19):4157, 1998.

[36] Kevin M Birnbaum, Andreea Boca, Russell Miller, Allen D Boozer, Tracy E Northup, and H Jeff Kimble. Photon blockade in an optical cavity with one trapped atom. *Nature*, 436(7047):87–90, 2005.

[37] Martin Mücke, Joerg Bochmann, Carolin Hahn, Andreas Neuzner, Christian Nölleke, Andreas Reiserer, Gerhard Rempe, and Stephan Ritter. Generation of single photons from an atom-cavity system. *Physical Review A*, 87(6):063805, 2013.

[38] James K Thompson, Jonathan Simon, Huanqian Loh, and Vladan Vuletić. A high-brightness source of narrowband, identical-photon pairs. *Science*, 313(5783):74–77, 2006.

[39] Haruka Tanji, Saikat Ghosh, Jonathan Simon, Benjamin Bloom, and Vladan Vuletić. Heralded single-magnon quantum memory for photon polarization states. *Physical review letters*, 103(4):043601, 2009.

[40] Andreas Reiserer, Norbert Kalb, Gerhard Rempe, and Stephan Ritter. A quantum gate between a flying optical photon and a single trapped atom. *Nature*, 508(7495):237–240, 2014.

[41] Kristian Baumann, Christine Guerlin, Ferdinand Brennecke, and Tilman Esslinger. Dicke quantum phase transition with a superfluid gas in an optical cavity. *nature*, 464(7293):1301–1306, 2010.

[42] Juan A Muniz, Diego Barberena, Robert J Lewis-Swan, Dylan J Young, Julia RK Cline, Ana Maria Rey, and James K Thompson. Exploring dynamical phase transitions with cold atoms in an optical cavity. *Nature*, 580(7805):602–607, 2020.

[43] Masahiro Kitagawa and Masahito Ueda. Squeezed spin states. *Physical Review A*, 47(6):5138–5143, 1993.

[44] Monika H. Schleier-Smith, Ian D. Leroux, and Vladan Vuletić. Squeezing the collective spin of a dilute atomic ensemble by cavity feedback. *Physical Review A - Atomic, Molecular, and Optical Physics*, 81(2), 2010.

[45] Ian D. Leroux, Monika H. Schleier-Smith, and Vladan Vuletić. Implementation of cavity squeezing of a collective atomic Spin. *Physical Review Letters*, 104(7):1–4, 2010.

[46] Konrad Banaszek, Rafał Demkowicz-Dobrzański, and Ian A Walmsley. Quantum states made to measure. *Nature Photonics*, 3(12):673–676, 2009.

[47] D Linnemann, H Strobel, W Muessel, J Schulz, K V Kheruntsyan, and M K Oberthaler. Quantum-Enhanced Sensing Based on Time Reversal of Nonlinear Dynamics. 013001(July):1–5, 2016.

[48] Onur Hosten, Nils J Engelsen, Rajiv Krishnakumar, and Mark A Kasevich. Measurement noise 100 times lower than the quantum-projection limit using entangled atoms. *Nature*, 529(7587):505–508, 2016.

[49] Luca Pezzè, Augusto Smerzi, Markus K. Oberthaler, Roman Schmied, and Philipp Treutlein. Quantum metrology with nonclassical states of atomic ensembles. *Reviews of Modern Physics*, 90(3), 2018.

[50] Haruka Tanji-Suzuki, Ian D. Leroux, Monika H. Schleier-Smith, Marko Cetina, Andrew T. Grier, Jonathan Simon, and Vladan Vuletić. Interaction between Atomic Ensembles and Optical Resonators. Classical Description. *Advances in Atomic, Molecular and Optical Physics*, 60(November 2011):201–237, 2011.

[51] Yves Colombe, Tilo Steinmetz, Guilhem Dubois, Felix Linke, David Hunger, and Jakob Reichel. Strong atom–field coupling for bose–einstein condensates in an optical cavity on a chip. *Nature*, 450(7167):272–276, 2007.

[52] Claude Cohen-Tannoudji, Jacques Dupont-Roc, and Gilbert Grynberg. *Photons and Atoms-Introduction to Quantum Electrodynamics*. 1997.

[53] Daniel A Steck. *Quantum and atom optics*. 2007.

[54] Daniel Braak. Integrability of the rabi model. *Physical Review Letters*, 107(10):100401, 2011.

[55] P Forn-Díaz, L Lamata, E Rico, J Kono, and E Solano. Ultrastrong coupling regimes of light-matter interaction. *Reviews of Modern Physics*, 91(2):025005, 2019.

[56] Edwin T Jaynes and Frederick W Cummings. Comparison of quantum and semiclassical radiation theories with application to the beam maser. *Proceedings of the IEEE*, 51(1):89–109, 1963.

[57] L Tian and HJ Carmichael. Quantum trajectory simulations of two-state behavior in an optical cavity containing one atom. *Physical Review A*, 46(11):R6801, 1992.

[58] Howard J Carmichael. *Statistical methods in quantum optics 1: master equations and Fokker-Planck equations*, volume 1. Springer Science & Business Media, 1999.

[59] Daniel F Walls and Gerard J Milburn. *Quantum optics*. Springer Science & Business Media, 2007.

[60] Julio Gea-Banacloche, Ning Lu, Leno M Pedrotti, Sudhakar Prasad, Marlan O Scully, and Krzysztof Wãdkiewicz. Treatment of the spectrum of squeezing based on the modes of the universe. I. Theory and a physical picture. *Physical Review A*, 41(1):369–380, 1990.

[61] Marlan O Scully and M Suhail Zubairy. Quantum optics, 1999.

[62] P. M. Visser and G. Nienhuis. Solution of quantum master equations in terms of a non-Hermitian Hamiltonian. *Physical Review A*, 52(6):4727–4736, 1995.

[63] Ariel Sommer, Hans Peter B, and Jonathan Simon. Quantum Crystals and Laughlin Droplets of Cavity Rydberg Polaritons. pages 1–13, 2015.

[64] Jonathan Simon. Cavity QED with atomic ensembles. (May), 2010.

[65] Nathan Schine. Quantum hall physics with photons. 2019.

[66] Claude Cohen Tannoudji, Gilbert Grynberg, and J Dupont-Roe. Atom-photon interactions. 1992.

[67] R.H.Dicke. Coherence in Spontaneous Radiation Process. *Physical Review*, 93(1):99–110, 1954.

[68] Lawrence C Biedenharn, James D Louck, and Peter A Carruthers. *Angular momentum in quantum physics: theory and application*, volume 8. Addison-Wesley Reading, MA, 1981.

[69] M. D. Lukin. Colloquium: Trapping and manipulating photon states in atomic ensembles. *Reviews of Modern Physics*, 75(2):457–472, 2003.

[70] Jia Ningyuan, Alexandros Georgakopoulos, Albert Ryou, Nathan Schine, Ariel Sommer, and Jonathan Simon. Observation and characterization of cavity Rydberg polaritons. *Physical Review A - Atomic, Molecular, and Optical Physics*, 93(4):1–5, 2016.

[71] Mikhail D Lukin, Michael Fleischhauer, Marlan O Scully, and Vladimir L Velichansky. Intracavity electromagnetically induced transparency. 23(4):295–297, 2020.

[72] Lindsey F Keary and Jonathan D Pritchard. Strong coupling and active cooling in a finite temperature hybrid atom-cavity system. *arXiv preprint arXiv:2108.01386*, 2021.

[73] Alexey V. Gorshkov, Axel André, Mikhail D. Lukin, and Anders S. Sørensen. Photon storage in Λ -type optically dense atomic media. I. Cavity model . *Physical Review A*, 76(3):1–15, 2007.

[74] DI Schuster, Andrew Addison Houck, JA Schreier, A Wallraff, JM Gambetta, A Blais, L Frunzio, J Majer, B Johnson, MH Devoret, et al. Resolving photon number states in a superconducting circuit. *Nature*, 445(7127):515–518, 2007.

[75] Ray Radebaugh. Pulse tube cryocoolers. In *Low temperature and cryogenic refrigeration*, pages 415–434. Springer, 2003.

[76] P Micke, J Stark, SA King, T Leopold, T Pfeifer, Lisa Schmoeger, M Schwarz, LJ Spieß, PO Schmidt, and JR Crespo López-Urrutia. Closed-cycle, low-vibration 4 k cryostat for ion traps and other applications. *Review of Scientific Instruments*, 90(6):065104, 2019.

[77] J Schoser, A Batär, R Löw, V Schweikhard, A Grabowski, Yu B Ovchinnikov, and T Pfau. Intense source of cold rb atoms from a pure two-dimensional magneto-optical trap. *Physical Review A*, 66(2):023410, 2002.

[78] Zack Lasner, Debayan Mitra, Maryam Hiradfar, Benjamin Augenbraun, Lawrence Cheuk, Eunice Lee, Sridhar Prabhu, and John Doyle. Fast and high-yield loading of a d _2 mot of potassium from a cryogenic buffer gas beam. *arXiv preprint arXiv:2105.14701*, 2021.

[79] Kevin L Moore, Thomas P Purdy, Kater W Murch, Sabrina Leslie, Subhadeep Gupta, and Dan M Stamper-Kurn. Collimated, single-pass atom source from a pulsed alkali metal dispenser for laser-cooling experiments. *Review of Scientific Instruments*, 76(2):023106, 2005.

[80] James P McGilligan, Paul F Griffin, Erling Riis, and Aidan S Arnold. Phase-space properties of magneto-optical traps utilising micro-fabricated gratings. *Optics express*, 23(7):8948–8959, 2015.

[81] James P McGilligan, Paul F Griffin, Rachel Elvin, Stuart J Ingleby, Erling Riis, and Aidan S Arnold. Grating chips for quantum technologies. *Scientific reports*, 7(1):1–7, 2017.

[82] Dominik Schrader, Stefan Kuhr, Wolfgang Alt, Martin Müller, Victor Gomer, and Dieter Meschede. An optical conveyor belt for single neutral atoms. *Applied Physics B*, 73(8):819–824, 2001.

[83] Aziza Suleymanzade, Alexander Anferov, Mark Stone, Ravi K Naik, Andrew Oriani, Jonathan Simon, and David Schuster. A tunable high-q millimeter wave cavity for hybrid circuit and cavity qed experiments. *Applied Physics Letters*, 116(10):104001, 2020.

[84] Nikola Šibalić, Jonathan D Pritchard, Charles S Adams, and Kevin J Weatherill. Arc: An open-source library for calculating properties of alkali rydberg atoms. *Computer Physics Communications*, 220:319–331, 2017.

[85] E W Hudson, R W Simmonds, C A Yi Leon, S H Pan, and J C Davis. A Very Low Temperature Vibration Isolation System. *Proceedings of the 21st International Conference on Low Temperature Physics*, pages 2737–2738, 1996.

[86] Takayuki Tomaru, Toshikazu Suzuki, Tomiyoshi Haruyama, Takakazu Shintomi, Akira Yamamoto, Tomohiro Koyama, and Rui Li. Vibration analysis of cryocoolers. *Cryogenics*, 44(5):309–317, 2004.

[87] Saurabh Chaudhary, Janmey Jay Panda, Suman Mundlia, S Mathimalar, Aathif Ahmedof, and Karthik V Raman. A low noise cryogen-free scanning tunneling microscope–superconducting magnet system with vacuum sample transfer. *Review of Scientific Instruments*, 92(2):023906, 2021.

[88] Shuai Zhang, Di Huang, and Shiwei Wu. A cryogen-free low temperature scanning tunneling microscope capable of inelastic electron tunneling spectroscopy. *Review of Scientific Instruments*, 87(6):063701, 2016.

[89] Jason D Hackley, Dmitry A Kislitsyn, Daniel K Beaman, Stefan Ulrich, and George V Nazin. High-stability cryogenic scanning tunneling microscope based on a closed-cycle cryostat. *Review of Scientific Instruments*, 85(10):103704, 2014.

[90] Young Jae Song, Alexander F Otte, Vladimir Shvarts, Zuyu Zhao, Young Kuk, Steven R Blankenship, Alan Band, Frank M Hess, and Joseph A Stroscio. Invited review article: A 10 mk scanning probe microscopy facility. *Review of Scientific Instruments*, 81(12):121101, 2010.

[91] Stefan Seel, Rafael Storz, Giuseppe Ruoso, Jürgen Mlynek, and Stephan Schiller. Cryogenic Optical Resonators : A New Tool for Laser Frequency Stabilization at the 1 Hz Level. pages 4741–4744, 1997.

[92] David Hunger, Tilo Steinmetz, Yves Colombe, Christian Deutsch, Theodor W Hänsch, and Jakob Reichel. A fiber fabry–perot cavity with high finesse. *New Journal of Physics*, 12(6):065038, 2010.

[93] Javier Miguel-Sánchez, Andreas Reinhard, Emre Togan, Thomas Volz, Atac Imamoglu, Benjamin Besga, Jakob Reichel, and Jérôme Estève. Cavity quantum electrodynamics with charge-controlled quantum dots coupled to a fiber fabry–perot cavity. *New Journal of Physics*, 15(4):045002, 2013.

[94] Benjamin Besga, Cyril Vaneph, Jakob Reichel, Jérôme Estève, Andreas Reinhard, Javier Miguel-Sánchez, Ataç Imamoğlu, and Thomas Volz. Polariton boxes in a tunable fiber cavity. *Physical Review Applied*, 3(1):014008, 2015.

[95] Lukas Greuter, Sebastian Starosielec, Daniel Najer, Arne Ludwig, Luc Duempelmann, Dominik Rohner, and Richard J Warburton. A small mode volume tunable microcavity: Development and characterization. *Applied Physics Letters*, 105(12):121105, 2014.

[96] Maximilian Ruf, Matthew J Weaver, Suzanne B van Dam, and Ronald Hanson. Resonant excitation and purcell enhancement of coherent nitrogen-vacancy centers coupled to a fabry-perot microcavity. *Physical Review Applied*, 15(2):024049, 2021.

[97] Samarth Vadia, Johannes Scherzer, Holger Thierschmann, Clemens Schäfermeier, Claudio Dal Savio, Takashi Taniguchi, Kenji Watanabe, David Hunger, Khaled Karraï, and Alexander Högele. Open-cavity in closed-cycle cryostat as a quantum optics platform. *arXiv preprint arXiv:2103.05619*, 2021.

[98] Bernardo Casabone, Chetan Deshmukh, Shuping Liu, Diana Serrano, Alban Ferrier, Thomas Hümmer, Philippe Goldner, David Hunger, and Hugues de Riedmatten. Dynamic control of purcell enhanced emission of erbium ions in nanoparticles. *Nature communications*, 12(1):1–7, 2021.

[99] Yannik Fontana, Rigel Zifkin, Erika Janitz, Cesar Daniel Rodríguez Rosenblueth, and Lilian Childress. A mechanically stable and tunable cryogenic fabry–pérot microcavity. *Review of Scientific Instruments*, 92(5):053906, 2021.

[100] Benjamin Merkel, Alexander Ulanowski, and Andreas Reiserer. Coherent and purcell-enhanced emission from erbium dopants in a cryogenic high-q resonator. *Physical Review X*, 10(4):041025, 2020.

[101] Johannes FS Brachmann, Hanno Kaupp, Theodor W Hänsch, and David Hunger. Photothermal effects in ultra-precisely stabilized tunable microcavities. *Optics express*, 24(18):21205–21215, 2016.

[102] Martin de Wit, Gesa Welker, Kier Heeck, Frank M Buters, Hedwig J Eerkens, Gert Koning, Harmen van der Meer, Dirk Bouwmeester, and Tjerk H Oosterkamp. Vibration isolation with high thermal conductance for a cryogen-free dilution refrigerator. *Review of Scientific Instruments*, 90(1):015112, 2019.

[103] W. Zhang, J. M. Robinson, L. Sonderhouse, E. Oelker, C. Benko, J. L. Hall, T. Legero, D. G. Matei, F. Riehle, U. Sterr, and J. Ye. Ultrastable Silicon Cavity in a Continuously Operating Closed-Cycle Cryostat at 4 K. *Physical Review Letters*, 119(24):1–5, 2017.

[104] Shashank Misra, Brian B Zhou, Ilya K Drozdov, Jungpil Seo, Lukas Urban, Andras Gyenis, Simon CJ Kingsley, Howard Jones, and Ali Yazdani. Design and performance of an ultra-high vacuum scanning tunneling microscope operating at dilution refrigerator temperatures and high magnetic fields. *Review of Scientific Instruments*, 84(10):103903, 2013.

[105] Martin De Wit, Gesa Welker, Kier Heeck, Frank M. Buters, Hedwig J. Eerkens, Gert Koning, Harmen Van der Meer, Dirk Bouwmeester, and Tjerk H. Oosterkamp. Vibration isolation with high thermal conductance for a cryogen-free dilution refrigerator. *Review of Scientific Instruments*, 90(1), 2019.

[106] Sang Il Park and C. F. Quate. Theories of the feedback and vibration isolation systems for the scanning tunneling microscope. *Review of Scientific Instruments*, 58(11):2004–2009, 1987.

[107] E. E. Ungar and C. W. Dietrich. High-frequency vibration isolation. *Journal of Sound and Vibration*, 4(2):224–241, 1966.

[108] AI Oliva, M Aguilar, and Víctor Sosa. Low-and high-frequency vibration isolation for scanning probe microscopy. *Measurement Science and Technology*, 9(3):383, 1998.

[109] Y Kuk and PJ Silverman. Scanning tunneling microscope instrumentation. *Review of scientific instruments*, 60(2):165–180, 1989.

[110] Lisheng Chen, John L. Hall, Jun Ye, Tao Yang, Erjun Zang, and Tianchu Li. Vibration-induced elastic deformation of Fabry-Perot cavities. *Physical Review A - Atomic, Molecular, and Optical Physics*, 74(5):1–13, 2006.

[111] Thomas Kessler, Christian Hagemann, C Grebing, T Legero, Uwe Sterr, Fritz Riehle, MJ Martin, L Chen, and J Ye. A sub-40-mhz-linewidth laser based on a silicon single-crystal optical cavity. *Nature Photonics*, 6(10):687–692, 2012.

[112] Matthew Pelliccione, Adam Sciambi, John Bartel, AJ Keller, and David Goldhaber-Gordon. Design of a scanning gate microscope for mesoscopic electron systems in a cryogen-free dilution refrigerator. *Review of Scientific Instruments*, 84(3):033703, 2013.

[113] N Moussy, H Courtois, and B Pannetier. A very low temperature scanning tunneling microscope for the local spectroscopy of mesoscopic structures. *Review of Scientific Instruments*, 72(1):128–131, 2001.

[114] Han J.M.T.A. Adriaens, Willem L. De Koning, and Reinder Banning. Modeling piezoelectric actuators. *IEEE/ASME Transactions on Mechatronics*, 5(4):331–341, 2000.

[115] R W Peterson. Quantum measurement backaction and upconverting microwave signals with mechanical resonators. 2017.

[116] Malcolm C Smith. Synthesis of mechanical networks: the inerter. *IEEE Transactions on automatic control*, 47(10):1648–1662, 2002.

[117] Takurō Ikeda. *Fundamentals of piezoelectricity*. Oxford university press, 1996.

[118] A. Ansi/ieee standard 176-1987. *IEEE Standard on Piezoelectricity*, 1987.

[119] F. Wahl, G. Schmidt, and L. Forrai. On the significance of antiresonance frequencies in experimental structural analysis. *Journal of Sound and Vibration*, 219(3):379–394, 1999.

[120] Christian Sames, Haytham Chibani, Christoph Hamsen, Paul A Altin, Tatjana Wilk, and Gerhard Rempe. Antiresonance phase shift in strongly coupled cavity qed. *Physical Review Letters*, 112(4):043601, 2014.

[121] Eugen Skudrzyk. Theory of noise and vibration insulation of a system with many resonances. *The Journal of the Acoustical Society of America*, 31(1):68–74, 1959.

[122] Jun Ye, Travis C Briles, Dylan C Yost, Arman Cing, and Thomas R Schibli. Simple piezoelectric-actuated mirror with 180 kHz servo bandwidth. 18(10):9739–9746, 2010.

[123] Milan Mitrovic, Greg P Carman, and Friedrich K Straub. Response of piezoelectric stack actuators under combined electro-mechanical loading. *International journal of solids and structures*, 38(24-25):4357–4374, 2001.

[124] J. O. Almen and a. Laszlo. The uniform-section disk spring. *Transactions of the American Society of Mechanical Engineers*, 58:305–314, 1936.

[125] O Umezawa and K Ishikawa. Electrical and thermal conductivities and magnetization of some austenitic steels, titanium and titanium alloys at cryogenic temperatures. *Cryogenics*, 32(10):873–880, 1992.

[126] Nickel Development Institute. Materials for Cryogenic Service: Engineering Properties of Austenitic Stainless Steels.

[127] William Duffy. Acoustic quality factor of copper, brass and beryllium copper from 50 mK to 300 K. 623(19):241–248, 1993.

[128] William Duffy. Acoustic quality factor of aluminium and selected aluminium alloys from 50 mK to 300 K. *Cryogenics*, 42(3-4):245–251, 2002.

[129] William Duffy. Acoustic quality factor of niobium and vanadium at low temperatures. *Journal of Applied Physics*, 72(12):5628–5634, 1992.

[130] Y. K. Yong, S. O.R. Moheimani, B. J. Kenton, and K. K. Leang. Invited review article: High-speed flexure-guided nanopositioning: Mechanical design and control issues. *Review of Scientific Instruments*, 83(12), 2012.

[131] Yuen Kuan Yong. A new preload mechanism for a high-speed piezoelectric stack nanopositioner. *Mechatronics*, 36:159–166, 2016.

[132] Brian Jeffrey Kenton. *Design, characterization, and control of a high-bandwidth serial-kinematic nanopositioning stage for scanning probe microscopy applications*. University of Nevada, Reno, 2010.

[133] AN Oliveira, LS Moreira, RL Sacramento, L Kosulic, VB Brasil, W Wolff, and CL Cesar. Cryogenic mount for mirror and piezoelectric actuator for an optical cavity. *Review of Scientific Instruments*, 88(6), 2017.

[134] Lewis A. Williamson, Yu Hui Chen, and Jevon J. Longdell. Magneto-optic modulator with unit quantum efficiency. *Physical Review Letters*, 113(20):1–5, 2014.

[135] Jonathan Simon, Haruka Tanji, James K Thompson, and Vladan Vuletić. Interfacing collective atomic excitations and single photons. *Physical review letters*, 98(18):183601, 2007.

[136] A. Gogyan. Qubit transfer between photons at telecom and visible wavelengths in a slow-light atomic medium. *Physical Review A*, 81(2):2–5, 2010.

[137] Ningyuan Jia, Nathan Schine, Alexandros Georgakopoulos, Albert Ryou, Logan W Clark, Ariel Sommer, and Jonathan Simon. A strongly interacting polaritonic quantum dot. *Nature Physics*, page 1, 2018.

[138] K Saito, M Yamaguchi, H Kakiuchida, AJ Ikushima, K Ohsono, and Y Kurosawa. Limit of the rayleigh scattering loss in silica fiber. *Applied physics letters*, 83(25):5175–5177, 2003.

[139] Mark Stone, Aziza Suleymanzade, Lavanya Taneja, David I Schuster, and Jonathan Simon. Optical mode conversion in coupled fabry–perot resonators. *Optics Letters*, 46(1):21–24, 2021.

[140] Alipasha Vaziri, Gregor Weihs, and Anton Zeilinger. Experimental two-photon, three-dimensional entanglement for quantum communication. *Phys. Rev. Lett.*, 89(24):240401, 2002.

[141] Mohammad Mirhosseini, Omar S. Magaña-Loaiza, Malcolm N. O'Sullivan, Brandon Rodenburg, Mehul Malik, Martin P.J. Lavery, Miles J. Padgett, Daniel J. Gauthier, and Robert W. Boyd. High-dimensional quantum cryptography with twisted light. *New J. Phys.*, 17(3):033033, 2015.

[142] Nenad Bozinovic, Yang Yue, Yongxiong Ren, Moshe Tur, Poul Kristensen, Hao Huang, Alan E. Willner, and Siddharth Ramachandran. Terabit-scale orbital angular momentum mode division multiplexing in fibers. *Science*, 340(6140):1545–1548, 2013.

[143] M. W. Beijersbergen, R. P. C. Coerwinkel, M. Kristensen, and J. P. Woerdman. Helical-wavefront laser beams produced with a spiral phaseplate. *Opt. Commun.*, 112(5-6):321–327, 1994.

[144] Eliot Bolduc, Nicolas Bent, Enrico Santamato, Ebrahim Karimi, and Robert W. Boyd. Exact solution to simultaneous intensity and phase encryption with a single phase-only hologram. *Opt. Lett.*, 38(18):3546–3549, 2013.

[145] Philip Zupancic, Philipp M. Preiss, Ruichao Ma, Alexander Lukin, M. Eric Tai, Matthew Rispoli, Rajibul Islam, and Markus Greiner. Ultra-precise holographic beam shaping for microscopic quantum control. *Opt. Express*, 24(13):13881–13893, 2016.

[146] Marco W. Beijersbergen, Les Allen, H. E. L. O. Van der Veen, and J. P. Woerdman. Astigmatic laser mode converters and transfer of orbital angular momentum. *Opt. Commun.*, 96(1-3):123–132, 1993.

[147] Jesse Lu and Jelena Vučković. Objective-first design of high-efficiency, small-footprint couplers between arbitrary nanophotonic waveguide modes. *Opt. Express*, 20(7):7221–7236, 2012.

[148] Daoxin Dai and Mao Mao. Mode converter based on an inverse taper for multimode silicon nanophotonic integrated circuits. *Opt. Express*, 23(22):28376–28388, 2015.

[149] Sergio G. Leon-Saval, Nicolas K. Fontaine, Joel R. Salazar-Gil, Burcu Ercan, Roland Ryf, and Joss Bland-Hawthorn. Mode-selective photonic lanterns for space-division multiplexing. *Opt. Express*, 22(1):1036–1044, 2014.

[150] Gregorius C. G. Berkhout, Martin P. J. Lavery, Johannes Courtial, Marco W. Beijersbergen, and Miles J. Padgett. Efficient sorting of orbital angular momentum states of light. *Phys. Rev. Lett.*, 105:153601, 2010.

[151] Guillaume Labroille, Bertrand Denolle, Pu Jian, Philippe Genevaux, Nicolas Treps, and Jean-François Morizur. Efficient and mode selective spatial mode multiplexer based on multi-plane light conversion. *Opt. Express*, 22(13):15599–15607, 2014.

[152] Nicolas K. Fontaine, Roland Ryf, Haoshuo Chen, David T. Neilson, Kwangwoong Kim, and Joel Carpenter. Laguerre-gaussian mode sorter. *Nat. Commun.*, 10(1):1–7, 2019.

[153] David A. B. Miller. Self-configuring universal linear optical component. *Photonics Res.*, 1(1):1–15, 2013.

[154] Antonio Ribeiro, Alfonso Ruocco, Laurent Vanacker, and Wim Bogaerts. Demonstration of a 4× 4-port universal linear circuit. *Optica*, 3(12):1348–1357, 2016.

[155] Siddharth Ramachandran, Zhiyong Wang, and Man Yan. Bandwidth control of long-period grating-based mode converters in few-mode fibers. *Opt. Lett.*, 27(9):698–700, 2002.

[156] Adolfo del Campo. Shortcuts to adiabaticity by counterdiabatic driving. *Phys. Rev. Lett.*, 111(10):100502, 2013.

[157] William R. Sweeney, Wei Hsu Chia, and Douglas A. Stone. Theory of reflectionless scattering modes. *Preprint at https://arxiv.org/abs/1909.04017*, 2019.

[158] Lian-Wee Luo, Noam Ophir, Christine P Chen, Lucas H. Gabrielli, Carl B. Poitras, Keren Bergmen, and Michal Lipson. Wdm-compatible mode-division multiplexing on a silicon chip. *Nat. Comm.*, 5(1):1–7, 2014.

[159] M. Raquib Ehsan, Saika Muntaha Bari, Mainul Haque, and Intekhab Alam. Optical mode converter using ring resonator structure. *Conference on Lasers and Electro-Optics Pacific Rim*, page 27P_53, 2015.

[160] S. Boscolo, M. Midrio, and T. F. Krauss. Y junctions in photonic crystal channel waveguides: high transmission and impedance matching. *Opt. Lett.*, 27(12):1001–1003, 2002.

[161] Jérôme Poirson, Fabien Bretenaker, Marc Vallet, and Albert Le Floch. Analytical and experimental study of ringing effects in a fabry–perot cavity. application to the measurement of high finesses. *J. Opt. Soc. Am. B*, 14(11):2811–2817, 1997.

[162] A. E. Siegman. *Lasers*. University Science Books, Sausalito, 1986.

[163] Stefan Hild, Harald Lück, Walter Winkler, Ken Strain, Hartmut Grote, Joshua Smith, Michaela Malec, Martin Hewitson, Benno Willke, James Hough, and Karsten Danzmann. Measurement of a low-absorption sample of oh-reduced fused silica. *Appl. Opt.*, 45(28):7269–7272, 2006.

[164] Qingzhong Huang, Ge Song, Juguang Chen, Zhan Shu, and Jinzhong Yu. Proposal and fabrication of an electrooptically controlled multimode microresonator for continuous fast-to-slow light tuning. *IEEE Photonics J.*, 6(4):1–11, 2014.

[165] Jesse Lu, Stephen Boyd, and Jelena Vučković. Inverse design of a three-dimensional nanophotonic resonator. *Opt. Express*, 19(11):10563–10570, 2011.

[166] Christina J. Hood, H. J. Kimble, and Jun Ye. Characterization of high-finesse mirrors: Loss, phase shifts, and mode structure in an optical cavity. *Phys. Rev. A*, 64(3):033804, 2001.

[167] Nathan Schine, Albert Ryou, Andrey Gromov, Ariel Sommer, and Jonathan Simon. Synthetic landau levels for photons. *Nature*, 534(7609):671–675, 2016.

[168] Samuel J. Whiteley, Gary Wolfowicz, Christopher P. Anderson, Alexandre Bourassa, He Ma, Meng Ye, Gerwin Koolstra, Kevin .J Satzinger, Martin V. Holt, F. Joseph Heremans, Andrew N. Cleland, David I. Schuster, Giulia Galli, and David D. Awschalom. Spin–phonon interactions in silicon carbide addressed by gaussian acoustics. *Nature Phys.*, 15(5):490–495, 2019.

[169] Samuel J. Mason. Feedback theory-some properties of signal flow graphs. *Proc. IRE*, 41(9):1144–1156, 1953.

[170] D. Riegle and P. Lin. Matrix signal flow graphs and an optimum topological method for evaluating their gains. *IEEE Trans. Circuit Theory*, 19(5):427–435, 1972.

[171] George B. Arfken, Hans J. Weber, and Frank E. Harris. *Mathematical methods for physicists*. Academic Press, Waltham, 7 edition, 2011.

[172] Zhexin Zhao, Cheng Guo, and Shanhui Fan. Connection of temporal coupled-mode-theory formalisms for a resonant optical system and its time-reversal conjugate. *Phys. Rev. A*, 99(3):033839, 2019.

[173] Wonjoo Suh, Zheng Wang, and Shanhui Fan. Temporal coupled-mode theory and the presence of non-orthogonal modes in lossless multimode cavities. *IEEE J. Quantum Electron.*, 40(10):1511–1518, 2004.

[174] Crispin W. Gardiner and M. J. Collett. Input and output in damped quantum systems: Quantum stochastic differential equations and the master equation. *Phys. Rev. A*, 31(6):3761, 1985.

[175] Hermann A Haus. *Waves and fields in optoelectronics*. Prentice-Hall, Englewood Cliffs, 1984.

[176] Robert J. Lang and Amnon Yariv. An exact formulation of coupled-mode theory for coupled-cavity lasers. *IEEE J. Quantum Electron.*, 24(1):66–72, 1988.

APPENDIX A

SI: MODE CONVERSION

A.1 Single-Mode S-Matrix Approach for Coupled Fabry Pérot Cavities

The behavior of a general linear coupled cavity system may be exactly analyzed with a scattering (S) matrix approach, so long as the paraxial and scalar field approximations are valid. In this section only a single spatial mode will be considered. The light field in a given transverse plane may then be described as an amplitude of a right- and a left-traveling wave, or a vector $\boldsymbol{\psi} = (\psi_r, \psi_l)^T$.

For a region of space containing paraxial optical elements between two transverse planes, there exists a mapping between the incoming waves on either side to the outgoing waves, called the scattering matrix. With the two sides labeled A and B, the scattering matrix $\boldsymbol{S}$ is defined by:

$$\begin{bmatrix} \boldsymbol{\psi}_{A,out} \\ \boldsymbol{\psi}_{B,out} \end{bmatrix} = \begin{bmatrix} S_{11} & S_{12} \\ S_{21} & S_{22} \end{bmatrix} \begin{bmatrix} \boldsymbol{\psi}_{A,in} \\ \boldsymbol{\psi}_{B,in} \end{bmatrix} \tag{A.1}$$

The scattering matrices for simple optical elements like on-axis mirrors and regions of free propagation are well known. When multiple optical elements are placed in succession, the overall scattering matrix can be calculated by the transfer matrix approach, or equivalently by pairwise application of the cascaded scattering matrix formula:

$$\boldsymbol{S}^{\text{tot}} = \begin{bmatrix} S_{11}^1 + S_{12}^1 S_{11}^2 F S_{21}^1 & S_{12}^1 \left(1 + S_{11}^2 F S_{22}^1\right) S_{12}^2 \\ S_{21}^2 F S_{21}^1 & S_{22}^2 + S_{21}^2 F S_{22}^1 S_{12}^2 \end{bmatrix} \tag{A.2}$$

with $F = \left(1 - S_{22}^1 S_{11}^2\right)^{-1}$.

This formula is sufficient to calculate the overall behavior of a single-mode paraxial system. Using the elementary scattering matrices for free propagation, $\boldsymbol{P} = \begin{bmatrix} 0 & e^{i\phi/2} \\ e^{i\phi/2} & 0 \end{bmatrix}$ and mirrors, $\boldsymbol{M} = \begin{bmatrix} r & it \\ it & r \end{bmatrix}$, we obtain the scattering matrix for a Fabry-Pérot resonator:

$$\boldsymbol{S}^{FP} = \begin{bmatrix} r_1 - \frac{e^{i\phi} t_1^2 r_2}{1 - e^{i\phi} r_1 r_2} & -\frac{e^{\frac{i\phi}{2}} t_1 t_2}{1 - e^{i\phi} r_1 r_2} \\ -\frac{e^{\frac{i\phi}{2}} t_1 t_2}{1 - e^{i\phi} r_1 r_2} & r_2 - \frac{e^{i\phi} t_2^2 r_1}{1 - e^{i\phi} r_1 r_2} \end{bmatrix} \tag{A.3}$$

where ϕ is the round-trip phase accrued in the cavity and r_i, t_i are the field reflection and transmission coefficients. For two coupled Fabry-Pérots the transmitted component is

$$S_{11} = \frac{-ie^{\frac{1}{2}i(\phi_1+\phi_2)} t_1 t_2 t_3}{1 - e^{i\phi_1} r_1 r_2 - e^{i\phi_2} r_2 r_3 + e^{i(\phi_1+\phi_2)} r_1 r_3 \left(r_2^2 + t_2^2\right)} \tag{A.4}$$

An effective finesse for the primary cavity can be extracted by putting Equation A.4 in the usual form of transmission through a Fabry-Pérot, $E_t/E_i = -\frac{e^{\frac{i\phi_1}{2}} t_1 t_{23}}{1 - g e^{i\phi_1}}$, with round-trip gain:

$$g = r_1 \frac{r_2 - r_3 e^{i\phi_2} \left(r_2^2 + t_2^2\right)}{1 - r_2 r_3 e^{i\phi_2}} \tag{A.5}$$

and t_{23} the transmission of the M_{23} cavity. Both of these numbers vary slowly with ϕ_2 in high-finesse configurations. Then the finesse is evaluated as [162] $\mathcal{F} = \frac{\pi\sqrt{|g|}}{1-|g|}$.

The effect of mirror loss on the transmitted field can be easily calculated. Loss in the outer mirrors M_1 and M_3 simply reduces the transmitted power by a factor of $\frac{T_1}{1-R_1}\frac{T_3}{1-R_3}$, where $1 - R_i$ is the power transmission of a lossless mirror with the same reflectance. To

treat loss in M_2, we note that Equation A.4 is invariant under the substitution:

$$
\begin{aligned}
r_2 \to r_2' &= \frac{r_2}{\beta} \\
t_2 \to t_2' &= \frac{t_2}{\beta} \\
r_1 \to r_1' &= \beta r_1 \\
r_3 \to r_3' &= \beta r_3 \\
t_1 \to t_1' &= \beta t_1 \\
\beta^2 &= r_2^2 + t_2^2 = 1 - L_2
\end{aligned}
$$

Thus the transmitted field of a cavity with lossy M_2 is equivalent to a cavity with lossless M_2 and modified M_1 and M_3. This cavity has spectral properties set by R_1', R_2', R_3' and also a loss-induced amplitude reduction given by $\frac{T_1'}{1-R_1'}\frac{T_3'}{1-R_3'} = \beta\frac{T_1}{1-\beta^2 R_1}\frac{T_3}{1-\beta^2 R_3} \approx \frac{T_1}{T_1+L_1+L_2}\frac{T_3}{T_3+L_3+L_2}$ in the high reflectance limit.

Multielement scattering systems may also be treated as a signal flow graph and efficiently solved with Mason's gain formula [169].

A.2 Suppression of Loss Through Higher-Order Modes

In the tunable finesse cavity, imperfect mode matching leads to leakage of light out of the M_1-M_{23} cavity through higher-order modes of M_{23}, potentially limiting the maximum achievable finesse. As with leakage through the lowest mode of M_{23}, this loss is suppressed as the modes are detuned from the primary cavity resonance. By making the M_{23} cavity highly degenerate, it is possible for the fundamental mode of the primary cavity to be spectrally isolated from all modes of the M_{23} cavity, thus avoiding accidental near-degeneracies. We choose L to realize a half-confocal cavity with $\omega_{nlm} = \omega_{fsr}\left[n + \frac{1}{4}(l+m)\right]$, ensuring that the mode of the primary cavity is detuned by at least 1/8 of a free spectral range (FSR) from all modes of

M_{23}. This detuning results in a transmission suppression of $\frac{2-\sqrt{2}}{4} \approx 15\%$ relative to that at a detuning of 1/2 the FSR: as long as the mode matching is better than 85%, the maximum finesse should not be significantly affected.

A.3 Multimode Scattering Matrix Approach for Coupled Fabry-Pérot Cavities

A general paraxial system may be analyzed by the same scattering matrix approach with simple modifications. For simplicity this discussion will use a single transverse dimension, but the approach is easily extended to a full 2D transverse treatment. The light field in a given transverse plane may be decomposed into a basis of orthonormal Hermite-Gauss mode amplitudes for right- and left-traveling waves, described by a vector $\boldsymbol{\psi} = \left(\psi_{0,r}, \psi_{1,r}, \ldots, \psi_{n,r}, \psi_{0,l}, \psi_{1,l}, \ldots, \psi_{n,l}\right)^T = (\boldsymbol{\psi}_r, \boldsymbol{\psi}_l)^T$. It is accurate to restrict to a finite number n modes so long as the field distribution is bounded and nonsingular.

There is an infinite family of such Hermite-Gauss decompositions parameterized by the "complex beam parameter" q and an axis around which the modes are centered. q determines both the scaling (or waist) of the basis functions, and the degree of wavefront curvature.

Equations A.1 and A.2 are both valid in the multimode case, but with the entries S_{ij} understood to be block matrices of size $n \times n$. As long as the multimode scattering matrices of the individual optical elements are known, the overall scattering matrix may be calculated.

In the Hermite-Gauss basis, the scattering matrices of paraxial optical elements, such as free-space propagation and on-axis mirrors, have a simple form. Such elements do not produce mixing between modes, only overall rescaling and wavefront curvature, amounting to a change in the q parameter [162]. Put another way, the block elements S_{ij} of the scattering matrix are diagonal, so long as it is understood that the fields on each port of the interface are expressed in Hermite-Gauss bases with the appropriate q values. We could express the vector with reference to its basis $\boldsymbol{\psi} = \left(\boldsymbol{\psi}_{r,q_r}, \boldsymbol{\psi}_{l,q_l}\right)^T$, but this will be left implicit in our

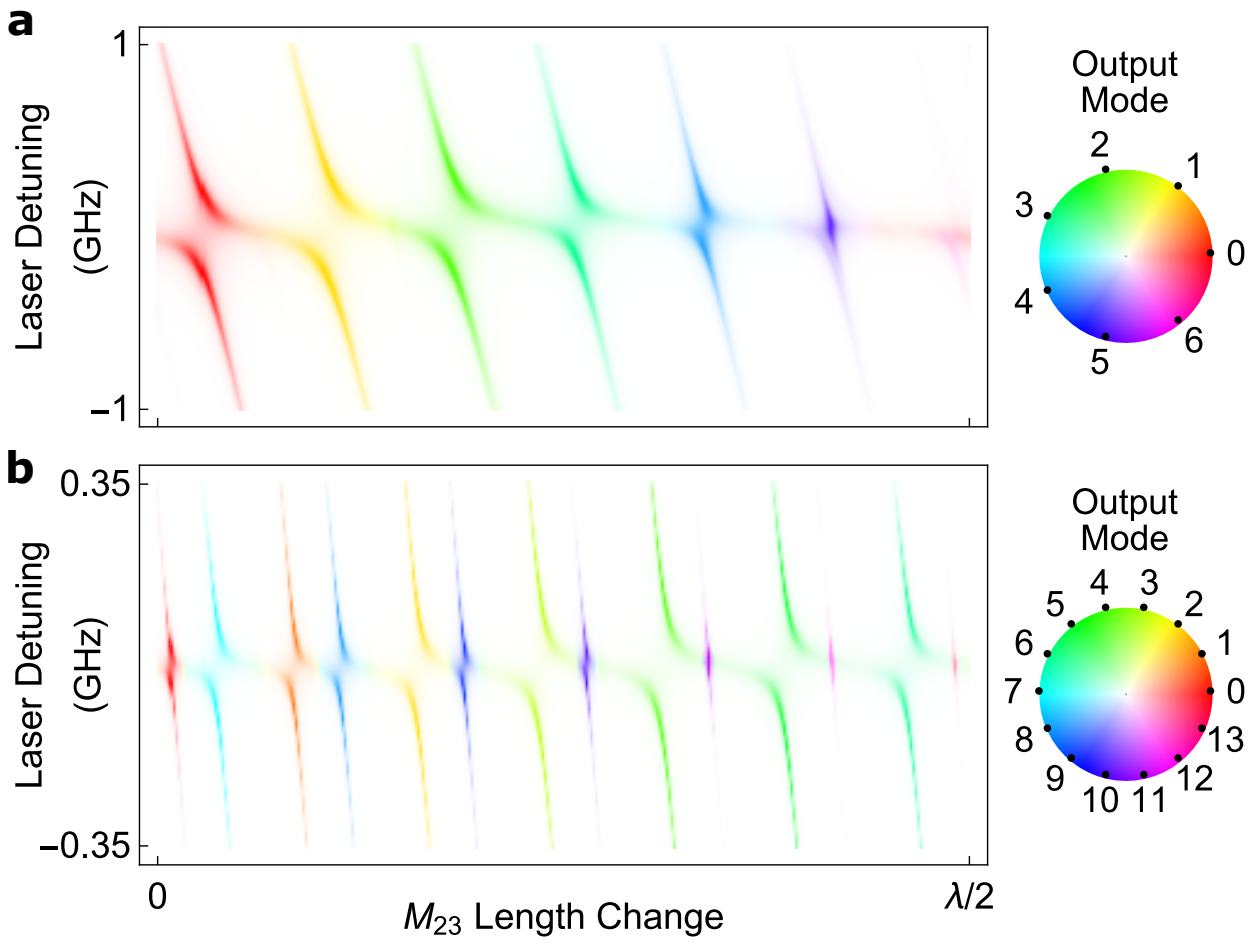

Figure A.1: **Simulated Spectrum of Coupled Multimode Optical Resonators. a,** Simulated transmission of the mode converter demonstrated in the main text, with $T_1 = T_3 = 0.035$, $T_2 = 0.028$, and an input HG_{00} beam. The output mode content (indicated by hue) varies as the length of the M_{23} cavity is tuned, bringing different HG_{m0} modes near resonance with the primary cavity. The output power (indicated by color saturation) reaches near unity at the impedance matched condition, as confirmed by the measured cross-sections in Fig. 3 of the main text, corresponding to perfect mode conversion. Successive mode orders display reduced peak splitting, reflecting a reduced coupling to the HG_{00} mode of the primary cavity. After HG_{50} the splitting is smaller than the cavity linewidth and impedance matching cannot be achieved, so higher-order modes disappear from the spectrum. The coupling coefficients are set by the transverse offset between cavities, here 1.3 mode waists. **b,** Increasing mirror reflectance ($T_1 = T_2 = T_3 = 0.01$) and transverse offset (2.1 mode waists) allows more modes to be impedance matched, and reduces leakage into accidentally near-degenerate modes. An input HG_{00} can be coherently converted into HG_{00}–$HG_{13,0}$. Modes HG_{70}–$HG_{13,0}$ belong to the next lower axial mode group and appear interspersed amongst HG_{00}–HG_{60}.

equations. The required relation between q values on each port of a paraxial element can be calculated using the ABCD matrix formalism, but it is not necessary for this discussion.

Inside an optical resonator, there exists a particular choice of q which is transformed back into itself after each round trip [162]. This is the most convenient choice, and it guarantees that every element of the resonator is described in a diagonal basis for most resonators, including all two-mirror resonators.

However, the mode converter consists of two optical resonators which have mismatched optical axes and/or waists, so no choice of optical axis and q will yield diagonal forms for the scattering matrices of all elements. One solution is to describe the third mirror as an off-axis mirror whose scattering matrix has mode-mixing terms. Instead, we add an explicit change-of-basis matrix at the interface between the two resonators. This does not represent a physical optical element, but a mathematical transformation which allows the field on either side to be written in different bases. The matrix conveniently casts the field inside each resonator in terms of the eigenmodes of that resonator. The elements of the change-of-basis scattering matrix take the form

$$\begin{aligned} S_{12,mn} &= \langle \psi_m | \psi_n \rangle \\ S_{21} &= S_{12}^\dagger \equiv K^\dagger \\ S_{11} &= 0 \\ S_{22} &= 0 \end{aligned}$$

where the overlap integral $\langle \psi_m | \psi_n \rangle$ between Hermite-Gauss modes with different optical axis and q may be calculated numerically, or analytically using the method in Supplement A.5.

The scattering matrices for paraxial elements with the correct q are as follows. Mirrors act as n copies of the form $\boldsymbol{M}$ from Supplement A.1 on the individual modes. Propagation through free space gives a phase shift $P_{12,mn} = S_{21,mn} = \delta_{mn} e^{i[kL+(m+1)\theta]}$, where θ is the

well-known Gouy phase which may be calculated from q and L.

The overall scattering matrix for mode-mismatched coupled cavities may be found from repeated application of Equation A.2. The left-to-right transmission is:

$$\boldsymbol{S}_{21} = -it_1t_2t_3e^{i\boldsymbol{\Phi_2}/2}\boldsymbol{K}\left[\boldsymbol{I} - r_1r_2e^{i\boldsymbol{\Phi_1}} - r_2r_3\boldsymbol{K}^\dagger e^{i\boldsymbol{\Phi_2}}\boldsymbol{K} + \left(r_2^2+t_2^2\right)r_1r_3e^{i\boldsymbol{\Phi_1}}\boldsymbol{K}^\dagger e^{i\boldsymbol{\Phi_2}}\boldsymbol{K}\right]^{-1} e^{i\boldsymbol{\Phi_1}/2} \tag{A.6}$$

and the left-to-left reflection is:

$$\begin{aligned}\boldsymbol{S}_{11} = r_1\boldsymbol{I} - t_1^2e^{i\boldsymbol{\Phi_1}/2}&\left[r_2\boldsymbol{I} - \left(r_2^2+t_2^2\right)r_3\boldsymbol{K}^\dagger e^{i\boldsymbol{\Phi_2}}\boldsymbol{K}\right]\times \\ &\left[\boldsymbol{I} - r_1r_2e^{i\boldsymbol{\Phi_1}} - r_2r_3\boldsymbol{K}^\dagger e^{i\boldsymbol{\Phi_2}}\boldsymbol{K} + \left(r_2^2+t_2^2\right)r_1r_3e^{i\boldsymbol{\Phi_1}}\boldsymbol{K}^\dagger e^{i\boldsymbol{\Phi_2}}\boldsymbol{K}\right]^{-1} e^{i\boldsymbol{\Phi_1}/2}\end{aligned} \tag{A.7}$$

where $\boldsymbol{\Phi}_i$ is the round trip propagation matrix for cavity i, including Gouy phases.

The mode converter of the main text is simulated using the S-matrix formalism in Fig. A.1. Near-unity efficiency mode conversion is predicted when different modes of the two cavities are near resonant, as measured experimentally in Fig. 3 of the main text.

Multielement, multimode cavities may also be treated as noncommutative signal-flow graphs with matrix-valued weights and efficiently solved with Riegle's rule [170].

A.4 Mode Purity

Mode purity can be calculated exactly using the S-matrix formalism, or estimated from the mirror transmission coefficients. Mode purity is degraded due to imperfectly suppressed outcoupling through parasitic modes of the M_{23} cavity. The mode in the primary cavity sees outcoupling through the target mode $T_{23}^{i\leftrightarrow j}$, which is set approximately equal to T_1 in the impedance matched condition. It also sees outcoupling through each unwanted mode p equal to $T_{23}^{i\leftrightarrow p} = \left|\alpha_{ip}\right|^2 T_2T_3f_p(\omega)$, where α_{ip} is the mode overlap integral and $f_p(\omega)$ is a resonant enhancement factor, which is of order unity if the mode is moderately detuned.

The ratio between power in parasitic mode p and the target mode j therefore scales as $\left|\alpha_{ip}\right|^2 \frac{T_2 T_3}{T_1} f_p(\omega)$. We note that the sum of all overlap integrals is bounded as $\sum_k \left|\alpha_{ik}\right|^2 = 1$. This estimate neglects the second-order effect of additional modes excited in the primary cavity.

A.5 Overlap of Hermite-Gauss Modes

To analyze coupled resonators which are not spatially mode-matched, it is useful to perform a change of basis between their eigenmodes. This transformation requires the overlap integrals between offset and/or rescaled Hermite-Gauss (HG) functions. These integrals may be calculated numerically, in which case it is useful to calculate the Hermite polynomials using a stable algorithm such as the recurrence relation [171] $H_{n+1}(x) = 2xH_n(x) - 2nH_{n-1}(x)$. They can also be calculated analytically using the method of generating functions. Here we work in a single transverse dimension for simplicity. The normalized Hermite-Gauss functions HG_n with waist w are given by:

$$\mathrm{HG}_n(x; w) = \sqrt{\frac{\sqrt{2/\pi}}{2^n n! w}} H_n\left(\frac{\sqrt{2}x}{w}\right) e^{-\frac{x^2}{w^2}} \tag{A.8}$$

where $H_n(x)$ is the nth-order Hermite polynomial and the HG functions are taken to have no wavefront curvature (valid when the overlap is taken at the mode waist). The generating function for unnormalized HG functions is:

$$g_w(x,t) = e^{\frac{2\sqrt{2}x}{w}t - t^2} e^{-\frac{x^2}{w^2}} \tag{A.9}$$

$$= \sum_{n=0}^{\infty} H_t\left(\frac{\sqrt{2}x}{w}\right) e^{-\frac{x^2}{w^2}} \frac{t^n}{n!} \tag{A.10}$$

The overlap integral between modes m and n of two HG bases is calculated by taking the integral of the product of their respective generating functions, picking off the correct series

coefficients, and inserting normalization factors:

$$\int \mathrm{HG}^*_{m,\lambda w}(x)\mathrm{HG}_{n,w}(x+aw)dx = \sqrt{\frac{2}{\pi 2^m m! 2^n n! \lambda w^2}}\left[\frac{d^m}{du^m}\frac{d^n}{dt^n}\int g^*_{\lambda w}(x,u)g_w(x+a,t)dx\right]_{u,t=0} \tag{A.11}$$

$$= \sqrt{\frac{2}{2^m m! 2^n n!}}\sqrt{\frac{\lambda}{1+\lambda^2}}e^{-\frac{a^2}{1+\lambda^2}} \times \left\{\frac{d^m}{du^m}\frac{d^n}{dt^n}\mathrm{Exp}\left[\frac{(1-\lambda^2)(t^2-u^2)+4tu\lambda+2\sqrt{2}a(u-\lambda t)}{1+\lambda^2}\right]\right\}_{u,t=0} \tag{A.12}$$

In this work we only require the overlap of modes with zero wavefront curvature. However, a similar derivation applies more generally, using the complex q-parameter formulation of the Hermite-Gauss functions.

A.6 Two-Mode Coupled Mode Analysis

In Supplement A.7 we derive coupling constants for the phenomenological temporal coupled mode theory (TCMT) treatment of multimode coupled optical cavities. Here we use the results for a simple case with two transversely offset optical resonators coupled through a shared mirror, each supporting a single mode (which may have different transverse profiles). Assuming reciprocal media and neglecting loss, the scattering matrix takes the form [172, 173]:

$$S = -I - i\boldsymbol{D}\frac{1}{(\boldsymbol{\Omega}-i\boldsymbol{\Gamma})-\omega}\boldsymbol{D}^T \tag{A.13}$$

with

$$\boldsymbol{\Omega} = \begin{bmatrix} -\frac{\delta}{2} & g \\ g & \frac{\delta}{2} \end{bmatrix} \tag{A.14}$$

$$\boldsymbol{D} = \begin{bmatrix} \sqrt{\gamma_1} & 0 \\ 0 & \sqrt{\gamma_2} \end{bmatrix} \tag{A.15}$$

$$\boldsymbol{\Gamma} = \boldsymbol{D}^\dagger \boldsymbol{D} = \begin{bmatrix} \frac{\gamma_1}{2} & 0 \\ 0 & \frac{\gamma_2}{2} \end{bmatrix} \tag{A.16}$$

$$\tag{A.17}$$

with δ the detuning between the modes. The coupling rate between the resonator mode in cavity i and its corresponding output channel is $\sqrt{\gamma_i} = -\log R_i \nu_i$, where ν_i is the free spectral range and R_i is the reflectance of the output mirror. The coupling rate between the two resonator modes is $g = \alpha\sqrt{-\log R_c \nu_1 \nu_2}$, where α is the overlap integral between the two modes and R_c is the reflectance of the shared mirror.

Impedance matching occurs when the reflection coefficient vanishes. In the energy-conserving case, transmission reaches unity at this point, indicating full mode conversion. With matched cavity decay rates $\gamma_1 = \gamma_2 = \gamma$, this occurs at $\delta = 0$, $\omega = \pm\sqrt{g^2 - \left(\frac{\gamma}{2}\right)^2}$. Under these conditions, evaluation of the eigenmodes of the effective Hamiltonian, $\boldsymbol{\Omega} - i\boldsymbol{\Gamma}$, shows that equal stored energy resides in each cavity.

For $g < \frac{\gamma}{2}$ there is no real solution, but the minimum reflection occurs at $\delta = 0, \omega = 0$. Thus a solution with unit efficiency mode conversion exists whenever $|\alpha|^2 > \frac{\gamma^2}{-4 \log R_c \nu_1 \nu_2}$.

For mismatched cavity decay rates $\gamma_1 \neq \gamma_2$, impedance matching occurs at $\delta \neq 0$, but there is still generally a solution for sufficiently large $|\alpha|$. In this case, the product of the stored energy and the decay constant of each cavity is equal.

A.7 Multimode Coupled Mode Analysis

The S-matrix analysis of Supplement A.3 relies only on the paraxial and scalar field approximations and is otherwise exact. Coupled optical cavities can also be analyzed using the temporal coupled mode theory (TCMT), a phenomenological model of open resonant optical systems. Although TCMT is not derived from first principles, it has been shown to agree well with rigorous analysis and provides useful intuition for the design of optical devices. TCMT is mathematically equivalent to the input-output formalism of damped quantum systems [174]. Here a full multimode theory for coupled optical resonators will be developed, while Supplement A.6 specializes to the two-mode limit to discuss impedance matching.

In this formalism an optical cavity is described by a set of M cavity modes which are allowed to couple with each other and with N ports, each containing an incoming and outgoing propagating channel. Assuming reciprocal media, the coupled mode equations are [172, 173, 157] :

$$\frac{d}{dt}\boldsymbol{a} = -i\left(\boldsymbol{\Omega} - i\boldsymbol{\Gamma}\right)\boldsymbol{a} + \boldsymbol{D}^T\boldsymbol{s}_+ \tag{A.18}$$

$$\boldsymbol{s}_- = \boldsymbol{C}\boldsymbol{s}_+ + \boldsymbol{D}\boldsymbol{a} \tag{A.19}$$

where $\boldsymbol{a}$ is a state vector containing the M amplitudes of the modes, normalized such that $|a_i|^2$ corresponds to the energy stored in the ith mode. $\boldsymbol{\Omega}$ and $\boldsymbol{\Gamma}$ are $M \times M$ Hermitian matrices, with $\boldsymbol{\Omega}$ representing the resonator mode frequencies and couplings and $\boldsymbol{\Gamma}$ representing decay processes. The resonances are coupled to the N incoming channels $\boldsymbol{s}_+$ and outgoing channels $\boldsymbol{s}_-$ according to the coefficients in the $N \times M$ matrix $\boldsymbol{D}$. The channel amplitudes are normalized such that $|s_{+i}|^2$ ($|s_{-i}|^2$) is the power carried by the ith incoming (outgoing) channel. The $N \times N$ symmetric matrix $\boldsymbol{C} = \boldsymbol{C}^T$ represents direct coupling from input to output channels, including direct reflection and processes not included in the resonant modes $\boldsymbol{a}$.

Assuming harmonic time dependence for $\boldsymbol{a}$ then eliminating $\boldsymbol{a}$ from Equations A.18, A.19 gives the S-matrix $\boldsymbol{s}_- = \boldsymbol{S}\boldsymbol{s}_+$ as:

$$\boldsymbol{S} = \boldsymbol{C} - i\boldsymbol{D}\frac{1}{(\boldsymbol{\Omega} - i\boldsymbol{\Gamma}) - \omega}\boldsymbol{D}^T \tag{A.20}$$

For systems with no absorption loss, all decay comes from radiative coupling to propagating channels. When energy conservation and time-reversal symmetry hold, it can be shown that [172]:

$$\boldsymbol{\Gamma} = \frac{\boldsymbol{D}^\dagger \boldsymbol{D}}{2} \tag{A.21}$$

$$\boldsymbol{C}\boldsymbol{D}^* = -\boldsymbol{D} \tag{A.22}$$

$$\boldsymbol{C}^\dagger \boldsymbol{C} = I \tag{A.23}$$

In what follows, we neglect loss so that these relationships hold.

All that remains is evaluation of the (system-dependent) coupling constants in $\boldsymbol{C}$, $\boldsymbol{D}$, and $\boldsymbol{\Omega}$. For two coupled optical resonators, the modes are enumerated as follows. All modes are labeled by their tranverse spatial mode index t. Channel modes have an additional port index yielding $s_{\pm,pt}$. Resonator modes have a cavity index and an axial mode index z yielding a_{ctz}.

To define the direct coupling matrix $\boldsymbol{C}$ we note that any incoming power not coupled into the resonator is reflected into the same channel, so $\boldsymbol{C}$ is diagonal. Combined with Equation A.23, this means each element of $\boldsymbol{C}$ is a phase factor with unit magnitude. We take coupling to occur at the mirror surface, so that all transverse modes must experience the same reflection phase shift. This defines $\boldsymbol{C}$ up to a single arbitrary phase, which we choose so that $\boldsymbol{C} = -I$.

The resonator-to-channel matrix $\boldsymbol{D}$ only couples modes with the same spatial mode index t. Resonator modes in a given cavity only couple to mirror(s) connected to that

cavity. Therefore the element $D_{pt',ctz} = \xi_{ptz}\delta_{t,t'}\sigma_{p,c}$, where we define $\sigma_{p,c} = 1$ if port p is connected to cavity c and zero otherwise, and ξ_{ptz} is a complex constant. The magnitude of ξ_{ptz} is fixed by an energy conservation argument [175]. We note that the energy of a single populated mode a_{ctz} with no input decays as $|a_{ctz}(t)|^2 = |a_{ctz}(0)|^2 e^{-\sum_p \gamma_p t}$, where the sum is over ports accessible from cavity c, $\gamma_p = -\nu_c \ln R_p$ is the decay rate into port p, ν_c is the free spectral range of cavity c, and R_p is the reflectance of the mirror at port p. The power exiting is $\frac{d}{dt}|a_{ctz}(t)|^2 = -\left(\sum_p \gamma_p\right)|a_{ctz}(t)|^2$. Therefore we ascribe a decay coefficient γ_p to each port p coupled to a_{ctz}. However, according to Equation A.19 the power exiting into port p is $\left|s_{-pt}\right|^2 = \left|D_{pt,ctz}\right|^2 |a_{ctz}(t)|^2$. Thus $\left|D_{pt,ctz}\right|^2 = \gamma_p$ and $\left|\xi_{ptz}\right| = \sqrt{\gamma_p}$.

The phase of ξ_{ptz} is constrained by Equation A.22 and our choice of $\boldsymbol{C} = -I$, yielding $\boldsymbol{D}^* = \boldsymbol{D}$, so all elements of $\boldsymbol{D}$ are real and defined up to a sign. Each resonant mode can have one arbitary sign in the coupling constant at one port. For all other ports accessible to that mode, the sign must be chosen consistently. This is important when multiple axial modes are included; adjacent axial modes have opposite parity, and incorrectly chosen signs will affect the interference between modes.

Finally we evaluate the closed-cavity Hamiltonian matrix $\boldsymbol{\Omega}$. The diagonal elements are just the (real) mode frequencies set by the free spectral range and transverse mode spacings. The off-diagonal elements represent coupling rates between resonant modes. We evaluate these with a similar energy conservation argument as used for $\boldsymbol{D}$ [175]. Coupling occurs between the modes of two cavities separated by a mirror of reflectance R_c. The circulating power in mode $a_{c't'z'}$ of cavity c' excites a mode a_{ctz} of cavity c. According to Equation A.18, the coupling contributes to $\frac{d}{dt}a_{ctz}$ a term $\Omega_{ctz,c't'z'}a_{c't'z'}$. This can be compared to excitation of a mode by a propagating channel, which contributes to $\frac{d}{dt}a_{ctz}$ a term $D_{pt,ctz}s_{+pt}$, where the incident power is $P = \left|s_{+pt}\right|^2$ and we have already determined the magnitude $\left|D_{pt,ctz}\right| = \sqrt{-\nu_c \ln R}$. In the present case the incident power due to mode $a_{c't'z'}$ is $P = |a_{c't'z'}|^2 \nu_{c'} \left|\alpha_{t',t}\right|^2$, where the overlap integral $\alpha_{t',t}$ restricts to that portion of

the incident mode which is spatially mode-matched. Comparing these two cases, we must have $\left|\Omega_{ctz,c't'z'}\right| = \sqrt{-\nu_c \nu_{c'} \ln R_c}\left|\alpha_{t',t}\right|$. The phase of the coupling coefficients must be chosen with similar concern as the elements of $\boldsymbol{D}$, taking into account the opposite parity of adjacent axial modes.

Although there exists an exact coupled-mode description of single-mode resonators [176] which could be extended to the multimode case, we do not pursue that here, as the S-matrix description of Supplement A.3 provides exact results, and the simpler coupled-mode theory is quite accurate and useful for intuition.